การประเมินค่าปริมาณรังสีที่ผิวจากการฉายรังสีโฟตอนพลังงาน 6 เมกะโวลต์

นางสาวลัคนา อภิปัญญาโสภณ

วิทยานิพนธ์นี้เป็นส่วนหนึ่งของการศึกษาตามหลักสูตรปริญญาวิศวกรรมศาสตรดุษฎีบัณฑิต
สาขาวิชาวิศวกรรมนิวเคลียร์ ภาควิชาวิศวกรรมนิวเคลียร์
คณะวิศวกรรมศาสตร์ จุฬาลงกรณ์มหาวิทยาลัย
ปีการศึกษา 2555
ลิขสิทธิ์ของจุฬาลงกรณ์มหาวิทยาลัย

ESTIMATION OF SURFACE DOSE FROM THERAPEUTIC 6 MV
PHOTON BEAMS

Miss Lukkana Apipunyasopon

A Dissertation Submitted in Partial Fulfillment of the Requirements
for the Degree of Doctor of Engineering Program in Nuclear Engineering
Department of Nuclear Engineering
Faculty of Engineering
Chulalongkorn University
Academic year 2012

Thesis Title   ESTIMATION OF SURFACE DOSE FROM
THERAPEUTIC 6 MV PHOTON BEAMS

By   Miss Lukkana Apipunyasopon

Field of Study   Nuclear Engineering

Thesis Advisor   Assistant Professor Nakorn Phisangittisakul, Ph.D.

Thesis Co-Advisor   Associate Professor Somyot Srisatit, M.Eng.

Accepted by the Faculty of Engineering, Chulalongkorn University in Partial Fulfillment of the Requirements for the Doctoral Degree

………………………………… Dean of the Faculty of Engineering

(Associate Professor Boonsom Lerdhirunwong, Dr.Ing.)

THESIS COMMITTEE

………………………………………….. Chairman

(Associate Professor Supitcha Chanyotha, Ph.D.)

………………………………….……. Thesis Advisor

(Assistant Professor Nakorn Phaisangittisakul, Ph.D.)

………………………………………….. Thesis Co-advisor

(Associate Professor Somyot Srisatit, M.Eng.)

………………………………………….. Examiner

(Associate Professor Sunchai Nilsuwankosit, Ph.D.)

………………………………………….. Examiner

(Phongphaeth Pengvanich, Ph.D.)

………………………………………….. External Examiner

(Associate Professor Lalida Tuntipumiamorn, M.Sc.)

ลัคนา อภิปัญญาโสภณ : การประเมินค่าปริมาณรังสีที่ผิวจากการฉายรังสีโฟตอนพลังงาน 6 เมกะโวลต์. (ESTIMATION OF SURFACE DOSE FROM THERAPEUTIC 6 MV PHOTON BEAMS) อ.ที่ปรึกษาวิทยานิพนธ์หลัก : ผศ.ดร.นคร ไพศาลกิตติสกุล, อ.ที่ปรึกษาวิทยานิพนธ์ร่วม : รศ. สมยศ ศรีสถิตย์, 123 หน้า.

เนื่องจากในปัจจุบันมีการนำรังสีมาใช้ประโยชน์ในการรักษาด้านการแพทย์เพิ่มขึ้น การทราบค่าปริมาณรังสีที่ผิวได้รับอย่างถูกต้องจึงมีส่วนช่วยในการกำหนดเทคนิคการรักษา และค่าปริมาณรังสีโดยรวมที่จะให้กับผู้ป่วย รวมถึงบอกผลกระทบที่อาจเกิดกับผิวจากการรับรังสีได้ โดยทั่วไปการประเมินค่าปริมาณรังสีที่ผิวทำโดยการวัดด้วยหัววัดรังสีชนิดต่างๆ อย่างไรก็ตามจากการปนเปื้อนของอิเลคตรอนที่บริเวณความลึกใกล้ผิว ทำให้ค่านับวัดที่ได้จากหัววัดรังสีมากเกินความจริง ในการศึกษาครั้งนี้จึงได้ทำการหาค่าปริมาณรังสีที่ผิวจากเครื่องเร่งอนุภาคที่พลังงานรังสีโฟตอน 6 เมกะโวลต์ ในขนาดพื้นที่ลำรังสีตั้งแต่ 3 จนถึง 25 เซนติเมตร ตามแนวกึ่งกลางลำรังสีด้วยวิธีการจำลองด้วยโปรแกรม EGS4nrc Monte Carlo เทคนิค และการวัดด้วยหัววัดรังสีชนิดต่างๆ ได้แก่ หัววัดรังสีชนิดบรรจุก๊าซ (CC13 dosimeter and Markus chamber), หัววัดรังสีชนิดสารกึ่งตัวนำ (PFD^{3G} dosimeter) และหัววัดรังสีชนิดสารเรืองแสง (TLD chip) หาค่าปริมาณรังสีที่ผิวด้วยการลากเส้นแนวโน้มของชุดข้อมูลที่ได้จากทั้งการคำนวณ และการวัดที่ความลึกใกล้ผิว จากการศึกษาพบว่าค่าปริมาณรังสีที่ผิวทั้งจากการคำนวณ และการวัดพบว่ามีค่าเพิ่มขึ้นอย่างมีนัยยะสำคัญเมื่อเพิ่มขนาดพื้นที่ของลำรังสีตกกระทบ โดยค่าปริมาณรังสีที่ผิวจากการวัดจะมีค่ามากกว่าจากการคำนวณ เพื่อให้การประเมินค่าปริมาณรังสีที่ผิวจากการวัดในช่วงขนาดพื้นที่ลำรังสี 5 ถึง 20 เซนติเมตรมีความถูกต้อง จึงได้ทำการกำหนดค่าแก้เนื่องจากปริมาณรังสีที่วัดได้มากเกินจริงสำหรับหัววัดรังสีแต่ละชนิด โดยหัววัดรังสีที่ให้ค่านับวัดมากเกินจริงน้อยที่สุด และมากที่สุดในการศึกษานี้คือ TLD chip และ CC13 dosimeter ตามลำดับ สำหรับในขนาดพื้นที่ลำรังสีใดๆ สามารถคำนวณหาค่าปริมาณรังสีที่ผิวได้โดยการหาพื้นที่เทียบเท่าพื้นที่จัตุรัสด้วยสูตรพื้นที่ต่อเส้นรอบวง เมื่อทำการเปรียบเทียบค่าปริมาณรังสีที่ผิวจากการคำนวณในพื้นที่นั้นๆ รวมถึงการสลับแกน กับการหาพื้นที่เทียบเท่าพื้นที่จัตุรัสพบว่าค่าความแตกต่างอยู่ในระดับที่ยอมรับได้ ดังนั้นค่าปริมาณรังสีที่ผิวในพื้นที่ลำรังสีใดๆ สามารถประเมินได้อย่างน่าเชื่อถือด้วยวิธีการที่ใช้ในการศึกษานี้

ภาควิชา   วิศวกรรมนิวเคลียร์   ลายมือชื่อนิสิต _____

สาขาวิชา   วิศวกรรมนิวเคลียร์   ลายมือชื่อ อ.ที่ปรึกษาวิทยานิพนธ์หลัก _____

ปีการศึกษา   2555   ลายมือชื่อ อ.ที่ปรึกษาวิทยานิพนธ์ร่วม _____

LUKKANA APIPUNYASOPON: ESTIMATION OF SURFACE DOSE FROM THERAPEUTIC 6 MV PHOTON BEAMS. ADVISOR: ASSIST. PROF.NAKORN PHAISANGITTISAKUL, Ph.D., CO-ADVISOR: ASSOC. PROF. SOMYOT SRISATIT, M.Eng., 123 pp.

Accurate assessment of surface dose from therapeutic photon beam can lead to predict the skin reaction and design the radiation treatment technique. Many common dosimeters have been used to estimate the surface dose. However, they are known to over-response in the near surface region. In this study, the surface dose at the central axis of 6 MV photon beams from Varian Clinac 23EX medical linear accelerator was investigated using both measurement and simulation. The photon beams are in square and rectangular shape with the side ranging from 3 to 25 cm defined by the collimators. The measurements were taken using four detectors: TLD chip, PFD^{3G} diode, Markus parallel-plate and CC13 cylindrical ionization chamber. The EGS4nrc Monte Carlo (MC) code was used in the simulation. The surface dose was obtained from an extrapolation of absorbed dose in the near surface region. It was found to be significantly increased almost linearly with the increasing square field size from both measured and simulated results. As expected, the surface dose from the measurement was higher than the simulated result. The lowest and highest over-responses in the surface dose measurement, compared with MC simulation, were found with the TLD chip and the CC13 chamber, respectively. Using the MC result as a gold standard, the correction factors for each dosimeter for estimating the surface dose from square photon beam with the side between 5 to 20 cm were introduced. For the rectangular field, its surface dose can also be obtained from that of the square field using the equivalent square approach. Specifically, the side of the equivalent square of rectangular field was computed using the area-to-perimeter formula. In the comparison between the percentage surface dose of rectangular field and that of the relevant equivalent square, the difference was found to be clinically negligible. Moreover, the influence of collimator scatter on the surface dose was also found to be insignificant. Hence, the surface dose of various rectangular fields from therapeutic photon beam can be predicted reliably using the approach proposed in this study.

Department : Nuclear Engineering   Student's Signature _____

Field of Study : Nuclear Engineering   Advisor's Signature _____

Academic Year : 2012 _____   Co-advisor's Signature _____

ACKNOWLEDGEMENTS

CONTENTS

Page

Page

Page

LIST OF TABLES

Table   **Page**

Table   **Page**

LIST OF FIGURES

LIST OF ABBREVIATIONS

Abbreviation	Terms
A	Specific parameter
AAPM	American Association of Physicists in Medicine
AE	Electron production cutoff energy
AP	Photon production cutoff energy
A/P	Area to Perimeter
BCA	Boundary Crossing Algorithm
C	The collector edge to side wall distance in mm
CC13	Compact chamber with sensitive volume of 0.13 cm^3
C_i	The correction factor for each detector
C_{ij}	The calibration factor for each individual TLD chip
CM	Component Module
cm^2	Square centimeter
cm^3	Cubic centimeter
^{60}Co	Cobalt-60
CPE	Charged Particle Equilibrium
CPU	Central Processing Unit
CT	Computed Tomography
°C	Degree Celsius
d$_{max}$	The depth of maximum dose
D	Absorbed dose
D_0	The percentage surface dose
DC/DC	Direct current to direct current
E	The maximum energy of the photon spectrum
ECUT	Global Electron Cutoff Energy
EGS	Electron Gamma Shower
ESA	Electron Step Algorithm
ETRAN	Electron Transport
GeV	Gigaelectronvolt

Abbreviation	Terms
GK	Gerki and Khan
GHz	Gigahertz
Gy	Gray
g	Radiative fraction
g/cm^3	Gram per cubic centimeter
h	hour
IAEA	International Atomic Energy Agency
ICRP	International Commission on Radiological Protection
ICRU	International Commission on Radiation Units and Measurements
IR	The ionization ratio measured at 10 and 20 cm depths for the field size of 10×10 cm^2 at 100 cm SSD
k	Geometric parameter
K	kerma
K_{col}	Collision kerma
K_{rad}	Radiative kerma
keV	Kiloelectronvolt
l	The plate separation
L	The length of square field's side
L_{eq}	The side of equivalent square for rectangular field
L_{sq}	The side of equivalent square field
L_x	The field's side defined by the X-collimator
L_y	The field's side defined by the Y-collimator
LiF	Lithium Floride
MC	Monte Carlo
MCNP	Monte Carlo Neutron Photon
MeV	Megaelectronvolt
Mg	Megnesium
MLC	Multileaf collimator
mm	Millimeter

Abbreviation	**Terms**
mm/s	Millimeter per second
mm^2	Square millimeter
MU	Monitor Unit
ms	Millisecond
MV	Megavoltage
NRC	National Research Council of Canada
PCUT	Global Photon Cutoff Energy
PDD	Percentage Depth Dose
PDI	Percentage Depth Ionization
PENELOPE	PENetration and Energy Loss of Positrons and Electrons
PFD^{3G}	p-type photon semiconductor dosimeter
PMT	Photomultiplier Tube
PRESTA	Parameter Reduced Electron Step Transport Algorithm
P′(d)	The corrected percentage depth dose at depth 'd'
P(d)	The uncorrected percentage depth dose at depth 'd'
R$_{ij}$	The reading of the ij TLD chip
SMAX	Maximum Step Size
SSD	Source-to-surface distance
TCPE	Transient Charged Particle Equilibrium
TG	Task Group
Ti	Titanium
TL	Thermoluminescent
TLDs	Thermoluminescence dosimeters
TPSs	Computerized Treatment Planning System
TRS	Technical Report Series
V	Electrical potential difference in voltage
ξ (E,0)	The over-response in percent per mm of chamber plate separation
α	An empirically determined constant of proportionality

CHAPTER I

INTRODUCTION

1.1 <u>Background and rationale</u>

From the past to present, both directly (charged particles such as electron and positron) and indirectly (neutral particles such as photon and neutron) ionizing radiations are mainly used in the treatment of cancer diseases. Most type of treatment in radiotherapy is the use of a high energy photon beam generated by a medical linear accelerator. The interaction of photon beams may be occurred with a tightly bound electron (Photoelectric absorption), with an essentially free orbital electron (Compton scattering) or with the field of the nucleus (Pair production). As the beam passes through the patient, it interacts with tissues forming highly reactive radicals in the intracellular material, and denatured cellular components that can cause lethal damage to the irradiated cells. With an increase of the beam energy, the penetrating power of photon as well as the secondary charged particle increases and allows to be treated in a deeper position. The maximum energy of the produced photon depends on the energy of impinging electrons. Normally, the range of therapeutic photon beam energies is 6-25 MV. The depth of maximum dose increases with the beam energy. The deposited energy in the tissue from the irradiation per unit mass of tissue is known as the radiation absorbed dose. The higher the absorbed dose is the greater the chance of killing cells [1].

The absorbed doses increase with the depth in the medium, when the medium is irradiated with the photon beam. A maximum dose is reached at a depth of maximum range of electrons produced by the photons [2]. The dose deposited within the first few millimeters of skin depth varies considerably which is known as the build-up region [1]. It is a special characteristic of the photon beams. The surface dose is known as the dose accumulated at the boundary between air and patient's skin. Normally, the surface dose is about 75-95% of the maximum dose for an electron beam and about 10-30% for a photon beam [1]. For high energy photon beam used in

conventional radiotherapy, the surface dose may not be a major concern because of the skin-sparing effect [3-7]. However, for the unconventional hypofractionated radiation where the fractional dose is extremely high and for the treatment of deep-seated tumors, the skin complications may be the limiting factor in the delivery of high tumor dose. Therefore the doses at the surface and in the buildup region are an important factor for prescription the radiation dose.

A clinical photon beam mainly consists of primary photons, scattered photons and contaminant electrons [8]. Primary photons come directly from the target to the patient. Scattered photons are generated or scattered in the accelerator components other than target. Contaminating electrons are produced by the photon interaction in the air between the source and the patient, in the phantom and in the scattering material in the path of the beam. Because the electron contamination is mainly affect the superficial part of the depth dose, the therapeutic photon dose distribution at the surface and the buildup region is consisted of the pure photon dose and the contaminating electron dose [8]. Several studies have been investigated the sources of contaminating electron for clinical photon beams.

In 1983, Petti et al [9] investigated the contaminated electron sources in the accelerator's head for the 25 MV photon beam at the source to surface distance (SSD) of 80-100 cm using the EGS3 Monte Carlo code. They summarized that the electron contamination mainly derived from the flattening filter and monitor chamber, and the collimating system. In 1986, Nilsson and Brahme [10] showed that the air volume between the target to patient at the extended SSD also a major contributor to the surface dose. In 2000, Butson et al [11] also investigated the electron contribution from air volume at the 6 MV photon beam produced by linear accelerator. The study was done by the calculation using the Monte Carlo Neutron Photon 4A (MCNP 4A) and by the measurement using an Attix parallel plate ionization chamber. The results showed that the number of electrons excited in the air volume increase with the increasing field size from 10% to 18% for the field sizes of 10×10 to 40×40 cm^2, respectively.

All studies showed that the secondary electrons generated from the treatment head and from the air volume contributed the most of surface dose. According to the comprehensive published data, the major source of the contaminant electrons at the

surface for the photon energy higher than 8 MV has been the flattening filter. For the photon energy lower than 8 MV, the contaminant electron generated by the movable jaws may become important. The previous publications presented that the dose at the surface and the buildup region of clinical photon beams have been studied for the photon beam energies between the 1.25 MV and 25 MV [9-17]. The surface dose for a 10×10 cm^2 field amounts to some 30% of the maximum dose for a cobalt beam, 15% for a 6 MV X-ray beam and 10% for a 18 MV X-ray beam [1]. Therefore, the surface dose depends on the specific parameters, such as the beam energy, the field size, the angle of beam incidence, the air gap and the beam-modifying devices [18-20].

Because the stem cells in the basal layer of skin are sensitive to radiation, they become less able to divide, repopulate and repair the skin's cells within treatment field when received the repeatedly radiation [21]. For radiotherapeutic irradiation, the skin reactions are a common site effect. The radiation exposure of the skin may affect the basal cells and leads to several phases of skin response [22,23]. Because the different reactions originate from different depths of the skin, the determination of skin dose will be complicated. The epidermal and dermal layers of the skin are defined from the surface to a depth of 1-4 mm. High dose in dermis contained the capillaries may lead to erythema, fibrosis, epilation, glandular injury, further vascular damage, and eventually to necrosis. Early skin reactions are evident approximately 1-4 weeks after beginning treatment and can persist of several weeks post treatment. It progresses from erythema to desquamation and to necrosis. The first phase of response is an erythema that seen within a few hours of irradiation. Either a dry or moist desquamation is the result of cell death in the basal layer and may be seen after 3-6 weeks. Late skin reactions are defined as the appearance of skin damage such as telangiectasia, dermal atrophy and necrosis that are occurred six moths after completion of radiation treatment.

According to the reports by the ICRU and ICRP, the practical dose determination of the skin layer is at 70 µm depth, which corresponds to the depth of basal layer [21]. The basal cell layer is the interface between the epidermis and dermis layers of the skin and is interested for skin erythema, and also the critical layer for carcinogenesis. Since the thickness of epidermis varies throughout the human body, the clinically relevant depth for skin dose determination should be considered. The

composition and thickness of the skin vary with location from 0.002-0.006 cm on the trunk and face, and from 0.05 for the eyelid to 1.5 mm for sole of the foot. Therefore the severity of the skin complication depends on the patient response and the treatment factors such as the radiation dose and the exposed condition.

The choice of the dosimeter is of great important for measurement in this region, because the conditions required for the equilibrium of the charged particles are not met in the build-up region, and the dose gradient is also high. The role of electronic equilibrium in the measurement will be occurred when the cavity volume is sufficiently large enough to collect all of particles. If the equilibrium exists, each electron carried an energy out of volume is compensated by another electron carried the same energy in. Thus the average charge in the volume equals the total charge released in volume [24]. Because the effective point of measurement of most commonly dosimeters are ranging from several micrometers to a few millimeters and there is no dosimeter that has an infinitely small sensitive volume, the surface dose by definition is difficult to measure.

The use of an extrapolation chamber is suggested for a more reliable measurement of the dose in the buildup region [25, 26-29]. Its measurement of surface dose was done by varying the electrode separations and extrapolated the reading to zero plate separation [28]. While the extrapolation chamber works well in this region, its measuring procedure is time-consuming and, therefore, impractical in a clinical setting. Additionally the most computerized treatment planning system (TPSs) fail to accurately determine the surface dose of the patient because of the accurately skin delineating on the CT slices and the larger voxel size in TPS [30]. Therefore it is interesting to introduce the better and practical method to estimate the dose at surface and at relevant depths. The detailed information of the dose at surface and various depths of the skin in critical to taken into account with the treatment criteria, and becomes one of important factors in radiation treatment planning. Knowing the accurate surface dose is, therefore, essential for assessing the skin complication, guiding the bolus thickness decision, and designing both the treatment technique and the scheme of dose fractionation.

1.2 <u>Research objectives</u>

1.2.1 To investigate the surface dose at the central axis of 6 MV therapeutic photon beam of square and rectangular fields with various sizes using the Monte Carlo simulation along with the measurement.

1.2.2 To introduce the method for estimating the surface dose for different rectangular field sizes.

1.3 <u>Scope of dissertation</u>

1.3.1 Therapeutic photon beam is obtained from the Varian Clinac 23EX linear accelerator installed at Siriraj hospital.

1.3.2 The simulation was done using the EGSnrc Monte Carlo code.

1.3.3 The dose measurements were done using four common detectors: a compact cylindrical ionization chamber type CC13, a silicon p-type photon semiconductor dosimeter type PFG^{3G}, a parallel-plate ionization chamber type Markus 23392 and TLD chips.

1.3.4 The measurements of surface dose are done in either water tank or solid water phantom.

1.3.5 The surface dose is investigated for:

  1.3.5.1 The square open field sizes of 3×3, 5×5, 10×10, 12×12, 15×15, 20×20 and 25×25 cm^2.

  1.3.5.2 The rectangular open field size ranges from 20×5 to 20×20 cm^2 and from 5×20 to 20×20 cm^2.

CHAPTER II

LITERATURE REVIEWS

2.1 <u>Kerma and Absorbed dose</u>

Kerma (K) is a kinetic energy released per unit mass, and quantifies the mean energy transferred from the indirectly ionizing radiation to charged particles in the medium without a concern to what happens after this transfer. It consists of two components: the collision kerma (K_{col}) and the radiative kerma (K_{rad}). Because the electrons traveled in the medium and deposited energy along the tracks, the energy absorption does not take place at the same location as the energy transfer described by kerma. This is due to the non-zero (finite) range of the secondary electrons released through photon interactions [1].

Absorbed dose (D) is defined as the mean energy imparted by ionizing radiation in the medium per unit mass [1,31]. It is a non-stochastic quantity applicable to both indirectly and directly ionizing radiations. The gray (Gy) is a radiation unit of absorbed dose, and is defined as joule/kilogram, the absorbed energy per unit mass of the medium.

For indirectly ionizing radiations, the energy of photon is imparted to matter in two processes. In the first step, the indirectly ionizing radiation transfers energy as kinetic energy to secondary charged particles through various interactions. In the second step, these charged particles transfer some of their energy to the medium through in the form of radiative losses. Because of the escape of the radiative photons from the volume of interest, one relates absorbed dose usually to collision kerma. If a high energy photon beam penetrates the medium, kerma is maximal at the surface of the irradiated material because the photon fluence is greatest at the surface, but the charged particle fluence will be increased as a function of depth until the depth of dose maximum is attained. While, the absorbed dose near the surface is less and combined with both the incident contaminating electrons and photon-generated

electrons. Loevinger introduced the ratio between absorbed dose (*D*) and collision kerma (*K*$_{col}$) in order to describe the buildup dose. It is often denoted as

$$\beta = \frac{D}{K_{col}} \qquad (1)$$

Figure 2.1 represent the relation between collision kerma and absorbed dose under buildup condition. If there were no photon attenuation or scattering in the medium, but yet production of electrons would occur, the buildup region will be followed by a region of complete charged particle equilibrium (CPE), as presented in Figure 2.1 (a). Because of the photon attenuation and scattering in the medium in the more realistic situation, a region of transient charged particle equilibrium (TCPE) occurs, as presented in Figure 2.1 (b). At the condition of transient electronic equilibrium, the ratio between *D* and *K* reached a limiting value, depended on the energy and slightly on field size. Nilsson and Brahme [13] calculated the typical value of the ratio between *D* and *K* is 1.02 for both 6 and 21 MV beam. This relation is practically constant, since the average energy of the generated electrons in high energy photon beams and their ranges do not change appreciably with in the medium.
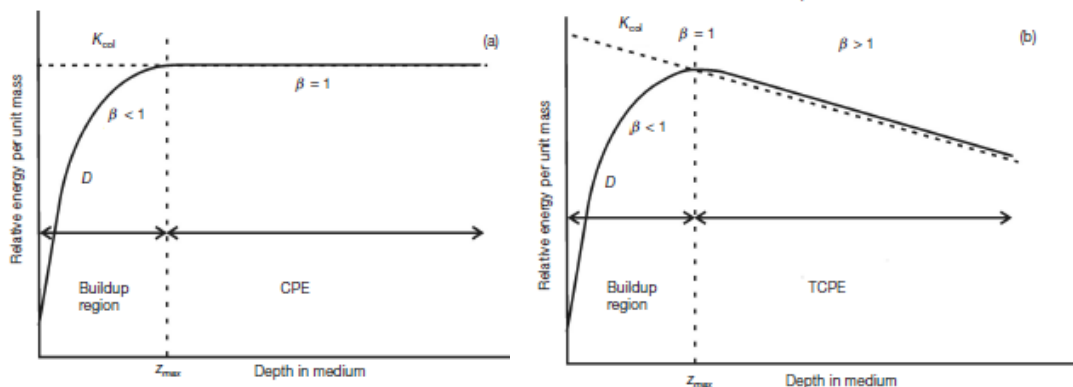
Figure 2.1. Kerma and absorbed dose as a function of depth in a medium irradiated by a high energy photon beam for (a) no photon attenuation or scattering and for (b) the realistic case [1].

If radiative photons escape the volume of interest, an assumption is made that $\beta \approx 1$. If the surface dose is due entirely to the contaminating electron, an assumption is made that $\beta = 0$. In the special case in which true CPE exists at the depth of maximum dose in the medium, the relation between absorbed dose and total kerma is given by:

$$D = K_{col} = K\left(1 - \bar{g}\right)$$
(2)

where $\bar{g}$ is the radiative fraction, depending on the electron kinetic energy, and the atomic number of material.

Bjarngard et al [32] described an experimental method to determine the dose near the surface under lateral equilibrium conditions using a mathematical extrapolation based on the MC simulation-calculated kerma values. The equilibrium dose at large depths is extrapolated back towards the surface and compared with measured dose at the 6 and 25 MV photon beam. The results showed that the electron dose generated from phantom increased exponentially with depth from zero at the surface and the contaminating electron doses decreased rapidly with depth with an attenuation coefficient.

2.2   <u>Measurement</u>

Generally, the detection of gamma rays for the megavoltage photon beam is carried out by a dosimeter, defined as any device that provides a reading from the measurement in the form of the average absorbed dose deposited in its sensitive volume. Because the perturbation effect from the contaminated electrons in the beam and the secondary electrons generated in the irradiated medium are occurred and the equilibrium condition of the charged particles are not met in the build-up region, the accurate measurement in this region is difficult [26]. To measure the dose in this region, the size of dosimeter should be as small as possible. In the past, the surface

dose from therapeutic photon beams was investigated using various types of dosimeter as described in the following subsections [1-7, 25].

2.2.1   Ionization chamber dosimeters

The fundamental of ionization chamber is an air-filled dosimeter that particularly well-suited for measurement the photon beam energies below 10 MeV [1]. Because of the long range of the secondary electrons from high photon energies, the measurement is done using a cavity chamber. It is defined as a small gas-filled volume, surrounded by a solid wall material. If the chamber walls of detector are sufficiently thick compared with the range of secondary electrons, a condition of electronic equilibrium is established [24].

However, there is a problem for keeping the cavity small enough when compared with the range of incident charged particles in the build-up region, and that can be explained by the Bragg-Gray cavity principle. It is the first cavity theory developed to provide a relation between the absorbed dose in a dosimeter and in the medium containing the cavity [1]. In 1929 and 1939, Gray refined the principle and relies for its validity on four basic assumptions [31]:

- Charged particle equilibrium exists in the absence of the cavity
- The particle fluence is not disturbed by the cavity presence
- The mass stopping power ratio constants over the energy spectrum
- The secondary particles lose their energy by a large number of small interactions.

In therapeutic photon beam, Gas-filled ionization chamber can be also applied indirectly to measure the absorbed dose in arbitrary media. It comes with various shapes and sizes and can be used as a reference dosimeter. Basically, it is surrounded by a conductive outer wall and having a central collecting electrode. The wall and the collecting electrode are separated by a high quality insulator to reduce the leakage current when a polarizing voltage is applied to the chamber. A guard electrode is usually provided in the chamber to further reduce chamber leakage, and allows it to flow to guard by passing the collecting electrode. Most common types of ionization

chamber, used in the radiative measurement are cylindrical and parallel-plate ionization chambers. A cylindrical ionization chamber is used to the rigors of radiotherapy output measurement, while a parallel-plate ionization chamber is used for measurement the output of low electron energy and the surface dose [31].

2.2.1.1 Extrapolation chamber

An extrapolation chamber is one category of parallel plate ionization chamber with a small sensitive volume which can be varied as a function of electrode spacing [25]. It has a large guard width when compared with the electrode separation and the sidewalls distance. The example of an extrapolation chamber is shown in Figure 2.2.
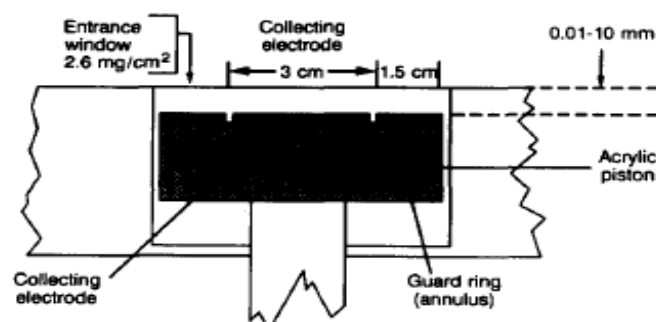
Figure 2.2.   Diagram of the PTW extrapolation chamber demonstrated chamber dimensions and entrance window thickness [27].

In the several literature reviews [25, 26-28], they had suggested for more reliable measurement of the dose in the build-up region and in the transition zones between two different media, in which the electronic equilibrium of charged particles does not exist. Because an extrapolation chamber has a large guard width when compared with the chamber height, the electrons contribution from side wall is reduced, as reported by Nilsson and Montelius [28]. The surface dose can be estimated by measuring the ionization per unit volume as a function of electrode

spacing, and then extrapolating the data to the zero electrode spacing. Unfortunately, the use of the extrapolation chamber is limited and a time consuming procedure since it is not typically available in most institutes and in routine situation.

2.2.1.2 Parallel plate ionization chamber

A parallel plate ion chamber is a fixed-electrode volume and consists of two plane walls, one serving as an entry window and polarizing electrode, and the other as the back wall and collecting electrode, as illustrated in Figure 2.3. The back wall is usually a block with a thin conducting layer of graphite forming the collecting electrode and the guard ring system on top [1]. A layer of gas between the walls acts as the collecting volume. It can be constructed very thinly, leading to less perturbation. It is commonly available and also convenient to use for the surface dose measurement in various situations [33-41].
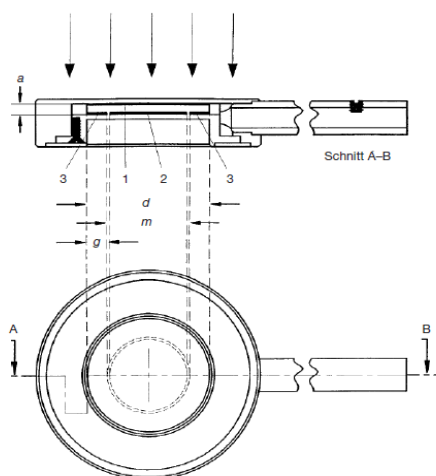
Figure 2.3. Diagram of the parallel plate ionization chamber [1].

However, its accuracy in the build-up region remains in doubt since there exist a cavity perturbation from the chamber volume. Because of the non-electronic equilibrium condition in the buildup measurements, the perturbation of the electron fluence contributed to the ionization in the chamber. When the photon beam interacted on the chamber, many electrons in the front electrode, collector and through the side walls are emitted and then backscattered into the active chamber volume.

However, the main contribution in the chamber volume is due to secondary electrons coming from the air and the treatment head. Nilsson and Montelius [26] investigated the perturbation effect of these electrons due to the emitted electrons through the side walls in parallel plate ionization chamber used for buildup measurement. The studies were done by measurement using film and extrapolation chambers in a $30\times30\times30$ cm^3 polystyrene phantom and by calculations in the ^{60}Co machine and the Scanditronix M22 Microtron with the 6 and 21 MV photon beam energies. The plate separation of an extrapolation chamber was varied between 0.5 and 1.0 mm. The results showed that the perturbation electron fluence depends on the side wall material and chamber geometry. The linear relationship between the plate separation and the contribution to the mass ionization for all photon beam energies was observed at the plate separation larger than 2 mm. When the plate separation increased, they will give a large contribution in the collecting volume. For a smaller diameter chamber, a larger contribution from side wall electrons and a larger slope in the extrapolation curve were observed. The backscattered electron fluence throughout the chamber volume investigated by film was about 8% of the dose at the maximum depth for a 1.2 mm cavity height both for the 1.25 MV and 21 MV photon beam.

Velkley et al [36] evaluated the errors in measurements with a parallel plate chamber in the buildup region and proposed a formula for collecting results to the zero volume condition. The measurements of surface and buildup dose has been done by an aluminum-walled extrapolation chamber, a cylindrical and parallel plate ionization chamber with the 1.2-25 MV photon beam energy. The plate separation of an extrapolation chamber was varied from 0 to 8 mm. According to this study, the overestimation of the percentage depth dose obtained from the parallel plate chamber is about 10% - 40% when compared with the extrapolation chamber. To obtain an accurate surface dose value, the ionization reading has been corrected by taken into account the perturbation conditions [27-29]. Based on the data taken with an extrapolation chamber, the correction factor for percentage depth dose, expressed as a percentage change per millimeter of plate separation was applied to the buildup dose measured by a fixed-separation parallel plate chamber to correct the results. Because the perturbation effect varied with side wall material and chamber geometry depended on the electron contamination of the beam and angular distribution of the electron

fluence, the Velkley formula obtained with only one extrapolation chamber for a specific parallel plate chamber either under or over compensated the surface dose measurements for a different type of chamber.

Gerbi and Khan [28] evaluated the magnitude of the over-response dose at the surface and in the buildup region obtained with the commercial parallel plate chamber and TLD dosimeter, and modified the correction factor introduced by Velkley et al [29]. All measurements were performed at the square field size of 5, 10, 15 and 25 cm for the ^{60}Co treatment machine, the 6 MV and 24 MV photon beams generated by a Varian Clinac, and the 10 MV and 24 MV generated by a Philips linear accelerator. The response of four parallel plate ion chambers was studied: two Memorial Pipe chambers, the Markus chamber, and the Capintec PS-033 thin-window ionization chamber, and compared with an extrapolation chamber (PTW, Frieburg, Model 30-360) and TLD dosimeter. The extrapolation chamber was measured at the electrode separations of 0.5, 1.0, 2.5, and 5.0 mm. TLD chip with the thickness of 0.38 mm^3 and TLD powder were also used to measure the surface dose at any field sizes. The relative surface doses were normalized to the depth of dose maximum for various beam energies. This suggested that all parallel plate ion chamber over responded at the surface region. When compared with the extrapolation chamber, the magnitude of the over-prediction depends on the internal dimensions of the chamber and the beam energy. For the 6 MV photon beam, the over-responded of the percentage surface dose obtained from Markus chamber and TLD chip was more than 10% and about 12%, respectively. The percentage surface dose derived from the TLD powder was within 3% of the dose measured with the extrapolation chamber. The magnitude of the over response was more severed at a lower beam energy, as consistented with the results of Velkley et al [29]. For the high energy photon beam, the in-scattering electrons from the side walls of the chamber were less to reach the active volume because the scattered electron was more forward direction. After applied the Velkley correction, the difference in the percentage surface dose at the 6 MV photon beam obtained from the Capintec chamber and two Memorial chamber reduced to -1.4%, -0.2% and +1.9%, respectively. For the Markus chamber, the over-response after applied the correction was more than 5% for the four field sizes studied. To improve the accuracy of the Velkley correction [29], Gerki and Khan modified its

correction factor to take into account the effect of the collector edge-sidewall distance of the chamber, and to correct for the chamber response at different depths and different beam energies for various detector types.

Rawlinson et al [42] investigated the design features of a fixed-separation parallel-plate ionization chamber that has a negligible chamber signal of electrons from the side walls, and developed a guideline for predicting this sidewall effect. All measurements in the buildup region were performed by the Capintec model PS-033 chamber and the PTW Markus chamber for a ^{60}Co treatment machine and the 6 MV and 18 MV photon beam generated by linear accelerator. The study showed that the effect from the side wall of the chamber is primarily dependent on the ratio of the electrode separation to the wall diameter. Based on these results, it is possible to design a fixed separation parallel plate ion chamber to measure the buildup dose for the high energy photon beam and excludes the requirement of the correction factor. In the study, the correction factor was also introduced to estimate the over-response for a commercial ionization chamber under a normal build-up condition. It differs from the GK method in the parameter of the guard width that is used to characterize the proximity of the sidewall. However, this correction agrees well with the results of GK method for small collector diameter.

2.2.2   Semiconductor silicon diode

A semiconductor has the electrical conducting properties somewhere between those of a conductor and those of an insulator. Silicon, a group IV element in the periodic table, is the most commonly used as semiconductor material. It has four electrons in its outer valence band. If the impurities are added to silicon, a semiconductor with excess electrons or excess positive holes can be created (n- and p-type semiconductors, respectively). This process is known as doping. In practical, the dosimeter is classified as p- or n-type detector according to the large constituent part. A p-type semiconductor consists of silicon added a substance from group III of the periodic table, that is able to form covalent bands with silicon atom. An n-type semiconductor consists of silicon added a substance from group V of the periodic table, that are able to create free electron [31], as seen Figure 2.4.
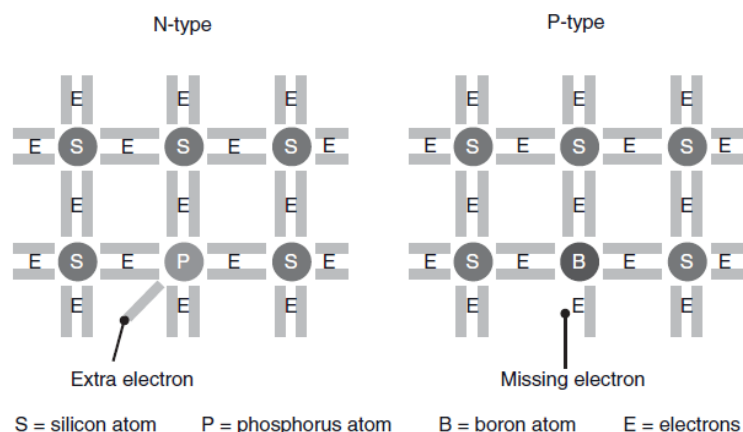
Figure 2.4. Atomic representation of n- and p-type semiconductor [31].

When a charged particle interact a semiconductor, the energy deposition always produces many electrons in semiconductor and holes in the valence band along the track of the particles. The electrons are attracted towards the positively charged impurity in the n-type silicon and the positive holes are diffused towards the negatively charged impurity in the p-type silicon. The ionization current expended by the primary charged particle to produce one electron-hole pair is proportional to the dose incidence, and can be measured using an electrometer. A p-type semiconductor is preferred in the clinical application, because of the linearity response with the dose rate [1,31].

The advantage of a semiconductor is high sensitivity, small physical size, mechanically stable, independent of atmospheric pressure, small stopping power variation with an electron energy and immediate read-out. Moreover the effective point of measurement can be located close to the surface of the detector, providing a high spatial resolution for the measurement [1,31,32]. However, it is a relative dosimeter and not be used for beam calibration. They need to be calibrated frequently with encapsulation to increase the measured precision. A significant disadvantage of diode is the non-water equivalence of the silicon, varies with the temperature and dose rate, and depends on exposed angular and energy.

2.2.3 Thermoluminescence dosimeters (TLDs)

Thermoluminescent (TL) crystals are thermally activated phosphorescence that can store the absorbed energy in the crystal lattice after being irradiated and release a visible light signal when it is heat [1]. As a dosimeter, if one can measure the amount of light emitted after TL crystal is irradiated, the exposed radiation dose can be determined. This is called a thermoluminescent dosimeter (TLD).
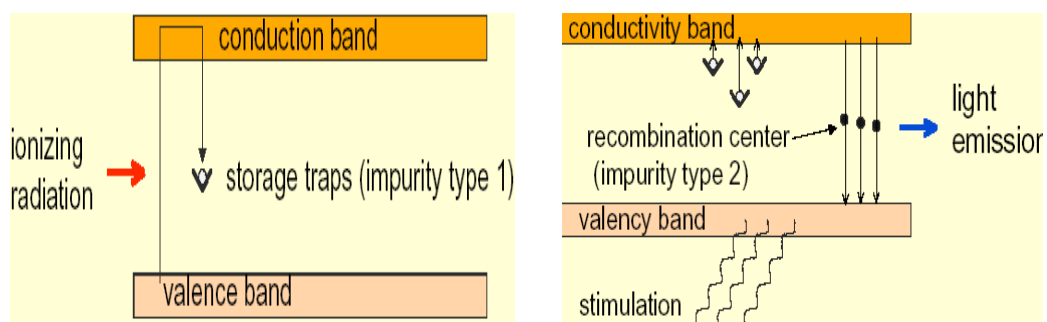
Figure 2.5. Principle of the dose measurement using the TLD [1].

When TLD is irradiated, free electrons and holes are produced. Some of the electrons in the valence band receive sufficient energy to be raised to the conduction band and return to the ground state. But a few electrons remain trapped in the forbidden region that is impurity in the crystal. The electron and hole move independently through their respective bands until an electron in the trap received heat to get out of the trap and return to the ground state with releasing the excess energy in the form of light. The emitted light signal have been measured and converted into an electronic signal by a photomultiplier tube (PMT). The total amount of emitted light will be proportional to the number of the electrons in the trap and in turn is proportional to the amount of the energy absorbed.

The most commonly used TLDs in medical application is a lithium fluoride (LiF) crystal doped with magnesium and titanium because the effective atomic number is very close to 7.4 of soft tissue and 7.78 of air. They are available in various thicknesses and forms, e.g., powder, chip, disc, ribbon or rod. It has a low rate of

fading which is generally less than 5% in 12 months. The standard TLD for photon measurement is TLD-100 which contained 7.5% ^{6}Li and 92.5% ^{7}Li which is used to measure the dose over a very wide range of 10^{-5}-10^3 Gy.

Nilsson et al [3] investigated the surface dose measurement in clinical photon beams with the different thickness of TLD and the silicon diode compared with an extrapolation chamber for the ^{60}Co treatment machine and for the photon beam energy of 6 MV and 21 MV. LiF-ribbon with a thickness of 0.9 mm (0.231 g/cm^2) and LiF-teflon disc with a thickness of 0.13 mm (0.027 g/cm^2) were used in the study. The window thickness of silicon diode was 0.5 mm water equivalent. All dosimeters were placed on a polystyrene phantom with a backscatter thickness comparable with a patient. The results showed that the TLD with a thickness of 0.9 mm and the silicon diode were not suitable for surface dose measurement. For the thin TLD with a thickness of 0.13 mm may be used to estimate the skin dose and the overestimation of the dose is less than 10% over the measured range.

Stathakis et al [23] investigated the entrance dose at the surface and the depth of 0.007 cm, and the exit dose with the TLDs measurement and the MC calculation at the square field sizes ranging from 5 to 20 cm for the 6 MV, 10 MV and 18 MV photon beams. The ultra-thin TLDs with a thickness of 0.01 cm were used for measurement the surface dose. The study found that the TLD measurement and the MC simulation were in good agreement within 2-3% excepted for a few points at the 18 MV photon beams. The accurate surface dose can be predicted by correlation between the TLD measurement and the MC calculation. The entrance surface dose increased with the field size and the angle of beam incidence. For the exit dose, it increases with field size, but decreases with the angle of beam incidence.

Although The TLDs play a useful role in the skin dose measurement on phantom or patient, they need to be calibrated frequently to increase the measured precision and need to be annealed to erase the residual signal before using [43-45]. Because the light output obtained from TLD measurement must be read by a photomultiplier, instantaneous dose reading are not possible. The management of a large number of results would be time-consuming with the delayed readings in comparison with instantaneous results from alternative dosimeters.

2.3   <u>Monte Carlo (MC) Simulation</u>

In the external beam radiotherapy, photons interact with surrounding matter via four main processes; Rayleigh scattering, Photoelectric absorption, Compton scattering and Pair production [1]. The electrons, occurred from the last three collision types, pass the matter and lose energy by the inelastic collision and the radiative interactions with the atom and molecules in the medium. Although the physics of the various interactions in matter is well understood, it is impractical to develop an analytical expression to describe these. The MC simulation is a solution method of the transport problem of these particles in matter. It is generally considered to be an accurate tool for dose estimation in radiotherapy, since the beam's particles are tracked individually in the media according to the reliable interaction database [46-48]. The results have been used for radiation dosimetry protocols and served as the gold standard in many situations, especially in the heterogeneities region or in the regions where the calculation algorithm are in adequate [48-51]. The disadvantage of the MC method is the long calculation times required to obtain the meaningful results.

The MC simulation is a theoretically algorithm that relies on the probability law controlling the individual interactions of electron and photon in material and the repeated random sampling process with pseudorandom numbers according to cross-section data to simulate the radiation transport. All particles are tracked through the transport until the original particle and secondary charged particles escape outside the interested geometry, locally absorb in the medium and the residual energy drop below the energy threshold. In the past, the MC simulated process is an analog simulation (interaction by interaction techniques), typically used for the transport of neutral particles [30]. It can be done by determine the distance of the photons go to the next site of interaction for choosing the interaction type, and then simulate the particle transport by selected interaction. Because all interactions including those of secondary particles are explicitly simulated, it is not practical due to the large number of interactions.

Therefore, all general purpose MC codes employed a condensed history schemes for charged particle transport [30]. The first condensed history technique was described by Berger et al [52]. Because the vast majority of electron interactions lead

to very small changes in the electron energy and/or direction, the effects of many scattering events can be grouped into relatively few condensed history steps, and their cumulative effect taken into account by sampling energy, direction, and position changes from appropriate distributions of grouped single interactions, as shown in Figure 2.6.
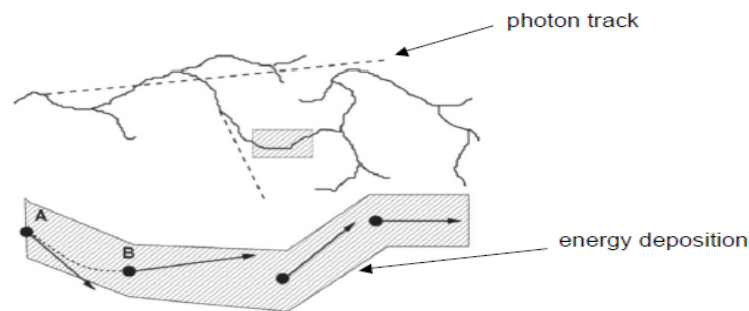
Figure 2.6. Illustration of the condensed history technique [30].

Several general purpose MC codes are publicly available such as EGS, MCNP, ETRAN, PENELOPE etc. EGSnrc is one of the codes that most frequently used for modeling the electron and photon transport in medical physics applications [53]. The multiplication version of EGSnrc is called as EGSnrcMP [54]. This feature has been implemented in the standard suite of EGSnrc user codes. This code is written in the FORTRAN programming language, run under the Linux or Window operating system and worked at the energy range of 1 keV to 10 GeV. It can be divided in two main sub-codes: BEAMnrc and DOSXYZnrc code [55-57]. Both codes are based on an electron gamma shower (EGS) user code.

2.3.1 BEAMnrc and DOSXYZnrc user code

The BEAMnrc [56-58] is a MC code built on the EGSnrc code system which was developed as part of the OMEGA project. It is based on the PRESTA extension and is applicable to model the realistic radiation beams from clinical radiotherapy accelerators, including low-energy x-rays, as illustrated in Figure 2.7.

In the BEAMnrc code, the accelerator head is built from a series of individual component modules (CMs) with a specify class of geometric shape within the horizontal band. These can be re-used several times in the accelerators and each of which has two surfaces in which perpendicular to the z-axis of the accelerator. The input file for each region which specifies all the details about the various components in the particular accelerator head, the parameters controlling the radiation transport modeling and the various variance reduction techniques to enhance the efficiency of the simulation, must be defined [58-62]. A large quantity of data related to photon and electron cross sections that generated by a PEGS4 data package for the specific materials in the accelerator model were read by the code during the execution stage.

.
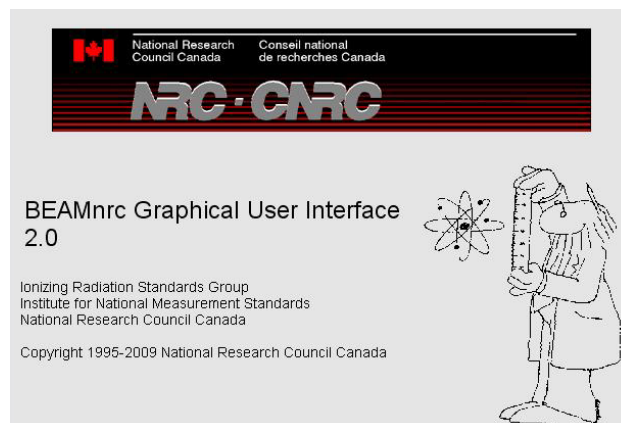
Figure 2.7. BEAM/EGS4nrc MC simulation code [56].

Most commonly the incident particles are high energy photon beams created by the electrons interaction with the target. The dose distribution was made to uniform across the field using a flattening filter and then shaped by the collimator jaws or the multi-leaf collimator (MLC). The particles passed through the various components inside the accelerator, and were scored in the scoring planes located at the back plane of CM. This plane is divided into angular regions around the central ray. The system refers to each random particle including its secondary product, as a history. A summary data of each plane consist of the charge, number, position and angle of particles, the deposited energy, and the radii (half-widths) of the scoring zones

followed by the actual fluence results. The primary output files derived from BEAMnrc code is a large file containing the phase-space information about all the particles. This file can be used directly in further BEAMnrc calculation or used as an input file to DOSXYZnrc.

The DOSXYZ code [57-63] is the part of the OMEGA-BEAM system, developed at NRC for calculating dose distribution in a rectilinear voxel of the phantom or the CT data set. A variety of incident beam, density and material in every voxel can be varied. The system handles the complexities of the accelerator beam coming in an arbitrary angle and the problem of defining the materials and densities to be used in the MC simulation based on the CT data. It requires one input file to be generated by user. The statistically significant results of MC calculations are obtained from the sufficiently number of incident particles. The histories number that required in each run to get desired statistical uncertainty depended on field size, voxel size and photon energy. Because of the fewer deposited dose in the smaller volume, the reducing of voxel sizes will increase the uncertainty for a fixed number of incident particles. Therefore a large number of histories were required to obtain less than 1% statistical uncertainty in the smallest voxels of each simulation in the build-up region. The typical values of voxel sizes are 2-5 mm and 1-2 mm for the field sizes greater and smaller than 3×3 cm^2, respectively [30].

In this code, the statistical analysis is based on a history by history method. The history by history method, described by Sempau et al [64], is an estimating uncertainty method that implemented in BEAMnrc and DOSXYZnec code. This method is well known and has been used for years in other MC codes such as MCNP. It involves grouping scored quantities, according to primary history during a run and determining the root mean square standard deviation on the mean of the groupings. Normally, there is no difference between a primary history and an incident particle. However, the grouping according to primary history is important where more than one incident particle can be tracked back to a single primary history. The equation can be written as:

$$\overline{X} = \sqrt{\frac{1}{N-1}\left(\frac{\sum_{i=1}^{N}X_i^2}{N} - \left(\frac{\sum_{i-1}^{N}X_i}{N}\right)^2\right)} \qquad (3)$$

where N is the number of independent histories, X_i is the value of X in history i and $\overline{X}$ is the mean value of X evaluated total number of histories.

This method greatly reduces the uncertainty in the uncertainty estimation, eliminates one dimension from all scoring arrays, decreases the required memory by a factor of two and takes into account the correlation between the incident particles and the phase space sources.

Although the MC method has become a standard tool for dose verifications, an undesirable discrepancy between measurement and MC derived-simulation has been reported in the initial build-up region, where MC shows significantly lower dose [33,65,66]. However, the recently studies [34,67,68] have demonstrated the coherence between the MC simulations and the measurements using an extrapolation chamber.

A study of Abdel-Rahman et al [66] validated the MC calculated dose in the buildup region for the 6 and 18 MV photon beams generated by a Varian Clinac linear accelerator. Generally the percentage depth dose in medium was equal to the percentage depth ionization (PDI) in high energy photon beam. Because the perturbation factors in the buildup region were strongly influenced by the type of ionization chamber and the different ionization chambers may give different PDIs, a raw comparison of MC calculated PDDs with corresponding uncorrected PDI measurements in the dose buildup region for photon beams may displayed significant discrepancies. In the study, the measurements were done by a TLD-600 and TLD-700 with a thickness of 0.15 mm^3, a 0.12 cm^3 cylindrical and a Roos parallel plate ionization chamber in solid water with a phantom-embedded extrapolation chamber (PEEC). The PEEC has a parallel plate geometry that can be varied the electrode separation ranging from mm to about 1 cm. The discrepancy between the measured PDI with the PEEC and the MC calculated PDD at the depth of 50 μm for a 10×10 cm^2 field at the 6 MV photon beam was about 17.5% versus 12.8%, respectively. The MC calculated PDI was also compared with the measure PDI in order to validate the

accuracy of the MC calculation. The results showed that the discrepancy of the measured and calculated PDI at the 50 μm depth was within 1% (17.5% versus 16.1%, respectively) for the 6 MV beam, while a significant difference was still observed for the 18 MV beam because of the contaminating neutrons and protons. For 6 MV photon beam, the MC calculation was an accurate method to determine the dose distribution in the buildup region.

Devic et al [67] investigated the deposited dose within the first millimeter of the build-up region and the last millimeter of the build-down region using several dosimeter types and MC simulations, and determined a corrected procedure to obtain an accurate skin dose based on radiochromic film measurements for the 6 MV photon beam. Three types of the new Gafchromic dosimetry film (HS, XR-T, and EBT), an Attix parallel plate chamber, a home-built extrapolation chamber and TLD were used to measure the percentage depth dose in the build-up region. The film has an effective point of measurement at depth slightly larger than 70 μm and the range of the effective points of measurement for all dosimeters used in this study was varied from 0.004 mm up to 1.2 mm. The EGSnrc MC code was also used to calculate the absorbed dose in the build-up region. In the build-down region, the EBT film strips were used to measure the percentage depth dose. The results obtained from the study showed that a relative large correction (15%) should be applied when using the film. The correction factor for the TLD, depended on the TLD thickness, is 0.810 for a thickness of 0.15 mm or 0.586 for a thickness of 0.4 mm. For the MC simulation, the percentage depth dose agreed well with the measurement, excepted at the depth below approximately 10 μm.

While Parsai et al [37] studied the variation of the percentage depth dose in the build-up region using MC simulation for the 6 and 10 MV photon beams from two commercial accelerators in comparison with the derived data using an extrapolation chamber (Far West Technology), a Markus parallel plate chamber and a conventional 0.125 cm^3 cylindrical chamber. The window of extrapolation chamber was made of 6.9 mg/cm^2 polyethylene. The measurement of collected charge was done in a solid water phantom for specific depths at source to skin distance of 100 cm. The reading was obtained by varying the plate separation from 0.65 to 4.65 mm and then fitted the measured percentage depth dose with linear regression equation. The BEAM/EGS4

code system was also used to simulate the 6 and 10 MV photon beams from a Varian Clinac and an Elekta linear accelerator. The simulated phantom was modeled using DOSXYZnrc code with a central axis voxel size ranging from $1\times1\times0.05$ to $1\times1\times0.1$ cm^3 along x, y and z directions respectively. When compared with the extrapolation chamber, the dose at the surface obtained from an uncorrected parallel plate ion chamber at the field size of 10×10 cm^2 overestimated by 30-40% for the 6 MV and by 20-30% for 10 MV photon beam. The difference between the extrapolation chamber and the uncorrected parallel plate chamber reading decreases when increased the photon beam energy. The equation proposed by Gerbi and Khan was used to correct the reading from parallel plate chamber. After applied the correction factor, the maximum deviation of the measured dose using the extrapolation chamber and the corrected parallel plate chamber was 2.4% and 3.2% for the 6 MV and 10 MV photon beam, respectively. Comparison between the percentage depth dose derived from the MC and the measurements indicated that the calculated surface dose agreed well with the measured surface dose using the extrapolation chamber. In additional, a study by Ding et al [65] presented the calculated percentage depth dose in the buildup region with the DOSXYZ/EGS4 and the DOSRZNRC/EGSnrc gave significantly lower than the measured percentage depth dose. Both studies suggested that the dose at the surface and a few mm beneath is significantly lower than the conventional accepted values.

In the recently study, Kim et al [68] investigated the effects of the electron transport algorithms at the buildup region in a homogeneous water phantom and also in a heterogeneous phantom using the EGSnrc code. The investigated algorithms and parameters included the boundary crossing algorithm (BCA), the electron step algorithm (ESA), the global electron cutoff energy (ECUT) and the electron production cutoff energy (AE). For the MC simulation, all surface doses were scored at or near the phantom surface and normalized to the depth of maximum dose. For the measurement, the surface doses were obtained using an Attix parallel plate ionization chamber and a EBT2 radiochromic film for the 6 MV photon beam generated by the Varian Clinac accelerator. The effective point of measurement for Attix chamber and EBT2 film was the depth of 48 and 95 μm respectively. The study displayed that the variations were found to be larger than 10% for different user-

specified transport parameters. They also found that using EXACT option for BCA and PRESTA-I option for ESA in BEAMnrc code gave the best accurate results and reduced the time in calculation buildup doses. Although the higher ECUT and AE of 0.711 MeV can improved the computing efficiency by more than half, there was an approximately 6% underestimate in calculation at the depth less than 0.1 mm. The comparison between the MC calculated doses and the measured data using both of an Attix ionization chamber and a EBT2 film was in good agreement to within 2.5% with no other corrections applied. For the heterogeneous phantom, the surface dose derived from the MC calculation using the PRESTA-I option for BCA agree with the EBT2 measurement within 2.7%, but it overestimated the surface doses by up to 4%.

2.4   <u>Equivalent square field</u>

Typically the beam data from the medical linear accelerator was generally collected for various square field sizes in order to reduce the measurement time, however the treatment field in clinical application often used in the rectangular size. For calculation purpose, it is customary to find a square equivalent to rectangular field for a specific dose parameter.

The equivalent field method is based fundamentally on Clarkson's integral in 1941. The study showed that an integration involving the scatter-radius function can be used to calculate the scatter dose in any field. The précised value of the equivalent field size derived from the scatter-radius function depends on the radiation quality, the depth and the source-surface distance. The equivalent field is defined as the standard field which has the same characteristic of the percentage depth dose at the central axis as the given non-standard field [69]. The use of the equivalent field is a simple method for obtaining the standard parameters for the treatment machine such as percentage depth dose, tissue air ratio, head scatter factor and output factor, and for increasing the calculation speed in rectangular fields. For example, the head scatter factor from a given rectangular field can be related to the square field by the well-established equivalent square relationship; in the form of the equivalent-square table [69-70], the area-to-perimeter formula [71-72], the empirical formula [73-74] and the geometric formula [75]. Therefore the data for rectangular fields can be obtained

using the data of equivalent squares or circles. For the photon beams, this method has been demonstrated to give satisfactory results including in the buildup region.

The practical method for determination of equivalent square fields was the using of the equivalent square table and the area to perimeter formula. The table of equivalent squares was calculated from an integration involving the scatter-radius function as given by Day et al [69]. The area to perimeter method is based on the assumption that the square and rectangular fields are equivalent if they have the same area to perimeter ratio. The results derived from both methods have been shown to be sufficiently accurate for clinical purposes over a wide range of depths and photon beam energies. Practically, the formula is more favorable than the table due to its simplicity of use. A side of equivalent square (L_{sq}) is calculated by

$$L_{sq} = \frac{2 \times L_x \times L_y}{\left(L_x + L_y\right)}$$ (4)

where L_x and L_y are the field's side as defined by the X- and Y-collimator, respectively. This formula includes the effect of field size elongation. However it works well for moderately elongated field but is doubtful if the field length over the field width exceeds 2 or either L_x or L_y exceeds 20 cm. Obviously, L_{eq} is invariant under an interchange between L_x and L_y. Therefore, this formula does not include the effect of collimator exchange. It also does not include the effect from the beam's energy, the configuration of each treatment unit, and the calculated depth.

Many previous works have been done to improve the accuracy of the equivalent field method. In 1993, Vadash and Bjarngard [73] proposed an empirical formula in an attempt to account for the collimator-exchange effect on the head scatter factor. The equivalent square collimator setting is given by

$$L_{sq} = \frac{\left(A+1\right) \times L_x \times L_y}{\left(AL_x + L_y\right)}$$ (5)

where *A* is a parameter specific for each beam. This parameter is determined by minimizing the average difference between the calculated and measured head scatter factors of the rectangular field. The formula is deduced to that of area-to perimeter when *A*=1. The beam's energy, the configuration of treatment unit as well as the calculated depth are included in this empirical formula since the parameter is determined using the specific beam data.

Similarly, Kim et al [75] proposed the geometric formula which accounts for both the effect of field elongation and collimator exchange based on the linac head's geometry using the field mapping method for the calculation of an equivalent square field. The derived formula has the same format as the empirical formula. The parameter '*A*' is replaced by the geometric parameter '*k*' which is obtained from the distances between the target and the top of each collimator jaw and between the bottom of each collimator jaw and the detector plane. Therefore, this formula includes the effect from collimator exchange, the configuration of a linear accelerator treatment head, and, also, the depth. The accuracy of the head scatter factor prediction for both open and wedged rectangular fields is within 1%. However, the beam's energy is not accounted for in this formula.

However, a study on the equivalent square approach for predicting the surface dose from rectangular photon beam is very limited. To our knowledge, there has been only one statement of Day and one study by Gossenlin et al [76]. The study of Gossenlin verified the generally validity of the equivalent field method to predict the depth of dose maximum and the surface dose for rectangular fields. All measurements were done in solid water phantom by using as Attix parallel plate ionization chamber at the 6 MV, 10 MV, and 18 MV photon beams generated from Varian Clinac linear accelerator. The various square and rectangular fields with elongation ratios ranging from 1.5 to 27 were measured in the study. In this study, the reliable alternative method to determine the surface dose from rectangular photon beam is introduced in order to replace the measurement. For all energies, the same depths of dose maximum and the surface dose as their corresponding equivalent fields were observed for the rectangular field with elongation ratios below 2. For the rectangular field with elongation ratios above 2, the difference of the surface dose of the rectangular fields and of their corresponding equivalent field was observed especially in the 18 MV

photon beam. The depth of dose maximum shift toward the surface and the surface dose increase due to the secondary electrons scattered in a larger surface area of the collimator. These effects were more pronounced when defined the long axis of the field by the upper jaws and the collimator exchange effect did not influence the dose at the surface.

2.5   **The acceptability of criteria**

Dosimetric accuracy required for the purpose of treatment planning has been discussed in several papers. Normally, the criteria recommends for the dose calculation derived from the computerized treatment planning system (TPSs). The most extensive sets of criteria have been published such as Van Dyk et al [77], AAPM TG 53 [78], Venselaar et al [79] and IAEA TRS report no.430 [80]. The recommendation report of IAEA TRS report no. 430 is presented in Table 2.1. In this study, the presented criteria intends for indicating the guidelines of acceptable deviation between the measured and calculated data obtained from MC simulation in the buildup region.

Table 2.1. The criteria for acceptability, as published in IAEA
TRS report no 430 [80].

Location	Simple geometry (homogeneous)	Complex geometry (inhomogeneity)	More complex geometry (combinations of 1 and 2)
Central beam axis	2%	3%	4%
Buildup region of central axis and penumbra region of profiles	2 mm or 10%	3 mm or 15%	3 mm or 15%
Outside central beam axis	3%	3%	4%
Outside beam edges	3% (30%)	4% (40%)	5% (50%)

CHAPTER III

METHODOLOGY

3.1   MATERIALS

3.1.1   MC simulation code

The MC simulation based on the EGS4nrc (Electron Gamma Shower) code system, developed by the National Research Council of Canada (NRC), was used in this study. EGS4nrc code is widely used in many areas of medical physics and divided into two main sub-codes. The BEAMnrc and DOSXYZnrc code system are used for simulating in radiotherapy beams and for calculating the dose distribution in phantom or in patient, respectively. These codes are written in the FORTRAN programming language and can be run under the Linux or Window operating system. They are free for non-commercial use and are limited to photon and electron beam in the energy range of 1 keV to 10 GeV.

The CPU used for the simulation with the EGS4nrc code is Intel-Pentium Core 2 at 2 GHz processor running on Redhat Linux 5.0 Professional.

3.1.2   Linear accelerator

The linear accelerator used in this experiment is Varian Clinac 23EX with on-board imaging system, manufactured by Varian Oncology Systems, Palo Alto, CA, as shown in Figure 3.1. The linac can produce dual photon beam energies of 6 and 10 MV, and six electron beam energies of 6, 9, 12, 15, 18 and 22 MeV. The photon field sizes can be varied ranging from 1×1 cm^2 to 40×40 cm^2 at the isocenter and 6×6 cm^2 to 25×25 cm^2 for electron applicator sizes. The distance from the target to isocenter is 100 cm. The dose rates have range from 100-600 monitor units per minute at standard target to surface distance. The MLC has the maximum number of 120 tungsten leaves which mounted below the conventional collimator at the same direction of X-jaws.

Figure 3.1. Varian Clinac 23EX linear accelerator.

3.1.3   Blue water phantom

The Blue phantom (Scanditronix Wellhofer Dosimetric, Schwarzenbruck, Germany) is made from acrylic plastic (Perspex), having the scanning volume of $48 \times 48 \times 41$ cm^3, as presented in Figure 3.2. In the experiments were used the scanning resolution of 2 mm and medium scan speed (5.13 mm/s). The position accuracy and the reproducibility of the scanning system is ± 0.5 mm per axis and ± 0.1 mm, respectively. It can be operated by the OmniPro-Accept software version 6.1 (IBA Advanced Radiotherapy, Scanditronix Wellhofer, Uppsala, Sweden). This phantom can be used for collecting the beam data from treatment machine such as the percent depth dose and the beam profile, measured with a compact cylindrical ionization chamber and a silicon p-type photon semiconductor dosimeter, respectively.

Figure 3.2. Blue water phantom.

3.1.4   Solid water phantom

Figure 3.3 displayed the solid water equivalent phantom slab (RMI, Model-457) is made in square size of 30×30 cm^2 with the thickness of 0.2, 0.3, 0.5, 1.0, 2.0 and 5.0 cm was used in this study. The physical density of solid water is 1.04 g/cm^3. It composes of the epoxy resin and powders in order to control the density and radiation properties.

Figure 3.3. Solid water phantom slab.

3.1.5 Compact cylindrical ionization chamber type CC13

Figure 3.4 show the compact cylindrical ionization chamber of type CC13 (Wellhofer Scanditronix, Germany). The CC13 dosimeter is the standard chamber for clinical application in water phantom. The outer and inner electrodes are made of Shonka C552. The chamber has a sensitive volume of 0.13 cm^3, a total active length of 5.8 mm, a cylindrical inner diameter of 6.0 mm, a wall thickness of 0.070 g/cm^2, and a reference point in water from the chamber distal end of 3.5 mm. The dosimeter can be operated with the Blue water phantom polarizing voltage in continuous scanning mode.

Figure 3.4. 0.13 cm^3 cylindrical ionization chamber type CC13.

3.1.6 The CU500E electrometer

The CU500E control unit has a built-in dual channel electrometer with reversible polarity and auto ranging for setting. The system is controlled by OmniPro-Accept software version 6.1. This electrometer is used with a compact cylindrical ionization chamber and a silicon p-type photon semiconductor dosimeter for measurement.

3.1.7 Silicon p-type photon semiconductor type PFD[3G]

Figure 3.5 show a silicon p-type photon semiconductor dosimeter type PFD[3G] (Wellhofer Scanditronix, Germany). The PFD[3G] dosimeter has an active diameter of 2 mm, a thickness of chip of 0.5 mm and an effective thickness of 0.06 mm from the detector front surface.

Figure 3.5. PFD[3G] dosimeter.

3.1.8 The Markus Parallel-Plate ionization chamber and DOSEI electrometer

A parallel-plate ionization chamber type Markus 23392 (PTW-Freiburg, Germany) consist of graphite polyethylene foil window and graphite polystyrene collector. The plate separation is 2 mm, with a 0.35 mm distance between the side wall and the collector. The guard ring width is 0.2 mm. An active diameter is 5.4 mm. The effective measured point was assumed to be at the bottom of the entrance window electrode.

The electrometer type DOSE1, IBA dosimetry, is used with Markus chamber type 23392. The polarizing voltage is produced by a DC/DC converter from a 5V internal supply voltage. The polarity voltage can be programmed in the range of 100-600 V with polarity either negative or positive. The measured polarizing voltage with Markus chamber is 300 volts. The reading can be presented in terms of nanocoulomb.

Figure 3.6. Markus parallel plate ionization chamber with DOSE1 electrometer.

3.1.9   Thermoluminescence dosimetry system

The TLD dosimetry system consists of TLD dosimeter, a TLD reader and TLD oven. The TLD chips used in this experiment are the lithium fluoride (LiF) crystals doped with magnesium and titanium (LiF: Mg, Ti) known as TLD-100. The TLD has a density of 2.64 g/cm^3 and effective atomic number of 8.2. Their thickness is 0.39 mm with a 9.92 mm^2 surface area (3.15×3.15 mm^2). The effective point of measurement was assumed to be at the middle of its thickness.

Figure 3.7. HARSHAW TLD-100 chip with TLD reader.

The TLD auto reader (Model LQS 5500: HARSHAW Chemical Company, Solou, OH), operated by WinREMS software version PL-26732.8.1.0.0, was used in the study with the TLD chips dosimeter. It is capable of reading 50 dosimeters per loading and can be used for various shapes of TLDs such as chips, rods, and cubes in a variety of sizes. It uses hot nitrogen gas heating with a closed loop feedback system that produced linearly ramped temperatures accurate within ±1°C to 400°C. The output data is presented in the form of heating profiles and glow curves.

3.2   <u>METHODS</u>

The Varian Clinac 23EX linear accelerator, equipped with a Millennium 120-leaf MLC and on-board imaging system, located at the department of radiation oncology, Siriraj hospital, was used in this study. All experiments were performed on the 6 MV photon beam.

3.2.1   <u>MC simulation with BEAMnrc and DOSXYZnrc codes</u>

The 6 MV photon beam generated from a Varian Clinac 23EX medical linear accelerator was simulated using the BEAMnrc user code. The dose distribution in a phantom was obtained by the use of DOSXYZnrc user code.

3.2.1.1 Linear accelerator modeling with BEAMnrc code

The first step of the MC simulated method is to model an appropriate representation of the beam for a given geometry of linear accelerator head, based on the specification data from the manufacturer, using BEAMnrc code in terms of the individual CM. The procedures are listed below.

1. Select the file from $EGS_HOME/beamnrc/spec-modules directory, and then choose the CMs to add and specify the accelerator. A window will appear with the necessary parameters entry boxes for the CMs such as the physical geometries, the materials, the densities and the transport parameters. Each CM was perpendicular to the z-axis and not overlaps between two planes, and can be used in a wide variety of applications. In this study, the SLABS CM was used for the target, CONS3R for a primary collimator, SLABS for a vacuum window, FLATFILT for a flattening filter, CHAMBER for an ionization chamber, MIRROR for a mirror, JAWS for a secondary collimator, and DYNVMLC for a multileaf collimator. For a more information of linac's head modeling was presented in the Appendix B.

2. Loaded the cross sectional data, created by the code PEGS4, from $EGS_HOME/pegs/data directory. These data based on the density effect corrections in ICRU report 37. The energy range is from the AE values of 521 or 700 keV up to 55 MeV.

3. Entered the input file to define the number of histories, the type of the source incident and storing data, the running method, the variance reduction technique, the presented output, and to specify the simulated parameters. Moreover the random numbers are defined for making the decisions about the simulated process of the individual particles. The number of simulation events was set to be about 10^9 histories for all conditions in order to achieve 1% statistical uncertainty for all voxels.

4. For the EGSnrc transport parameters, it allows to adjust within the "Main Inputs" window. The default settings of EGSnrc parameter in the code should be adequate for running except in low energy application. The particular parameters used in the BEAMnrc user code for generating the phase-space files and in the DOSXYZnrc user code for calculating the deposited dose in medium were as follows:

   a. AE = 0.521 MeV; AP = 0.001 MeV
   b. ECUT = 0.521 MeV; PCUT = 0.001 MeV
   c. Global SMAX = 5.000; ESTEPE = 0.25
   d. BCA = EXACT
   e. ESA = PRSTA_II
   f. Spin effect switched on.

   To specially calculate the surface dose, both the ECUT and AE values were lowered to 521 MeV. The particle's transport is terminated and its residual energy is transferred in the current region when the total energies of the electron and photon are less than the value of ECUT and PCUT, respectively. The production of secondary particles is considered if the particle's total energy is greater than AE for the knock-on electrons and greater than AP for the bremsstrahlung photons. For a more information of EGSnrc transport parameters was presented in the Appendix A.

5. The outputs of BEAMnrc code are shown as the listing, graphics and phase space files. The phase space data contained the data about each individual particle crossing the scoring planes, was recorded on the plane perpendicular to the beam-axis at 90 cm source to surface distance (SSD). The accurate phase space simulations depend on the accurate input parameters. It can be used in off-line analysis program, or fed directly into the DOSXYZnrc to calculate the dose distribution in the phantom or CT data. In this study, the average scored particle in each phase space file was about 5×10^7 events. The number of history per 1 hour of CPU time for the 6 MV photon beam was 1.5 million histories for the larger field.

3.2.1.2 Illustration of the accelerator's head modeling in BEAMnrc code

The linac's head components of Varian Clinac23EX were created individually using BEAMnrc code in terms of the CMs, as shown in Figure 3.8. Each color represents the different materials. The surrounded area and the area between the CMs were set to be an air. The front surface of the target at the coordinate system (x,y,z) = (0,0,0) is the origin where the initial electrons are incident. The target of this linac, the most dominant factors to the energy spectrum, is made of copper for the 6 MV photon beam. The primary collimator, a circular cone with the apex located at the electron beam striking point, is made of tungsten. For more details, see Appendix B.
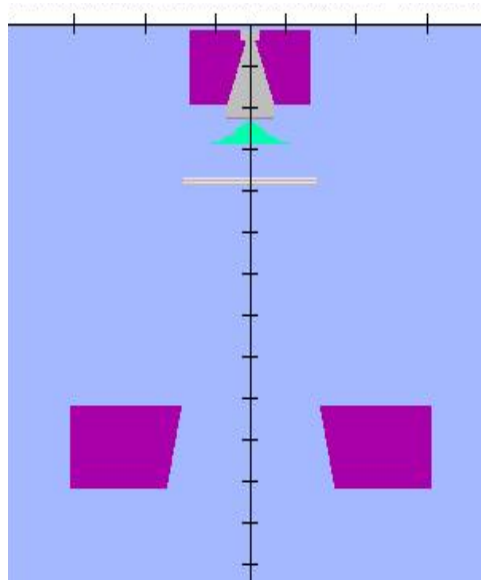
Figure 3.8. Illustration of the geometry of an accelerator head and
its CM in XZ plane.

Because the flattening filter is a main cause of the electron contamination in photon beam, the exact geometry and density of the filter is important [10,12-16,25]. In medical linear accelerator, a conical flattening filter is used for filtering the intensity of photon by removing low energy photon to produce the flat radiation beam. Because the bremsstrahlung spectra are harder at the center and softer at the edge of radiation beam, the shape of flattening filter is thicker in the middle and thinner near the edge, as shown in Figure 3.9. It is the most dominant factors to angular distribution, and is made of copper, low-z material. For more details of input file, see Appendix B.
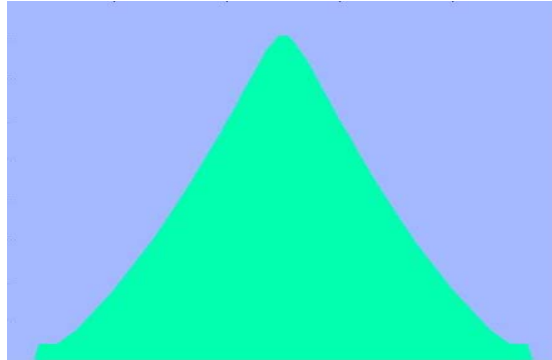
Figure 3.9. Illustration of FLATFILT CM for modeling the flattening filter of the 6 MV photon beam.

Secondary collimator follows the divergent shape of the primary collimator, and is made of tungsten. It consists of the upper and lower part located at the different level and independently moved in the Y- and X-direction, respectively. It was simulated by JAW CM, and shown in Figure 3.10. More details were presented in the Appendix B.
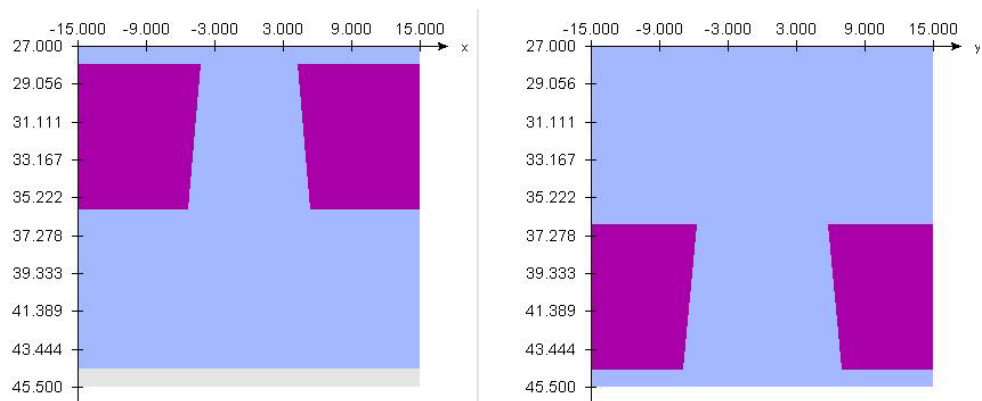
Figure 3.10. Illustration of JAW CM for modeling the secondary collimator of the 6 MV photon beam.

Although, the studied field sizes were defined using the secondary collimator, the Millennium 120 MLC was also created with DYNVMLC CM that can model the exact geometry of these leaves. The MLC were modeled after JAW CM, and was made of tungsten. The 120 tungsten leaves (60 per side, denoted as bank A and bank B) are rounded-end, and the leaf sides are tongue and groove design. The 40 central leaves project to 0.5 cm width at isocenter and the 20 outer leaves project to 1.0 cm width at isocenter. The thickness and material of individual leaf, the length and width of tongue and groove, the rounded leaf end, the air gap between the leave, the leaf tips, the driving screw holes and the supporting rail grooves can be defined in DYNVMLC CM, as shown in Figure 3.11. For more details, see Appendix B.
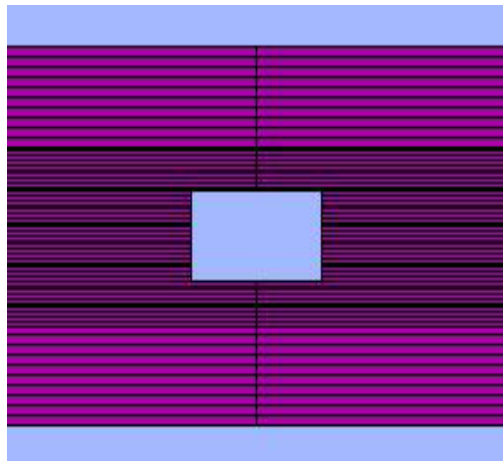
Figure 3.11. Illustration of DYNVMLC CM for modeling the
Millennium 120 MLCs.

3.2.1.3 Dose calculation in phantom with DOSXYZnrc code

Using the phase space file obtained from the BEAMnrc code as the input for the DOSXYZnrc code, the beam's interaction in the water phantom was simulated and, hence, the deposited dose within a voxel was obtained. To receive the accurate result, the size of simulated phantom should be matched with the size of the measured phantom. An approach consist of

1. Created an input file and loaded the PEGS4 cross sectional data in DOSXYZnrc code.

2. Entered the input file to define the source parameter, the definition of phantom and the simulation parameters. The transport parameters were similar in the BEAMnrc simulations. The phase space files obtained from the BEAMnrc code are used as the input source files for the DOSXYZnrc code to simulate the passage of source particles through phantoms. For the transport parameters, they are also defined in the same information within the BEAMnrc code.

3. The phantom is created in voxel by voxel of variable density and composition to calculate the deposited dose in medium. The number and the size of voxel dimensions in the x, y and z directions are specified. The geometries of phantom in x,y,z axis were defined as the in-plane, cross-plane and in-beam direction, respectively. To minimize the total number of voxel and maintain the good resolution, the voxel were divided into unequal size. The origin of the phantom was set at the center of radiation field.

For determination of the build-up dose, the size of water phantom was $30 \times 30 \times 20$ cm^3. To achieve reliable calculated result in this region where the electronic equilibrium of charged particle is not present, the voxel dimension should be small in the z plane and wide in the xy plane. Because the statistical uncertainty for the deposited dose in voxel sizes depend on the number of simulation event, the voxel size along the beam central axis from the phantom's surface to a few millimeters depth was set to 1x1x0.014 cm^3 for the 3×3 cm^2 and 5x5 cm^2 field size and $3 \times 3 \times 0.014$ cm^3 for other larger field sizes in the x,y,z direction, respectively.

4. The outputs are presented in the form of .3DDOSE file. It consists of the phantom data, the deposited values and the simulated error in each voxel.

5. The ".3DDOSE files" were analyzed and compared with the measured data. For details about 3DDOSE files, see Appendix C.

3.2.1.4 Determination of the initial beam parameter

Since the actual information about the incident electron beam on the target inside the linac was experimentally unknown in our study, the energy and radius distributions of the electron striking the target were varied to produce the best match between the simulated and measured results. In the study, the initial electron energy is assumed to be a monoenergetic circular beam with Gaussian distribution in x and y axis. The field size of 10×10 cm^2 and 30×30 cm^2 were used to determine both of incident electron energy and the radius distribution of the beam. The incident electron energies were varied from 6.0 to 6.5 MeV for matching with the percentage depth dose along the central axis measured by CC13 ionization chamber in the blue water phantom. The radius distributions were adjusted with the range of 1.0 to 1.6 mm to match the calculated beam profile with the beam profile measured by PFD[3G] dosimeter at the 10 cm depth.

For matching the calculated and measured data, the size of calculated water phantom was $60\times60\times40$ cm^3. Because of the limitation of total number of voxel, the voxel dimension for determination of the percentage depth dose was varied in the z axis. The voxel dimension around the central axis was $1\times1\times0.2$ cm^2 at the depth between 0 to 4 cm and $1\times1\times1$ cm^2 at the depth between 4 to 40 cm. For the beam profile calculations, the profiles were calculated at the depth of 10 cm. The voxel dimension was varied in the x axis and set to $1\times1\times1$ cm^2 and $0.5\times1\times1$ cm^2 in the field and in the region ±5 cm from the field edge, respectively. Optimal incident electron energy and radius distribution based on matching results were used for simulation the dose at the surface and the buildup region in the studied field sizes.

3.2.2   Measurements

3.2.2.1 Measurement of the PDDs and beam profiles using CC13 and PFD[3G] dosimeter

For obtaining the optimum parameters of initial electron energy and radius distribution of the simulated beam, the percentage depth dose (PDD) and the beam profiles for 6 MV photon beams were measured for the field sizes of 10×10 cm^2 and 30×30 cm^2 with the SSD of 100 cm. The CC13 and PFD[3G] dosimeter is recommended for measurement the PDD and the beam profile, respectively. These were mounted on a computer controlled scanning system in Blue water phantom. The effective point of measurement for each dosimeter was set at the central axis of beam. The PDDs were measured in the z-direction along the beam axis from the surface down to 30 cm depth, and were normalized to the depth of 1.5 cm for both of field sizes. The beam profiles were measured by scanning across the field area at the depths of 10 cm. Only the movable jaws were used to define the field size for measurement. The results of PDDs and beam profiles were compared with the values of simulation at the same field size and depth to indicate the suitable incident electron energy and radius distribution of the simulated beam.

For determining the dose at the surface and the buildup region, the PDDs at the square field sizes of 5×5, 10×10, 15×15 and 20×20 cm^2 defined by the movable jaws were measured by using a CC13 and PFD[3G] dosimeter in the blue water phantom at the depth ranging from 0 to 3 cm. All measurements performed at the standard SSD of 100 cm. The PDDs were normalized to the depth of 1.5 cm for all field sizes, and compared with the calculated percent depth dose from the MC method.

3.2.2.2 Measurement of the PDDs using Markus chamber

The central axis depth doses were obtained using the Markus chamber in $30\times30\times20$ cm^3 solid water phantom. The back of chamber had sufficient tissue-equivalent material to ensure that all electrons backscattered into the collecting volume were collected. For all measurements, the chamber was

imbedded in the solid phantom to provide a close fit during the measurement and placed in the same plane of the phantom surface. The doses at the depth of 0, 0.2, 0.3, 0.5, 1, 1.2, 1.5, 2 and 3 cm were measured by adding the solid water slabs over the chamber without the protective cap, while maintaining the SSD of 100 cm at the top of the phantom. The effective point of measurement of Markus chamber followed the recommendation of the IAEA TRS398 was the point below the top of polarizing electrode [81].

Measurements were performed for square fields and rectangular fields at the field ranging from 3×3 cm^2 to 25×25 cm^2. The exposed dose was set to be 100 monitor units (MU). The charge was collected by DOSE1 electrometer. Each measured signal was taken from an average of five readings at a given voltage to correct for an output variation. The reproducibility of measurement expressed as the standard deviation of the measured signal at a given depth.

Because a large perturbation effect was observed at the interface between the phantom surface and air, the measurements with both positive and negative voltage (+300V and -300V) were performed in order to take into account this effect [82]. The average reading (M_{ave}) of the measured ionization at each depth was calculated with the following formula:

$$M_{ave} = \frac{M_+ + M_-}{2} \tag{6}$$

where M_+ and M_- are the collected positive and negative charges, respectively. The measured doses in term of percentage were compared with the MC simulation.

3.2.2.3 Measurement of the PDDs using TLD chips

For obtaining the PDDs, TLD chips were carefully placed on the 30×30×20 cm^3 solid water phantom slabs and irradiated at the depth of 0, 0.2, 0.3, 0.5, 1, 1.2, 1.5, 2 and 3 cm in the square field sizes of 5×5, 10×10, 15×15 and 20×20 cm^2. Three repeated measurements were made to obtain the dose at

each position. The reproducibility of reading expressed as the standard deviation on a measured dose at a given depth. The reading in nC unit was converted to the absorbed dose in Gy unit by charge to dose conversion factor.

Before irradiation, all TLD chips were annealed in an annealing oven for restoring its basic condition 400°C for 1 h followed by 100°C for 2 h. After irradiation, the TLD chips were annealed to eliminate unstable low temperature glow curve at 100°C for 10 minutes. Because each TLD could be different in the radiation sensitivity, therefore the calibration factor for sensitivity of TLD must be determined. The TLDs was calibrated by exposure to a known dose at the depth of dose maximum in solid water phantom. The calibration is divided in many techniques depending on the form of dosimeter and the accuracy required. Subsequent action depends on the calibration method chosen.

The procedure of determination used in this study is as follow:

1. All TLDs were put in the holds of a Perspex sheet and covered with a 0.5 cm thickness of the thin Perspex sheet. They were handles with vacuum tweezers using a plastic nozzle to avoid scratching the surface of the chips. Then, they were exposed to a known dose of 1 Gy to avoid the problems with the supra-linearity of LiF at the depth of maximum dose from a 15×15 cm^2 field of a Cobalt-60 machine (THERATONIC 780C).

2. Before each reading of TL signal, the light source and dark current were checked five times. The light yields from TLD reader were signal from the exposed TLD plus background signal which arisen from dark current of PMT, and non-radiation condition. Then, the signal of each TLD responses were read and recorded by the TL reader.

3. The process in step 1 and 2 were repeated twice to produce a reliable calibration factor. The average reading for each TLD was obtained and recorded in ascending number ij (R_{ij}).

4. The calibration factor, C_{ij}, for each individual chip and the absorbed dose, D, is given by:

$$C_{ij} = \frac{R_{ij}}{dose(Gy)} \qquad (7)$$

$$D = \frac{R_{ij} - Background}{C_{ij}} \qquad (8)$$

where R_{ij} is the reading of the ij chip, i is the column and j is the row. The calibration factors for sensitivity of the TLDs used in this study are shown in the Appendix D. The reading was converted to the absorbed dose and then compared with the calculated dose from the MC method.

3.2.3   Determination of the simulated and measured surface dose

For determination of the dose at the surface and in the buildup region, the depth doses along the beam central axis, obtained from the MC simulation and measurement were normalized as a percentage of the maximum dose. The studies were performed at the square and rectangular field sizes. The MC simulations were calculated at the square field sizes ranging from 3 to 25 cm, and at the rectangular field sizes ranging from 5×20 cm^2 to 20×5 cm^2. The first set of data was taken with the square open field sizes of 3×3, 5×5, 10×10, 12×12, 15×15, 20×20 and 25×25 cm^2. The second set of data (FIX-X) was taken with the X collimator jaws fixed for the field's side of 20 cm and varying Y collimator to 5, 8, 10, 12, 15, 18 and 20 cm. The data with the Y collimator jaws fixed (FIX-Y) while the X jaws were varied in the same manner was the third set of our data. As a result, the opening field size ranges from 20×5 to 20×20 cm^2 for the second data set and from 5×20 to 20×20 cm^2 for the third data set.

The Markus chamber was measured at the same field sizes with the MC simulation. For measurement, the CC13 chamber, PFD^{3G} dosimeter and TLD chip were only performed at the square field sizes of 5 to 20 cm. The readings from each detector were assigned to the effective point of the measurement for each individual detector. Here, the percentage dose near or at the phantom surface was estimated by

the third-order polynomial extrapolation of the data. The measured surface doses from different dosimeters were compared with the calculated dose from the MC method in the same condition.

For the Markus chamber, the charge obtained in the build-up region was mainly contributed from electrons scattered from the sidewalls of chamber and collected in the chamber active volume, represented in Nilsson et al [26]. To obtain an accurate surface dose value, the ionization reading has to be corrected by taken into account the perturbation conditions. Here we refer to the correction method introduced by Gerbi and Khan et al [28]. as the GK method to obtain the corrected reading for our Markus parallel plate chamber. By comparing the readings of the various detectors with the reading of an extrapolation chamber, the correction equation was given by Eqs. (9) and (10):

$$P^{'}(d) = P(d) - \xi(E,0)l \exp\left(-\alpha\left(\frac{d}{d_{\max}}\right)\right) \qquad (9)$$

$$\xi(E,0) = 27.19 - 32.59 IR + (-1.666 + 1.982 IR)C \qquad (10)$$

where *P′(d)* and *P(d)* are the corrected and uncorrected percentage depth dose at depth '*d*', respectively, *d* and $d_{\max}$ are the depths, *E* is the maximum energy of the photon spectrum, l is the plate separation in the units of mm, *ξ(E,0)* is the over-response in percent per mm of chamber plate separation at the phantom surface for energy *E*, *IR* is the ionization ratio measured at 10 and 20 cm depths for the field size of 10×10 cm^2 at 100 cm SSD, *C* is the collector edge to side wall distance in mm (it is 0.35 in our case) and α is an empirically determined constant of proportionality which is equal to 5.5. The following constants were determined for our PDD measurement from the 6 MV photon beam: *IR* = 0.6709, *ξ(E,0)* = 5.26% per mm, and $d_{\max}$ = 1.5 cm.

3.2.3.1 Correction factor for the measured surface dose

The percentage doses at the zero depth and the depth of few millimeters from the surface for the 6 MV photon beam with different field sizes were derived from the extrapolation of the measured dose in the build-up region. The correlation of the dose to these dosimeters to the dose from MC simulation at these regions was created to provide the accurately measured dose at the surface and to evaluate the possible treatment complication including the treatment plan for the patients.

From the previous studies, the measured surface dose clearly increases with increasing field size, regardless of the detector used in the measurement. In order to scale down the over-response of the measured surface dose, the correction factors for each dosimeter used in this study were evaluated by calculating the ratio of the MC simulated surface dose and the measured value. To verify the accuracy of the correction factors, the measured surface doses derived from the Markus chamber in the square and rectangular open field sizes were compared with the calculated surface dose from the GK method and the full MC simulation.

3.2.3.2 Equation for estimating the surface dose of rectangular field

Based on the MC simulated results at the square field sizes, the equation for calculating the dose at the surface and relevant depths of rectangular sizes was introduced. In this study, the rectangular fields were converted to the equivalent square fields. The side of the equivalent square for each rectangular field, L_{eq}, was computed using the area-to-perimeter relationship, Equation (4). The surface dose of the equivalent square was then obtained using the equation from the correlation between the side of square field and the surface dose. To ensure the accuracy of this equation, the calculated surface doses from the full MC simulation were compared with the calculated values from the equation. The result of this comparison was shown in terms of the different values.

CHAPTER IV

RESULTS AND DISCUSSION

4.1   Matching the PDDs and beam profiles

After receiving an accurate modeling of the accelerator head geometry, obtaining optimal parameters for the incident electron beam are important to acquire the accurate MC simulated results. Because the extremely high intensity of therapeutic photon beams makes direct measurement of energy spectra virtually impossible, and there are no data available in the literature for angular distributions, the matching method between the MC calculated and measured dose distributions for a given beam energy were employed to generate the starting incident electron energy and radial spread function.

Because the influence of energy spread on both depth dose curves and beam profiles was less, the monoenergetic incident electron energy was used for MC simulation. However the PDD matching can be only used to define the suitable incident electron energy, the beam profile matching has the advantage to define the angular spread of the beam. In this study, the matching condition on the PDDs is started from the depth beyond 1.5 cm to 30 cm, because of the discrepancy due to electron contamination within the buildup region. For the lateral beam profiles, the matching ranges at the depths of 10 cm for the field size of 10×10 cm^2 and 30×30 cm^2 were from -14 to +14 cm and from -29 to +29 cm, respectively.

All measured PDDs and lateral beam profiles were derived from a CC13 and PFD^{3G} dosimeter, respectively. Each measured and simulated depth dose curve was normalized at the depth of maximum dose at the beam central axis. All profile data were normalized to 100% at the same manner. The percentage differences between calculated and measured dose at each point were calculated. The depth dose curve and beam profile comparison for the measurement and the simulation for a field size of 10×10 cm^2 and 30×30 cm^2 are plotted as an example in Figure 4.1 and 4.2, respectively.
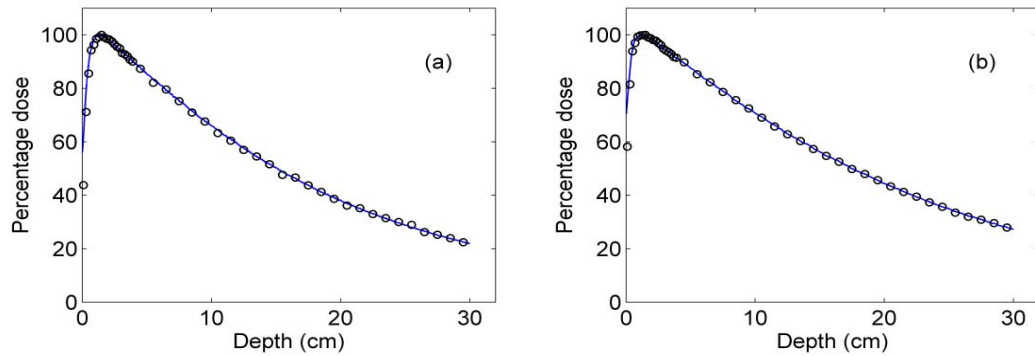
Figure 4.1. The percentage depth dose of (a) 10x10 cm^2 and (b) 30x30 cm^2 fields in water phantom from the 6 MV photon beam. Solid line and open circle represent the measured and simulated data, respectively.
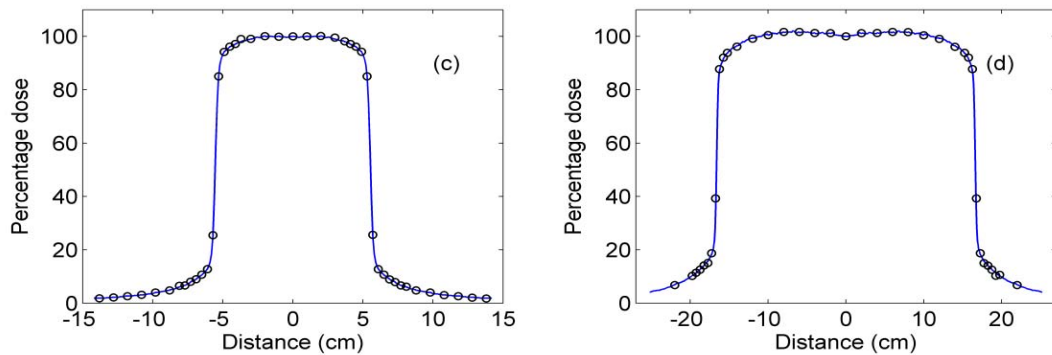
Figure 4.2. The dose profile at 10 cm depth of (c) 10x10 cm^2 and (d) 30x30 cm^2 fields in water phantom from the 6 MV photon beam. Solid line and open circle represent the measured and simulated data, respectively.

All dose differences and distance to agreement analysis between the simulated and measured data are mostly within 1% and 2 mm, respectively. Although the discrepancy between the simulations and measurements were small, the simulated results in systematically lower cross-field profiles than measurements. The comparisons gave the optimal value for starting incident electron energy of 6.1 MeV and for radius spread of 1.2 mm.

4.2   Comparison of the PDDs from the simulated and measured data

Measurements were done using the CC13 chamber, PFD^{3G} dosimeter, Markus chamber and TLD chip for the square field. MC simulations were also run at the same depth and field size with the measurement. The results from the MC calculation and measurement were normalized to the depth of 1.5 cm. The depth dose curve along the central axis plotted for the CC13 chamber, PFD^{3G} dosimeter, Markus chamber and TLD chips compared to the MC simulation of a 10×10 cm^2 field was shown as an example in Figure 4.3.

For the field sizes ranging from 5×5 to 20×20 cm^2, we found excellent agreement between all measured and simulated percentage depth doses for the depth beyond the build-up region or the depth after the maximum dose, because of the establishment of charge particle equilibrium. As we can see, the percentage depth doses obtained from these dosimeters were in good agreement with from MC simulation at the depth greater than 0.5 cm. This suggests that reliable measurement of the percentage depth dose beyond the build-up region can be obtained from any of our four detectors.
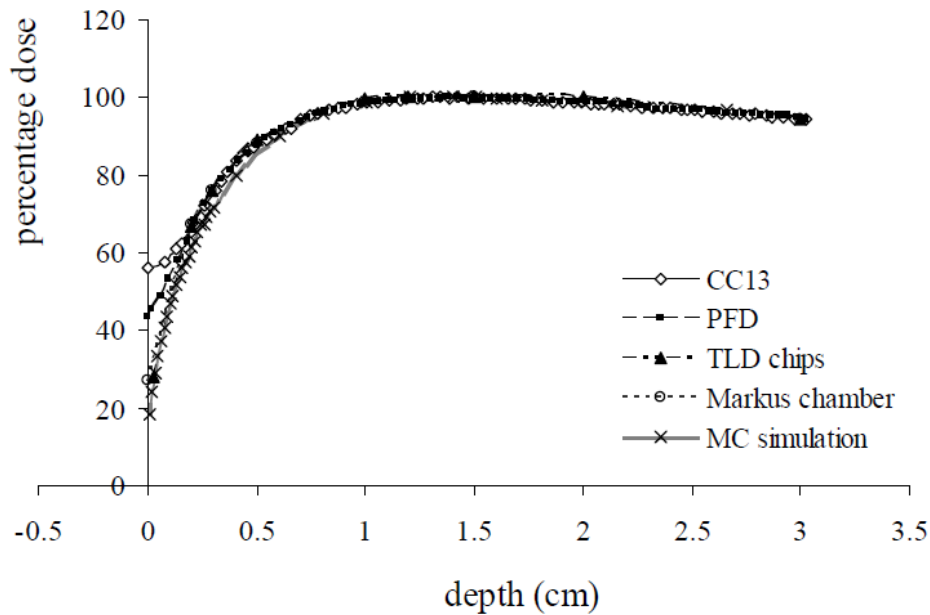
Figure 4.3. The percentage depth dose curves obtained using the CC13 chamber, PFD^{3G} dosimeter, Markus chamber, TLD chips and the MC simulation, for the 6 MV photon beam with a 10×10 cm^2 field.

However, a large deviation from the MC simulated results were noticed between the measurement using the CC13 chamber and the PFD^{3G} dosimeter, the irradiated geometry of the CC13 and PFD^{3G} dosimeter had some parts inside and outside the phantom surface, and was beneath the front of detector surface, respectively. While the results from the TLD and the Markus chamber seem to be in good agreement near the surface region, the irradiated geometry of Markus chamber and TLD chips were placed inside the solid phantom and in the same plane with the phantom surface. Both the curves from the CC13 and PFD^{3G} dosimeter exhibit a bending near the surface while TLD chips and Markus chamber gave smooth trends as similar as the MC simulated curve. From the results, the measured dose in the buildup region seem to depend on the effective point of measurement, the shape and composition of detector and the irradiated geometry as consistent with the reported by Devic et al [67].

Focusing on the buildup region, we examined the PDDs obtained from the four detectors as well as from the MC simulation for a 6 MV photon beam with the four different square field sizes. The percentage of dose in the buildup region for the square open field sizes ranging from 5×5 to 20×20 cm^2 derived from the MC simulation and the measurement using four common dosimeters are presented in Table 4.1 to 4.5.

Table 4.1. The percentage depth dose of the square field sizes between 5×5 to 20×20 cm^2 derived from the MC simulation at the depth of 0.007 to 0.301 cm for the 6 MV photon beam.

Depth (cm)	Field sizes (cm^2)			
	5×5	10×10	15×15	20×20
0.007	13.60	18.47	23.61	30.12
0.021	19.81	24.11	30.18	34.56
0.035	24.30	29.26	34.20	39.31
0.049	28.25	33.48	37.35	43.28
0.063	31.99	37.38	41.64	46.06
0.077	34.98	40.49	45.63	47.38
0.091	38.51	43.31	48.60	50.06
0.105	42.31	46.79	50.49	53.64
0.119	43.87	48.72	53.59	57.30
0.133	46.17	51.89	56.05	61.22
0.147	49.44	53.94	57.65	60.66
0.161	50.35	56.29	61.20	63.84
0.175	53.76	57.42	62.10	65.67
0.189	55.52	58.80	63.38	66.15
0.203	57.24	61.45	66.43	69.71
0.217	58.88	62.81	68.43	70.62
0.231	61.89	65.41	68.86	72.18
0.245	63.19	67.20	71.43	73.36
0.259	66.08	67.29	72.74	74.26
0.273	65.87	69.26	74.20	75.68
0.287	65.96	70.84	75.04	78.43
0.301	68.84	71.81	75.67	78.83

Table 4.2. The percentage depth dose of the square field sizes between 5×5 to 20×20 cm^2 derived from the measurement using CC13 dosimeter at the depth of 0.010 to 0.300 cm in Blue water phantom for the 6 MV photon beam.

Depth (cm)	Field sizes (cm^2)			
	5×5	10×10	15×15	20×20
0.010	50.70	56.16	60.68	64.65
0.020	51.70	56.91	61.67	65.35
0.040	52.69	57.65	62.79	66.58
0.060	53.86	59.55	63.90	67.80
0.080	55.98	61.53	65.76	69.52
0.100	58.02	63.43	67.54	71.17
0.120	59.99	65.27	69.26	72.74
0.140	61.89	67.03	70.90	74.25
0.160	63.73	68.72	72.48	75.70
0.180	65.49	70.34	73.99	77.08
0.200	67.19	71.91	75.43	78.40
0.220	68.83	73.40	76.82	79.67
0.240	70.40	74.84	78.14	80.88
0.260	71.92	76.22	79.41	82.03
0.280	73.38	77.54	80.62	83.13
0.300	74.78	78.80	81.78	84.18

Table 4.3. The percentage depth dose of the square open field sizes between 5×5 to 20×20 cm^2 derived from the measurement using Markus chamber at the depth of 0.003 to 1.000 cm in solid water phantom for the 6 MV photon beam.

Depth (cm)	Field sizes (cm^2)			
	5×5	10×10	15×15	20×20
0.003	20.99	27.01	32.88	38.38
0.200	63.24	67.05	70.88	74.36
0.300	72.62	75.78	78.98	81.80
0.500	85.92	88.00	90.19	92.02
1.000	98.37	98.89	99.45	99.94

Table 4.4. The percentage depth dose of the square open field sizes between 5×5 to 20×20 cm² derived from the measurement using PFD³ᴳ dosimeter at the depth of 0.006 to 0.300 cm in Blue water phantom for the 6 MV photon beam.

Depth (cm)	Field sizes (cm²)			
	5×5	10×10	15×15	20×20
0.006	40.30	43.60	47.90	52.00
0.020	42.20	45.40	49.40	53.10
0.060	46.10	48.80	52.30	55.40
0.100	50.80	53.10	56.20	58.60
0.140	56.00	57.90	60.70	62.50
0.180	61.40	63.00	65.60	66.80
0.220	66.50	68.00	70.40	71.30
0.260	70.80	72.40	74.80	75.60
0.300	74.30	76.00	78.40	79.30

Table 4.5. The percentage depth dose of the square open field sizes between 5×5 to 20×20 cm² derived from the measurement using TLD chips at the depth of 0.025 to 1.000 cm in solid water phantom for the 6 MV photon beam.

Depth (cm)	Field sizes (cm²)			
	5×5	10×10	15×15	20×20
0.025	22.76	28.21	33.04	39.34
0.200	62.66	66.80	71.08	75.06
0.300	71.43	76.16	79.93	83.69
0.500	85.17	89.04	92.04	95.05
1.000	97.46	99.75	100.33	100.45

The data set of the MC simulation, the CC13 chamber and the PFD³ᴳ dosimeter were obtained at the depth of 0.3 cm to the zero depth, while the data set of the Markus chamber and the TLD chip were performed at the depth of 1 cm to the

zero depth. The trend lines for each data set were obtained from the least square fitting using a polynomial function of an appropriate order.
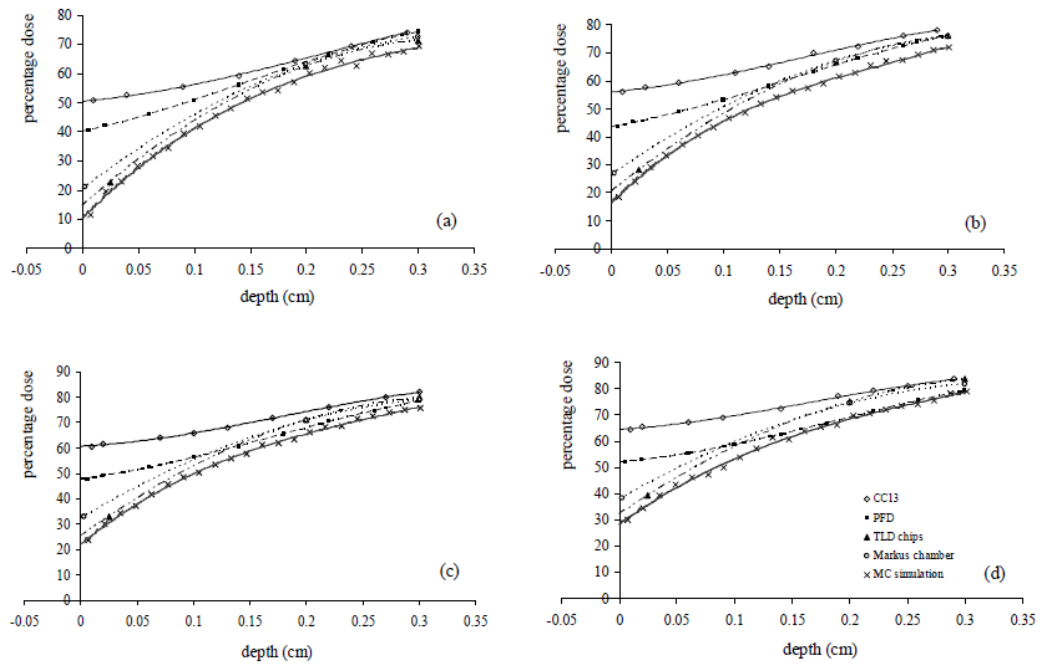
Figure 4.4. The percentage depth dose for the four different square field sizes of (a) 5×5, (b) 10×10, (c) 15×15 and (d) 20×20 cm^2, obtained from the four different dosimeters, plus the MC simulation data, normalized to the maximum depth dose and the best trend line for each data set.

As displayed in Figure 4.4, a similar change was observed in the near-surface region between the measured data from both the Markus chamber and the TLD chip with the MC simulated data, in which these curves have a negative curvature. In contrast, the CC13 and PFD^{3G} data show a positive curvature. Interestingly, the dose readings from both the CC13 chamber and PFD^{3G} dosimeter are almost steady near the surface, varying less than 5% for the CC13 chamber and 10% for the PFD^{3G} at within 1 mm from the surface for the 5×5 up to 20×20 cm^2 field sizes. This implied

that these two detectors are insensitive for the dose measurement at the depth near the surface region. From the results, the maximum deviation of the dose at the 1 mm depth in the phantom derived from the MC simulation and the CC13 chamber was 17%, decreasing to below 10% further than 2 mm. For the PFD^{3G} dosimeter, the deviations at the 1 mm depth derived from the MC simulation and the PFD^{3G} dosimeter at the square field sizes of 5 to 20 cm were less than 10%. Although the high deviations between the MC simulation and the measurement derived from both of detectors in the buildup region were observed, the CC13 chamber and PFD^{3G} dosimeter were typically used to collect the beam data commissioning for computerized treatment planning system in which a very precise position of the measurement at this region may not be necessary.

4.3   The percentage of surface dose

4.3.1   MC simulations

When the MC calculated dose distributions in the standard field sizes were in good agreement with measured dose distributions, the accelerator head geometry, the incident electron energy, the radius distributions and the transport parameters derived from the previous part of this study was used to determine the dose at shallow depths from difference field sizes in order to predict the skin complication. Using the simulation, the percentage depth dose near or at the phantom surface, estimated by the third-order polynomial extrapolation of the simulated data was obtained. The overall MC modeling error is within the requirement of 1%. Table 4.6 and 4.7 summarized the dose at the depth at 0 cm and the depth of 0.007 cm using the MC simulation method for the various fields. Based on the percentage depth dose in the buildup region, the percentage dose at depth of 0 and 0.007 cm, called surface and skin dose, respectively, were obtained from the third-order polynomial fitting

Table 4.6. The percentage surface dose for the 6 MV photon beams with a square and rectangular field sizes obtained from our MC simulation.

	L_x (cm)	L_y (cm)	MC simulation
Square	3	3	9.71
	5	5	10.27
	10	10	16.45
	12	12	20.03
	15	15	22.22
	20	20	28.41
	25	25	30.97
Rectangular	5	15	14.32
	15	5	14.48
	5	20	15.56
	20	5	15.53
	7	18	17.53
	18	7	17.95
	8	20	18.67
	20	8	19.49
	10	20	20.63
	20	10	20.08
	12	17	22.35
	17	12	21.51
	12	20	22.56
	20	12	22.28
	15	20	24.47
	20	15	23.68
	18	20	25.63
	20	18	25.36

Table 4.7. The percentage of dose at the 0.007 cm depth for the 6
MV photon beams with a square and rectangular field
sizes obtained from our MC simulation.

	L_x (cm)	L_y (cm)	MC simulation
Square	3	3	11.79
	5	5	13.60
	10	10	18.47
	12	12	21.76
	15	15	23.61
	20	20	30.12
	25	25	32.70
Rectangular	5	15	16.64
	15	5	16.57
	5	20	17.20
	20	5	17.81
	7	18	19.05
	18	7	19.70
	8	20	20.49
	20	8	20.86
	10	20	22.41
	20	10	22.09
	12	17	24.14
	17	12	22.91
	12	20	24.16
	20	12	24.40
	15	20	25.87
	20	15	25.72
	18	20	28.37
	20	18	27.51

Because of the influence of electron contaminations at the surface region, the ECUT and AE values were set to lower than 700 MeV in order to collect all secondary charged particles. In this study, the ECUT and AE value was set to 521 MeV for determining the surface dose, as consistent with the recommended parameters from the study of Kim et al [68]. Moreover the voxel size for calculating the dose at buildup region was defined with the thinner dimension in the z plane to represent the dose within the specific depth, because the deposited doses from MC simulation were integrated over the total thickness. In this study, the voxel size in the z direction was set to 0.014 cm. To receive the simulated uncertainty within 1%, the voxel size was set to 3×3 cm^2 in the x and y direction.

According to the comprehensive published data, the surface doses from our MC simulation were correlated with the theoretical surface dose. When compared our MC simulated result with the published data, the deviation of dose at the zero depth was less than 1.5% for a 10×10 cm^2 field at the 6 MV photon beam. Moreover, the deviations for the field sizes of 5, 10 and 15 were 1.63% 1.25%and 1.04%, respectively, when compared with the study of Gerbi and Khan [28].

Because it is well known that the thickness of skin layer varies throughout the position of human body, the relevant depths for determination of skin dose should be defined. To verify the accuracy of the dose determination near or at the surface using the MC simulation, the observed percentage doses at the surface and at the depth of 0.0007 and 0.005 mm were compared with the published results of Parsai et al [37] and Devic et al [67], since they had performed the reliable measurements using the extrapolation chamber of the same beam energy from the similar medical linear accelerators (the Varian Clinac 1800 and the Varian 2300 C/D). Moreover, we don't have the extrapolation chamber in our department. Table 4.8 presents the dose comparison using the MC simulation results obtained here and the previously measured values for the square fields with lengths of 5, 10, 15 and 25 cm. The difference column values indicate the percentage error between the MC simulation and the extrapolation chamber derived from the previous studies for each field size.

Table 4.8. Comparison of the percentage doses at the surface, and at a depth of 0.007 and 0.05 cm for the 6 MV photon beams obtained from our MC simulation and from previously reported empirical measurements.

Depth (cm)	Field size (cm^2)	Measured value [31,63]	Our MC simulation	Difference (%)
0	5×5	10.53	10.27	-0.26
	10×10	16.04	16.45	+0.41
	15×15	21.74	22.22	-0.48
	25×25	31.45	30.97	-0.48
0.007	5×5	11.50	11.61	+0.11
	10×10	17.00	18.30	+1.30
	15×15	23.60	23.61	+0.01
	25×25	33.50	32.70	-0.80
0.05	5×5	28.32	28.12	-0.20
	10×10	33.34	33.48	+0.14
	15×15	38.02	37.35	-0.67
	25×25	46.64	45.10	-1.54

The surface dose clearly increases with increasing field size as consistent with the previous studies [11, 18-20]. A substantial discrepancy in the dose at the build-up region from our MC simulation based calculations and their previously reported empirical measurements were not anticipated. Consistent results were generally observed in which all of the differences were less than 2%. Therefore, we conclude that our calculated surface doses using the MC simulation were justified. Observing in the percentage of surface dose, the differences between our MC simulation and the previous data from the similar linear accelerator were closed agreement. This implied that the percentage of dose at surface and relevant depths did not depend on the

linac's model of the same manufacturer, but it seems to depend on the different configuration of linac's head of the different manufacturer. According the study of Paelinck et al [83], the buildup dose between Varian and Elekta linear accelerators for high energy photon beam were compared. In regular square fields, the Varian linear accelerator have higher dose in the buildup region than the Elekta machine, both for the 6 MV and 18 MV photon beam, because of the higher amount of contaminant electrons.

4.3.2   Measurements

The percentage depth doses along the beam central axis for our 6 MV photon beam were experimentally acquired for all studied field sizes with four detectors: the CC13 chamber, PFD^{3G} dosimeter, Markus chamber and TLD chip. To validate the calculated dose derived from the treatment planning system, the percentage of dose near or at the surface were done by the CC13 and PFD^{3G} dosimeter since they are commonly used to collect the beam data. In this study, the percentage of dose at the surface and relevant depths collected from these dosimeters was only performed in the square field sizes ranging from 5 to 20 cm.

Because of the suitable properties and be useful in clinical situation, the TLDs are the appropriated choice of detector for measuring the surface dose. Before using, the TLDs were calibrated with the known dose and determined an individual calibration factor for each chip. The reproducibility of measured dose at the given depth using the TLDs expressed as the standard deviation was within 3%. In this study, the TLDs were placed at the central axis of beam in the same plane with the phantom surface to measure the percentage of dose at the 5×5 cm^2 to 20×20 cm^2 field sizes.

The parallel plate chambers are often used to measure the dose at the surface and the interfaces region. For the photon beam dosimetry, the chamber polarity effect on the total charge collected using parallel plate chamber has been known for many years. As the study of Gerbi and Khan [82], when the photon beam interacted with the collecting electrode of the chamber, the secondary electrons were generated and

ejected in the forward direction. A region of positive charge was established at the interacted site. After applying a negative bias, a greater positive charge is collected on the electrode. For a positive bias on the collecting electrode, the revered effect was observed. The positive charge was compensated by the negative electrons stopped in the collector as the depth of measurement approaches the range of secondary electrons. Therefore the large polarity effect was observed at the surface region and decreased with increasing the depth below the phantom surface.

To include the polarity effect in this study, the charged obtained from Markus chamber in the buildup region was corrected by measurement with both positive and negative voltage and calculation of the average value. For measuring the percentage of dose at the buildup region, the Markus chamber was placed at the central axis of beam in the same plane with the phantom surface for both of square and rectangular field size, because it was available for measurement and the consistency of measurement using Markus chamber was within 1%. In this study, the collected charges were found to nearly independent with the applied voltage at the depth deeper than 3 mm as consistent with the study of Velkley et al [29].

Table 4.9. The percentage surface doses for the 6 MV photon beam with a square field sizes, obtained from measurement using the CC13 chamber, PFD^{3G} dosimeter, Markus chamber and TLD chips.

Field size	Percentage surface dose			
(cm^2)	CC13	PFD^{3G}	Markus	TLD chip
5×5	50.59	40.12	20.46	14.59
10×10	55.99	43.52	26.31	20.46
15×15	60.73	47.87	32.21	25.34
20×20	64.54	52.01	37.75	32.17

Table 4.10. The percentage surface doses for the 6 MV photon beam with a square and rectangular field sizes, obtained from measurement using the Markus chamber.

	L_x (cm)	L_y (cm)	Percentage surface dose
Square	3	3	18.62
	12	12	29.38
	25	25	43.28
Rectangular	5	15	24.29
	15	5	24.34
	7	18	27.39
	18	7	27.33
	12	17	31.60
	17	12	31.56

From the extrapolation of the measured dose in the build-up region, the percentage doses at zero depth (surface dose) for the 6 MV photon beam with square and rectangular field sizes are shown in Table 4.9 and 4.10, respectively. The measured surface dose clearly increases with increasing field size, regardless of the detector used in the measurement. This is mainly due to the increasing number of contaminated electrons.

4.3.3 Comparison of the percentage surface dose from the simulated and measured data

The relation between the percentage surface dose and length of square field size was established for determination the influence of the field size to the surface dose, as shown in Figure 4.5. The measured surface dose is larger than that of the simulation which is consistent with previous reports [11, 18-20]. The surface dose

from the TLD measurement had the best agreement with the MC simulation. The worst and second worst agreement with the MC simulated data was exhibited by the CC13 and PFD^{3G} detectors, respectively.

Figure 4.5. The percentage surface dose obtained from the four different dosimeters and the MC simulation, normalized to the maximum depth dose at a 100 cm SSD for the 6 MV photon beam.

The high percentage surface doses observed with the CC13 and PFD^{3G} dosimeters with the field size of 10×10 cm^2 was about 55% and 43%, respectively. As represented in Table 4.11, the over responses at the zero depth were more than 38% and 25%, respectively. Possibly, these two detectors pick up many low-energy electrons from the non-electronic equilibrium situation in the build-up region. Moreover, at some point of the measurement, and especially close to the phantom surface, some part of these detectors was above the water level, which is also a cause of the non-equilibrium. Note that the percentage dose near the surface obtained with both PFD^{3G} and CC13 chamber did not change rapidly with the increasing depth see Figure 4.4, but remained approximately steady near the surface phantom for all field

sizes. In other words, these detectors eliminate the high gradient feature of the dose in the build-up region of the photon beam. As a result, their position for measuring the surface dose is not very critical. Because of this, both the PFD^{3G} dosimeter and CC13 chamber may be recommended for surface dose measurements if their accurate correction factors are available. Moreover the results derived from these dosimeters could be used as PDD data in the buildup region for a TPS to achieve the accurate dose calculation to skin.

Table 4.11. The over-response at the surface of the CC13 chamber, PFD^{3G} dosimeter, Markus chamber and TLD chip based on MC simulation for the 6 MV photon beam.

Field size (cm^2)	Over response			
	CC13	PFD^{3G}	Markus	TLD chip
5×5	40.32	28.67	9.01	3.14
10×10	39.54	27.07	9.86	4.01
15×15	38.51	25.65	9.99	3.12
20×20	36.13	23.60	9.34	3.76

According the study of Nilsson and Montelius [26], the perturbation effect will increase the ionization in the chamber when measured the surface dose with the fixed parallel plate chamber. A small diameter chamber will have a larger contribution from the electrons emitted from the side wall in forward directions at small angles. Therefore the parallel plate chamber used to measure the dose at surface should have a large angle between the side wall and the central axis. From the study of Velkley et al [29], they also found that the parallel plate chamber overestimated the percentage of dose by 10-40% depended on the photon energy.

In this study, the Markus chamber used to measure the surface dose has a small distance between the side wall and the central axis, the large perturbation effect

was observed. Comparison with the MC simulated results, the over-response of the Markus chamber for the surface dose before scaling of the effective depth of measurement was about 10%, which is consistent with the reports of Gerbi and Khan [28] and Devic et al [67]. After taking into account the effective point of measurement, the over-response from the Markus chamber remained almost unchanged due to its larger effective volume.

The TLDs with the thickness of 0.38 mm overestimated the dose at the phantom surface due to the integrated dose over the total thickness of chip. Comparison with the MC simulation, the over-response of the TLD chip for the surface dose before scaling of the effective depth of measurement were about 10%, which is consistent with the reports of Gerbi and Khan [28] and Devic et al [67]. After taking into account the effective point of measurement, the over-response from the TLD chip was reduced to approximately 4%. Since the effect of photon spectral variations on the response was less than 1% for all of our dose measurements, the variation of the TLD response with respect to the changes in either the field size or the measurement location was not included in this study [84].

4.4   Correction factor for the measured surface dose

In order to scale down the over-response of the measured surface dose, the correction factors for each dosimeter used in this study were evaluated by calculating the ratio of the MC simulated surface dose and the measured value, as shown in Table 4.12. Noting that a smaller correction factor implies a larger over-response of the detector for the surface dose measurement, the over dose response order (highest to lowest) was found to be the CC13 chamber > PFD^{3G} dosimeter > Markus chamber > TLD chip. The correction factor for dosimeter nearly close to 1 represents that the measured dose at the surface for that dosimeter agrees with the MC simulated data and is required the correction factor.

Table 4.12. The correction factor of the surface dose for the CC13 chamber, PFD^{3G} dosimeter, Markus chamber and TLD chip based on MC simulation for the 6 MV photon beam.

Field size	Correction factor			
(cm^2)	CC13	PFD^{3G}	Markus	TLD chip
5×5	0.2030	0.2560	0.5020	0.7040
10×10	0.2938	0.3780	0.6252	0.8041
15×15	0.3659	0.4641	0.6899	0.8770
20×20	0.4401	0.5462	0.7526	0.8831
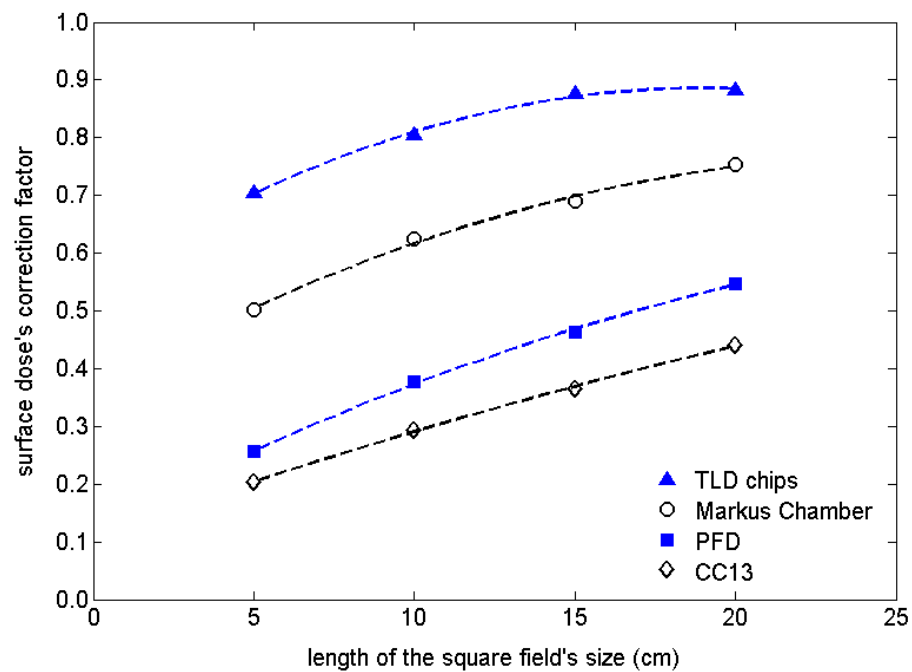
Figure 4.6. The correction factor for surface dose as a function of the length of square field's side for the four different dosimeters based on the MC simulation.

The relationship between the corrected factors, based on the data from the MC simulation as the reference value, for the four detectors at various open square field sizes were shown in Figure 4.6. Since the TLD chip gave the nearest surface dose to MC simulations, the correction factors for the TLD chip were the largest of the four different types of detectors. To evaluate the skin complication and design the treatment technique, the correlation between the measured dose and the MC simulated dose at the relevant depths should be provided. In this study, the correlation of the dose at depth of 0.007 cm derived from the MC simulation to the measured dose obtained from four dosimeter types was introduced, as shown in Table 4.13.

Table 4.13. The correction factor of the dose at depth of 0.007 cm for the CC13 chamber, PFD^{3G} dosimeter, Markus chamber and TLD chip based on MC simulation for the 6 MV photon beam.

Field size (cm^2)	Correction factor			
	CC13	PFD^{3G}	Markus	TLD chip
5×5	0.2688	0.3390	0.6648	0.9323
10×10	0.3299	0.4244	0.7020	0.9029
15×15	0.3888	0.4932	0.7330	0.9318
20×20	0.4667	0.5791	0.7980	0.9364

In order to include the effect of the field size dependence in the correction factor at the surface dose and the dose at depth of 0.007 cm, we performed the best least square fitting on the correction factors for the four square field sizes ranging from 5 to 20 cm, assuming a parabolic tendency on the length of the field's side [85].

The correction factor (C_i) for each detector (label by an index i) as a function of the length of square field's side (L) can be written as in Eq (11):

$$C_i(L) = a_i L^2 + b_i L + d_i \qquad (11)$$

where a_i b_i and d_i are the parameters which depend on the type of detector and were shown in Table 4.14 and 4.15. Our empirical correction factor takes into account the area (L^2) and the side of the field (L) with additional offset. They are supposed to be applicable to the surface dose and the dose at depth of 0.007 cm of the square field for a size ranging from 5×5 to 20×20 cm^2.

Table 4.14. Fitting parameters for the correction factor of the surface dose defined in Eq. (11) for the four different types of dosimeters.

Type of dosimeter	Coefficient		
	a	b	d
CC13	-0.0002	0.0198	0.1091
PFD^{3G}	-0.0004	0.0291	0.1220
Markus model 23392	-0.0006	0.0314	0.3628
TLD chip	-0.0009	0.0357	0.5470

Table 4.15. Fitting parameters for the correction factor of the dose at depth of 0.007 cm defined in Eq. (11) for the four different types of dosimeters.

Type of dosimeter	Coefficient		
	a	b	d
CC13	0.0002	0.0088	0.2215
PFD^{3G}	-	0.0158	0.2610
Markus model 23392	0.0003	0.0017	0.6515
TLD chip	0.0003	0.0077	0.9580

The dose at surface and depth of 0.007 cm after the correction is simply obtained by a multiplication of the correction factor C_i with the reading dose from the measurement. The correlation of the dose to each dosimeter at the zero and relevant depths will provide more tools for the physician for evaluating the skin complication and selecting better treatment technique for the patients. Moreover the physicist will be able to measure the accurate dose at the surface region.

4.4.1 Verification of the correction factor for the measured surface dose

To verify the accuracy of correction factor derived from the above equation, the percentage of doses for other square fields (3x3, 12x12, and 25x25 cm^2) and rectangular fields (5×15, 15×5, 7×18, 18×7, 12×17 and 17×12 cm^2) were empirically investigated using the measurements derived from the Markus chamber in a water equivalent solid phantom and, also, by the MC simulation, as presented in Table 4.16 and 4.17, respectively. Only the 3x3 and 25x25 cm^2 fields are extending this range to larger and smaller field sizes.

Table 4.16. The percentage depth dose of the rectangular field sizes derived from the measurement using Markus chamber at the depth of 0.003 to 1.000 cm in solid water phantom for the 6 MV photon beam.

Depth (cm)	Field sizes (cm^2)								
	3×3	12×12	25×25	5×15	15×5	7×18	18×7	12×17	17×12
0.003	18.62	29.38	43.28	24.29	24.34	27.39	27.33	31.60	31.56
0.200	61.84	68.58	77.25	65.96	65.79	67.97	67.70	70.61	70.43
0.300	72.59	76.38	84.90	75.21	75.08	76.95	76.65	79.13	78.92
0.500	85.58	89.10	93.43	87.05	87.03	88.32	88.07	89.64	89.67
1.000	98.52	99.17	100.10	98.51	98.40	98.76	98.67	99.12	99.12

Table 4.17. The percentage depth dose of the rectangular field
sizes derived from the MC simulation at the depth of
0.007 to 0.301 cm in Blue water phantom for the 6
MV photon beam.

Depth (cm)	Field sizes (cm^2)								
	3×3	12×12	25×25	5×15	15×5	7×18	18×7	12×17	17×12
0.007	11.79	21.76	32.70	16.64	16.57	19.05	19.70	24.14	22.91
0.021	16.44	27.29	38.34	22.03	22.41	24.59	25.07	29.63	29.27
0.035	21.13	31.49	42.11	26.37	26.52	30.12	29.59	33.36	33.00
0.049	27.06	35.78	45.10	30.53	31.40	35.01	33.52	37.55	38.26
0.063	28.61	39.80	47.98	34.06	36.03	38.04	36.82	41.34	42.20
0.077	32.07	43.18	51.87	38.63	38.58	39.87	40.02	44.25	44.45
0.091	36.12	46.21	52.67	41.37	41.43	44.27	43.05	47.12	46.33
0.105	37.61	48.66	55.75	44.58	44.88	46.81	45.67	49.33	50.05
0.119	41.05	51.38	58.67	47.03	47.85	49.54	49.64	51.89	51.86
0.133	43.87	52.86	62.48	50.09	50.49	51.80	51.60	54.32	54.49
0.147	47.69	54.56	63.58	51.58	52.60	54.15	52.77	56.11	56.20
0.161	50.14	58.14	66.73	52.37	54.49	56.38	55.67	58.70	59.15
0.175	53.05	60.27	67.93	55.88	55.33	58.62	57.21	60.40	60.63
0.189	53.13	61.99	68.26	57.10	56.91	60.52	58.65	62.80	62.08
0.203	56.09	62.78	68.20	58.57	59.33	62.34	61.53	65.84	64.53
0.217	58.73	66.78	71.74	61.51	62.21	64.28	63.66	65.61	65.85
0.231	59.52	67.70	71.60	64.28	65.15	65.33	65.44	65.99	67.31
0.245	60.70	67.12	72.44	64.62	65.50	65.99	66.60	68.52	68.65
0.259	63.73	69.88	73.53	66.03	67.35	68.87	67.73	69.24	71.17
0.273	65.44	71.88	76.08	67.97	68.79	70.60	70.07	71.26	71.57
0.287	67.37	72.90	77.13	67.84	70.61	71.05	71.18	73.79	71.85
0.301	68.96	72.85	78.06	70.56	70.63	71.03	72.20	73.85	74.92

The percentage surface doses from the actual reading, the Eq. (11) corrected values using the empirical correction factors (Table 4.14), and the MC simulation values are shown in Table 4.18, along with the modified percentage surface doses using the GK method for the Markus chamber.

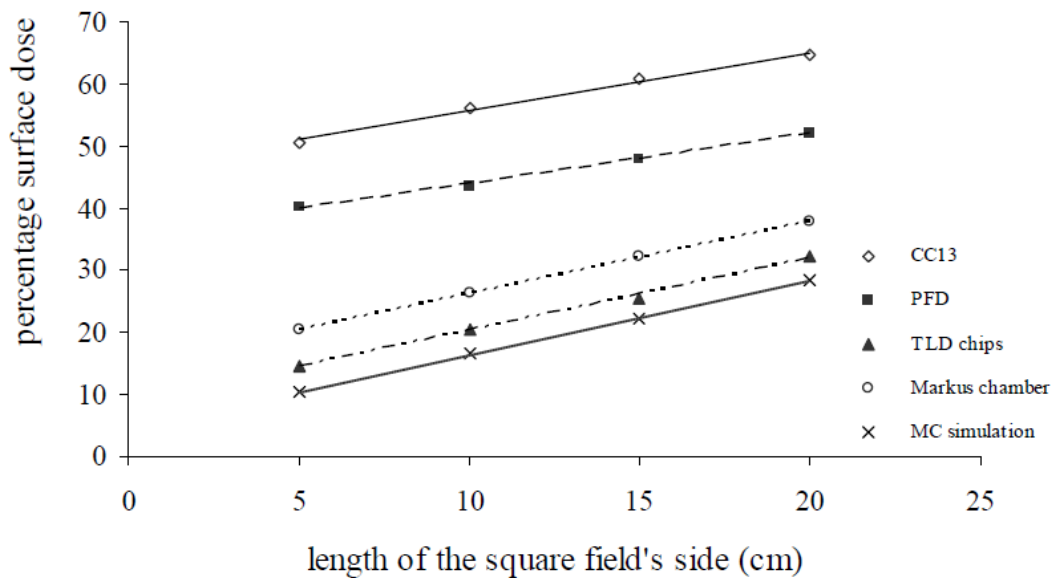**Table 4.18.** The percentage surface doses for the 6 MV photon beam with square and rectangular field sizes, obtained from measurements using the Markus chamber and then corrected using the GK method or empirical correction factor C_i, in comparison with that from MC simulation.

Field size (cm^2)	Percentage surface dose		
	MC simulation	GK method	Empirical method
3×3	9.71	8.21	8.14
5×15	14.32	13.88	13.71
15×5	14.48	13.93	13.74
7×18	17.53	16.98	16.94
18×7	17.95	16.92	16.90
12×12	20.03	18.97	19.19
12×17	22.35	21.19	21.67
17×12	21.51	21.15	21.64
25×25	30.97	32.88	33.45

The corrected surface dose values (using Eq. (11) and Table 4.14) were lower than that of the MC simulation for the field sizes smaller than 25×25 cm^2, and were closer to the MC simulation than the GK corrected values for only the 12×12 cm^2 square size. For both the 3×3 and 25×25 cm^2 field sizes, the GK corrected values were closer to the MC. In other words, the empirical correction of the surface dose presented here is not better than the GK method outside the range of the studied field size (5×5 cm^2 to 20×20 cm^2). The average deviation was about 1.5% in the square field sizes ranging from 3 to 14 cm. The maximum deviation was observed about 2.5% at the field size of 25×25 cm^2. Therefore, these empirical correction factors could be used for the field sizes in the range between 5×5 cm^2 to 20×20 cm^2.

For the depth of 0.007 cm, the measured doses performed by the Markus chamber at the zero depth were corrected with the empirical equation (using Eq. (11) and Table 4.15). The corrected dose values were good agreement with the full MC simulation within 1% exception in the field size of 25×25 cm^2. Therefore, the empirical correction for the dose at depth of 0.007 cm could be used for the field sizes ranging from 3×3 cm^2 to 20×20 cm^2.

Table 4.19. The percentage of doses at the depth of 0.007 cm for the 6 MV photon beam with square and rectangular field sizes, obtained from measurements using the Markus chamber and then corrected using the empirical correction factor C$_i$, in comparison with that from MC simulation.

Field size (cm^2)	Percentage surface dose		Difference (%)
	MC simulation	Empirical method	
3×3	11.79	12.28	-0.49
5×15	16.64	16.54	0.10
15×5	16.57	16.58	-0.01
7×18	19.05	19.15	-0.10
18×7	19.70	19.11	0.59
12×12	21.76	21.01	0.75
12×17	24.14	23.22	0.90
17×12	22.91	23.19	-0.28
25×25	32.70	38.15	-5.45

Because the number of data set was less, we tried to fit the curves of correction factor with the linear regression. When compared with the full MC simulation, the surface doses and the dose at depth of 0.007 cm derived from the

linear regression were lower in all studies field sizes exception in the field size of 25×25 cm^2. The average deviation was less than 2% in the square field sizes ranging from 3 to 14 cm. The maximum deviation was still observed more than 5% at the field size of 25×25 cm^2. Although the deviation derived from this equation was less than the tolerance criteria, as shown in Table 2.1, the surface doses and the doses at depth 0.007 cm derived from the linear regression equation were worst than that from the second order polynomial equation (Eq.(11)). Therefore we prefer to introduce the correction factor derived from the second order polynomial fitting to calculate the accurate surface dose and the dose at depth 0.007 cm.

4.5 MC simulated equation for estimation the surface dose of rectangular field

Because the treatment field of rectangular size is often used in clinical application where the ratio of length to width is 2 or less, knowing the surface dose and the dose in relevant depths in rectangular fields is necessary. As shown in Figure 4.7, the buildup dose of rectangular field also increases with the increasing field size and the collimator exchange effect is not obvious. Normally, the collimator exchange effect influences the head scatter factor (collimator factor) and the absolute dose at depth of maximum dose. Following the previous study [76], the influence of collimator exchange effect on the highly elongated rectangular fields was more pronounced when the upper jaws define the long axis of the rectangular field.
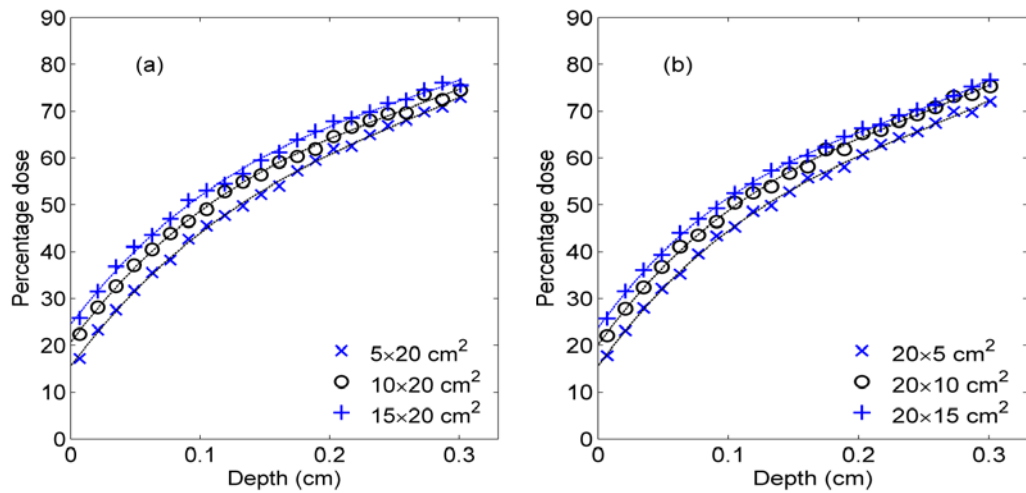
Figure 4.7. The percentage depth dose in the buildup region for some of the rectangular fields considered in this study: (a) represent the data with the Y jaws fixed for the field's side of 20 cm while the X jaws was varied and (b) represent the data with the X jaws fixed for the field's side of 20 cm.

The percentage of dose derived from the MC simulation for the rectangular fields with the Y collimator jaws fixed for the field's side of 20 cm and varying X collimator ranging from 5 to 20 cm, and the X collimator jaws fixed while the Y jaws was varied in the same manner were presented in Table 4.20 and 4.21, respectively.

Table 4.20. The percentage depth dose of the rectangular fields with the Y jaws fixed and varying the X jaws at the depth of 0.007 to 0.301 cm for the 6 MV photon beam.

Depth (cm)	Field sizes (cm^2)					
	5×20	8×20	10×20	12×20	15×20	18×20
0.007	17.20	20.49	22.41	24.16	25.87	28.37
0.021	23.29	27.14	28.12	29.57	31.54	32.92
0.035	27.61	30.97	32.66	33.60	36.83	38.34
0.049	31.74	34.84	37.14	37.87	41.05	41.60
0.063	35.53	38.95	40.49	40.21	43.58	44.16
0.077	38.20	42.04	43.90	44.77	47.02	48.24
0.091	42.68	45.55	46.51	47.62	51.00	51.12
0.105	45.54	47.94	49.06	49.65	53.11	54.45
0.119	47.75	50.02	52.88	52.55	54.46	57.42
0.133	49.77	53.15	54.96	53.45	56.65	59.19
0.147	52.20	55.28	56.44	57.14	59.49	62.41
0.161	54.02	58.12	59.18	58.16	61.23	62.11
0.175	57.27	59.62	60.34	58.46	63.90	64.27
0.189	59.47	61.07	61.90	61.72	65.73	66.08
0.203	61.98	62.61	64.61	65.57	67.79	68.06
0.217	62.52	63.61	66.60	66.41	68.56	68.89
0.231	64.96	66.03	68.05	67.83	69.84	70.99
0.245	66.91	67.15	69.48	69.33	71.66	72.22
0.259	68.09	68.57	69.70	70.96	72.45	73.81
0.273	69.88	68.92	73.60	72.31	74.60	75.78
0.287	70.90	71.17	72.45	73.67	76.04	79.48
0.301	72.91	73.07	74.53	75.00	75.51	78.75

Table 4.21. The percentage depth dose of the rectangular fields with the X jaws fixed and varying the Y jaws at the depth of 0.007 to 0.301 cm for the 6 MV photon beam.

Depth (cm)	Field sizes (cm^2)					
	20×5	20×8	20×10	20×12	20×15	20×18
0.007	17.81	20.86	22.09	24.40	25.72	27.51
0.021	23.14	25.94	27.82	29.12	31.59	32.52
0.035	27.99	30.32	32.39	33.22	36.12	37.50
0.049	32.14	35.04	36.74	37.53	39.33	41.47
0.063	35.24	37.94	41.08	40.71	44.06	44.56
0.077	39.54	41.66	43.55	43.87	47.03	49.40
0.091	43.38	44.09	46.46	48.06	49.34	51.47
0.105	45.30	46.57	50.51	50.48	52.51	52.98
0.119	48.62	49.01	52.59	52.53	54.40	56.52
0.133	49.84	51.10	53.93	53.34	57.38	58.78
0.147	52.83	53.95	56.79	57.20	58.87	59.67
0.161	55.75	55.76	58.20	58.34	60.46	62.64
0.175	56.40	56.82	61.82	60.32	62.37	64.62
0.189	58.05	59.20	61.87	62.33	64.56	66.02
0.203	60.76	62.39	65.25	63.89	66.39	66.47
0.217	62.88	65.02	65.98	66.24	67.09	69.90
0.231	64.36	65.47	67.91	66.97	69.16	71.18
0.245	65.64	66.68	69.27	69.69	70.29	72.47
0.259	67.49	68.91	70.82	72.20	71.35	73.29
0.273	69.98	70.23	73.17	71.33	73.25	73.41
0.287	69.76	71.23	73.62	73.43	75.32	75.91
0.301	72.07	71.24	75.30	74.47	76.65	77.53

From the MC data, the percentage surface dose (D_0) increased from about 10% to 31% for the square's side varying from 3 to 25 cm. While the percentage of dose at depth of 0.007 cm for the square field size of 3 to 25 cm increased from about 12% to 33%.To receive the accurate dose at the surface and the depth of 0.007 cm including in the rectangular sizes, the equivalent square of each rectangular field was determined using the A/P formula, equation (4).

The correlation between the side of the square field and the surface dose based on the MC simulated doses of all square fields was examined by the method of least-

square fitting. Its corresponding of percentage surface dose, D_0 (L_{sq}), and the dose at depth of 0.007 cm, $D_{0.007}$ (L_{sq}), was calculated using equation (12) and (13), respectively.

The equation for calculating the dose at zero depth:

$$D_0\left(L_{sq}\right) = -0.0117 L_{sq}{}^2 + 1.365 L_{sq} + 4.7363 \tag{12}$$

The equation foe calculating the dose at 0.007 cm depth:

$$D_{0.007}\left(L_{sq}\right) = -0.0078 L_{sq}{}^2 + 1.2078 L_{sq} + 7.8906 \tag{13}$$

To verify the accuracy of the empirical equation, the comparison between the calculation using this equation and its MC value was shown in Table 4.22 and 4.23, respectively. The doses at the surface and depth of 0.007 cm derived from the full MC simulation in the rectangular field approached to those from the corresponding equivalent square fields using the A/P relationship. The maximum difference was about 1% for all studied field sizes in both of depths. In this study, the surface doses for rectangular fields were generally higher than their corresponding equivalent square sizes for the elongation ratio of 2.5 or higher. For the rectangular field with an elongation ratio less than 2.5, the surface doses were generally lower than their corresponding equivalent square sizes. While the dose at the depth of 0.007 cm for the rectangular field with an elongation ratio higher than 2.5 were higher than their corresponding equivalent square sizes.

For each rectangular field pattern, the interchange between the X- and Y-collimator resulted in a minor difference (less than 1%) in the percentage of dose, at surface and at depth of 0.007 cm, as shown in the third column in Table 4.22 and 4.23. The collimator exchange did not affect the derived dose at both of depths. Therefore, it may not be practically important and can be excluded in the equivalent square formula for determination of the dose at surface and depth of 0.007 cm.

Table 4.22. The percentage surface dose of rectangular field pattern determined by the MC simulation and compared with that of its equivalent square.

L_x (cm)	L_y (cm)	Surface dose (%)	Side of equivalent square L_{eq} (cm)	Estimated Surface dose (%)	Difference (%)
5	15	14.32	7.50	14.32	0.00
15	5	14.48			0.16
5	20	15.56	8.00	14.91	0.65
20	5	15.53			0.62
7	18	17.53	10.08	17.31	0.22
18	7	17.95			0.64
8	20	18.67	11.43	18.81	-0.14
20	8	19.49			0.68
10	20	20.63	13.33	20.85	-0.22
20	10	20.08			-0.77
12	17	22.35	14.07	21.63	0.72
17	12	21.51			-0.12
12	20	22.56	15.00	22.58	-0.02
20	12	22.28			-0.30
15	20	24.47	17.14	24.70	-0.23
20	15	23.68			-1.02
18	20	25.63	18.95	26.40	-0.77
20	18	25.36			-1.04

Table 4.23. The percentage dose at the depth of 0.007 cm of rectangular field pattern determined by the MC simulation and compared with that of its equivalent square.

L_x (cm)	L_y (cm)	Dose at 0.007 cm depth (%)	Side of equivalent square L_{eq} (cm)	Estimated Surface dose (%)	Difference (%)
5	15	16.64	7.50	16.51	0.13
15	5	16.57			0.06
5	20	17.20	8.00	17.05	0.15
20	5	17.81			0.76
7	18	19.05	10.08	19.27	-0.22
18	7	19.70			0.43
8	20	20.49	11.43	20.68	-0.19
20	8	20.86			0.18
10	20	22.41	13.33	22.60	-0.19
20	10	22.09			-0.51
12	17	24.14	14.07	23.34	0.80
17	12	22.91			-0.43
12	20	24.16	15.00	24.25	-0.09
20	12	24.40			0.15
15	20	25.87	17.14	26.30	-0.43
20	15	25.72			-0.58
18	20	28.37	18.95	27.98	0.39
20	18	27.51			-0.47

Because the changes in derived dose at both of depths from their equivalent square values were minor and clinically insignificant, the equivalent square field using the A/P relationship was acceptable to convert the rectangular field to the equivalent square field.

A conclusion can thus be made that the empirical equation based on the MC simulation in the square field size ranging from 3 to 25 cm provides a reliable method for prediction the dose at the surface and the depth of 0.007 cm in clinically relevant rectangular fields.

CHAPTER V

CONCLUSIONS

Surface dose is the deposited dose at the boundary between the air and the patient. It varies considerably within the first few millimeters of depth due to the buildup characteristic of the megavoltage photon beam. For typical therapeutic irradiation, it is about 75-95% of the maximum dose for electron beam and about 10-30% for photon beam. In general, when cancer patients are treated with high energy photon beam, the surface dose is small due to the skin-sparing effect. However, for the unconventional hypofractionated radiation where the fractional dose is extremely high and for the treatment of deep-seated tumors, the skin complications may be the limiting factor in the delivery of high tumor dose. The high radiation exposure may affect the basal cells of the skin and leads to several phases of skin response. Because the severity of skin complication depends on the radiation dose, the amount of surface dose should be taken into account within the treatment criteria while at the same time ensuring sufficient dose to the target volume. Therefore the accurate assessment of surface doses can lead to predict the skin reaction, to guide bolus thickness decision and to design the treatment technique and dose fractionation schemes.

Normally the dose at the surface is primarily contributed from the secondary charged particles mainly affected at the superficial part of the depth dose curve. Therefore the therapeutic photon dose distribution at the surface and the buildup region is consisted of the pure photon dose and the electron contamination dose. These contaminations in the treatment beams are either generated in high-Z components of the accelerator head, e.g. the flattening filter, in the air or inside the patient. Commonly when the photon beam energies are higher, the relative surface doses are lower. Several previous studies have been investigated the sources of contaminating electron for clinical photon beams. All studies indicated that the secondary electrons generated from the treatment head and from the air volume contribute the most of surface dose. Additionally, the surface dose depends on patient-

specific parameter such as the beam energy, the field size, the angle of beam incidence and the use of beam-modifying devices.

Because the different reactions originate from different depths of the skin, the determination of skin dose will be complicated. According to the reports by the ICRU and ICRP, the practical dose determination of the skin layer is at 70 µm depth, which corresponds to the depth of basal layer. The basal cell layer is the interface between the epidermis and dermis layers of the skin and is interested for skin erythema, and also the critical layer for carcinogenesis. Since the thickness of epidermis varies throughout the human body from 0.002-0.006 cm on the trunk and face, and from 0.05 for the eyelid to 1.5 mm for sole of the foot, the clinically relevant depth for skin dose determination should be considered.

In the past, the surface dose from the therapeutic photon beam had been investigated by various dosimeter types such as thermoluminescense dosimeter, radiochromic film, semiconductor diode and many types of parallel-plate ionization chamber. Because the equilibrium condition of charge particle is not met in the buildup region and the dose gradient is also high, a typical dosimeter is not suitable for the measurement of surface dose. Moreover, if the measured point lies within the buildup region, the perturbation from the contaminating electrons in the beam and the secondary electrons generated by photon interactions in the irradiated medium occur. The suggested detector for reliably measuring the surface dose is the extrapolation chamber.

The extrapolation chamber is a parallel-plate ionization chamber with variable sensitive volume, and high accuracy in the non-electronic equilibrium region. The surface dose can be estimated by measuring the ionization per unit volume as a function of electrode spacing and extrapolating to zero electrode spacing. Unfortunately, the extrapolation chamber is not widely used since it is not typically available in most institutes and also its measurement procedure is time-consuming which makes the accurate measurement of the surface dose become clinically impractical. The fixed-electrode separation chambers are commonly available and also convenient to use in the dose measurement. However, their accuracy in the build-up region remains in doubt since there exists a cavity perturbation from the chamber volume causing an excess ionization. To obtain the accurate surface dose, the reading

of ionization should be corrected to take into account the perturbation conditions. Additionally, the most computerized treatment planning systems (TPSs) fail to accurately determine the surface dose. Therefore, it is interesting to develop the method to predict the dose at surface.

In the present, Monte Carlo method has been considered as an accurate tool in dose estimation in radiotherapy, especially in the heterogeneities region or in the regions where the calculation algorithm are in adequate. At the beginning, the undesirable discrepancy between the measurement and Monte Carlo calculation had been reported for the dose in the build-up region. Later on, several recent studies have demonstrated the sound agreement between the results from the Monte Carlo simulation and the measurement using the extrapolation chamber.

In this study, the dose at surface and at depth of 0.007 cm of the 6 MV therapeutic photon beam with various square and rectangular field sizes from the Varian Clinac 23EX linear accelerator were investigated using the MC simulation and the measurement. The dose measurements are performed by four common dosimeters, which are a CC13 compact cylindrical ionization chamber, a PFD^{3G} dosimeter, a Markus parallel-plate ionization chamber and the TLD chips. The percentage surface dose was obtained by extrapolating the percentage doses in the buildup region to the zero depth using the third-order polynomial function.

The experiments were done at the square and rectangular open field defined by the upper and lower jaws. The first set of data was taken with the square open field sizes of 3×3, 5×5, 10×10, 12×12, 15×15, 20×20 and 25×25 cm^2. The second set of data (FIX-X) was taken with the X collimator jaws fixed for the field's side of 20 cm and varying Y collimator to 5, 8, 10, 12, 15, 18 and 20 cm. The data with the Y collimator jaws fixed (FIX-Y) while the X jaws were varied in the same manner was the third set of our data. As a result, the opening field size ranges from 20×5 to 20×20 cm^2 for the second data set and from 5×20 to 20×20 cm^2 for the third data set.

The central axis depth doses from the measurement were performed using four common dosimeters. The readings from each measured position were corrected and then normalized to the maximum depth dose. The surface doses from each dosimeter were then estimated by the extrapolation of the measured dose near the surface.

Because of the limitation of the measurement, the MC simulation is proposed for accurate determination of the surface dose.

The Monte Carlo simulations used in our study were based on the EGSnrc code system, developed by the National Research Council of Canada (NRC). Our 6 MV photon beams from a Varian Clinac 23EX was simulated using the BEAMnrc user code. The dose distribution in a phantom was obtained by the use of DOSXYZnrc user code. Because the influence of energy spread on both depth dose curves and beam profiles was less, the monoenergetic incident electron energy was used for MC simulation. The suitable initial electron energy and the radius of Gaussian distribution of the electron beam incident on the target were determined from the best matching between the simulated and measured results of the percentage depth dose along the central axis and the beam profiles at 10-cm depth for the photon beam's field sizes of 10×10 and 30×30 cm^2. In our comparison, the monoenergentic electron energy and the radius of Gaussian distribution tuning resulted in 6.1 MeV and 1.2 mm, respectively.

Using the phase space file obtained from the BEAMnrc code as an input to the DOSXYZnrc code, the beam's interaction in the water phantom was simulated and, therefore, the deposited dose within a voxel was obtained. The MC simulated depth doses at the beam central axis were obtained for different field sizes and normalized as a percentage of the maximum dose. Here, the percentage dose near or at the phantom surface was estimated by the third-order polynomial extrapolation of the simulated data. Because an extrapolation chamber is not available in our department, our percentage doses at the surface, at depth of 0.007 and 0.05 cm were preliminary compared with the previously reported measurement from similar machines using an extrapolation chamber at the same beam energy to investigate the accuracy of our simulated data. The surface dose clearly increases with increasing field size as consistent with the previous studies. In this study, the percentage of dose at surface and at the depth of 0.007 cm for the field size of 10×10 cm^2 are 16.45% and 18.30%, respectively. Good agreement was generally observed since all of the differences were less than 2%. Therefore, similar to many previous studies our MC simulation has been verified to be a reliable alternative method to determine the surface dose.

As the results, the surface dose derived from both the measurements and the MC simulation increases almost linearly with the side of the square field due to the contaminated electron. The consistency between the measured data from all four detector types were observed for depths beyond the depth of maximum dose, but were all clearly different from each others and also from the MC simulated data in the buildup region. This suggests that reliable measurement of the percentage depth dose beyond the build-up region can be obtained from any of our four detectors.

Compared to the MC simulated data, the measured doses were typically higher near the surface region. A large deviation from the MC simulated results is noticed between the measurement using the CC13 chamber and the PFD^{3G} dosimeter while the results from the TLD and the Markus chamber seem to be in good agreement near the surface region. A similar change in the near surface region between the measured data from both Markus chamber and TLD chip and the simulated data in which these curves have a negative curvature while the trendlines for the CC13 and PFD^{3G} data have positive curvature. The dose at zero depth from each measurement data is always higher than that of Monte Carlo simulation for all of our 4 square fields. The similar observations were also reported in the previous studies. The surface dose from the TLD measurement had the most agreement with the MC simulation. The worst and second worst agreement with the MC simulated data was exhibited by the CC13 and PFD^{3G} detectors, respectively. Interestingly, the dose readings from both CC13 chamber and PFD dosimeter are almost steady near the surface. Within 1 mm from the surface, the percentage dose varies less than 5% for the CC13 chamber and 10% for the PFD^{3G} for the 5×5 cm^2 up to 20×20 cm^2 field sizes while it changes almost 30% in the MC simulation. The insensitivity of depth for dose measurement near the surface using these detectors implies that the high precision of the position of measurement is not necessary.

From the results, these dosimeters are over response for measured the surface dose. To receive the accurately measured dose at surface and at depth of 0.007 cm, the empirical correction factors for each dosimeter used in this study were introduced. These factors have been derived by calculating the ratio of the MC simulated surface dose and the measured value as a function of the length of the square field's side

ranging from 5 to 20 fitted using the polynomial model. In this study, we also presented the correction factors for each dosimeter to estimate the accurate dose at the depth of 0.007 cm. The correction factors at the field size of 10×10 cm^2 are 0.3299 for a CC13 chamber, 0.4244 for a PFD^{3G} dosimeter, 0.7020 for a Markus chamber and 0.9029 for the TLD chip if the clinically depth was at 70 μm. The smallest correction factor, or the largest over-response, was found with the CC13 chamber, whilst the largest correction factor, or the smallest over-response was found with the TLD chip. After applied the over response correction factor for the measured data derived from Markus chamber, the doses at both of depths are in good agreement with the calculated correction factor using Gerbi and Khan's method. The empirical correction of the surface dose presented here is not better than the GK method outside the range of the studied field size (5×5 cm^2 to 20×20 cm^2). Therefore, given the correction factors for the measured surface dose for each of our detectors as a function of the length of the square field's side ranging from 5 to 20 cm. Because of this, both the PFD^{3G} dosimeter and CC13 chamber may be recommended for surface dose measurements if their accurate correction factors are available. Moreover the results derived from these dosimeters could be used as PDD data in the buildup region for a TPS to achieve the accurate dose calculation to skin. For the TLD chip, the correction factor can be used to obtain the accurate measured surface dose on the patient skin in clinical situation.

Typically, several dose parameters from a medical linear accelerator are collected for the square field, but the treatment field in clinical application often used in the rectangular size. To estimate the surface dose of rectangular field from the square field data, the equivalent square formula using the A/P relationship is suggested. The linear relationship between the percentage surface dose and the side of the square field at the field sizes ranging from 5 to 20 cm was observed in the MC-based theoretical. To improve the method for determination of surface dose in the wide ranges, the surface dose of the equivalent square field was then estimated from the second-order polynomial function of the square field doses ranging from 3 to 25 cm. Subsequently, the dose at the surface and at the 0.007 cm depth of the rectangular field was compared with that of the relevant equivalent square field to see whether the

equivalent square field approach is suitable for the surface dose's approximation of the rectangular field from the 6 MV photon beam.

For each rectangular field pattern, the percentage of dose at surface and at the depth of 0.007 cm of the rectangular field and that of its equivalent square field using the A/P relationship were in good agreement with a maximum difference of less than 2%. For the dose in buildup region, the magnitude of this difference is considered to be small and may be clinically neglected. Moreover, the interchange between the X- and Y-collimator resulted in only a minor difference (less than 1%) in the percentage of doses at both of depths. This is because the major contribution to the dose in this region from the photon beam is the contaminant electron which is mainly originated at the flattening filter. The effect of collimator exchange on the surface dose is therefore practically unimportant and can be essentially excluded in the equivalent square formula for the dose determination.

Since the collimator exchange effect on the dose at both depths are not critical, the area-to-perimeter formalism is appropriate. Its applicability to determine the surface dose from rectangular photon beam is conceptually expected to better correlate the surface dose of the rectangular field to that of the square field. In this study, the side of the square field in which the dose at the surface and at the 0.007 cm is available ranged from 3 to 25 cm. Because there are no more elongated fields in which their equivalent squares fall out of our range, the surface dose of the rectangular field, in which its equivalent square side is out of that range, cannot be determined.

As the results, we concluded that the MC simulation can be used as a reliable method for determination the dose at the surface and at the relevant depths for the square and rectangular field sizes. The equations for calculation the dose at surface and the depth of 0.007 cm are presented. Moreover the correction factors for measured dose at the surface and the depth of 0.007 cm obtained from a CC13 chamber, a PFD^{3G} dosimeter, a Markus chamber and the TLD chip are introduced. The accuracy of equations and correction factors, based on the MC simulation is satisfied.

5.1   <u>Suggestion for the future work</u>

This study has only concentrated on the surface of the open field sizes defined by the adjustable collimators of the standard linear accelerator. The effect of a multileaf collimator is not taken into account in these MC simulations. Moreover, the correction factors reported here can be only used to scale the measured dose at the surface region using these dosimeters for the square open fields at 100 cm SSD in 6 megavoltage photon beam from a Varian linear accelerator.

In the future treatment machine, the flattening filter inside the accelerator's head can be removed in some special treatment technique. The effect of flattening filter is not taken into account. Therefore the investigation of the surface dose obtained from the treatment unit without an existence of the flattening filter and the field size defined by a multileaf collimator at different depth and, also, beam energy should be conducted.

REFERENCES

[1] Podgorsak, E.B. <u>Radiation oncology physics: a handbook for teachers and students</u>. Vienna: International Atomic Energy Agency, 2005.

[2] Rubach, A., et al. Dose build-up curves for cobalt-60 irradiation: a systematic error occuring with pancake chamber measurements. <u>Phys Med Biol</u> 31 (1986): 441-448.

[3] Nilsson, B., et al. Surface dose measurements in clinical photon beams. <u>Acta Oncol</u> 28 (1989): 517-542.

[4] Jackson, W., et al. Surface effects of high energy X-rays at oblique incidence. <u>Br J Radiol</u> 44 (1971): 109-115.

[5] Clifton, L.C., Improving the build up and depth dose characteristics of high energy photon beams by using electron filters. <u>Med Phys</u> 6 (1979): 296-301.

[6] Fiorino, C., et al. Skin dose measurements for head and neck radiotherapy. <u>Med Phys</u> 19 (1992): 1263-1266.

[7] Klein, E.E., Purdy, J. Entrance and exit dose regions for a clinic 2100C. <u>Int J Radiat Oncol Biol Phys</u> 27 (1993): 429-435.

[8] Yang, J., et al. Modelling of electron contamination in clinical photon beams of Monte Carlo dose calculation. <u>Phys Med Biol</u> 49 (2004): 2657-2673.

[9] Petti, P.L., et al. Investigation of buildup dose from electron contamination for the clinical photon beams. <u>Med Phys</u> 10 (1983): 18-24.

[10] Nilsson, B., Brahme, A. Absorbed dose from secondary electrons in high energy photon beams. <u>Phys Med Biol</u> 24 (1979): 901-912.

[11] Butson, M.J., Mathur, J.N., et al. Skin dose from radiotherapy X-ray beams: the influence of energy. <u>Australas Radiol</u> 41 (1997): 148-150.

[12] Biggs, P.J., et al. Electrons as the cause of the observed d_{max} shift with field size in high energy photon beams. <u>Med Phys</u> 6 (1979): 291-295.

[13] Nilsson, B. Electron contamination from different materials in high energy photon beams. <u>Phys Med Biol</u> 30 (1985): 139-151.

[14] Beauvais, H., et al. Characteristics of contamination electrons in high energy photon beams. <u>Radiother Oncol</u> 29 (1993): 308-316.

[15] Hannallah, D., et al. Electron disequilibrium in high-energy x-ray beams. <u>Med Phys</u> 23 (1996): 1867-1871.

[16] Hounsell, A.R., et al. Electron contamination and build-up doses in conformal radiotherapy fields. <u>Phys Med Biol</u> 44 (1999): 43-55.

[17] Butson, M.J., Cheung, T., et al. Simulation and measurement of air generated electron contamination in radiotherapy. <u>Radiat Measurements</u> 32 (2000); 105-111.

[18] Klein, E.E., Esthappan, J., et al. Surface and buildup dose characteristics for 6, 10, and 18 MV photons from an Elekta Precise linear accelerator. <u>J Appl Clin Med Phys</u> 4 (2003): 1-7.

[19] Bilge, H., et al. Surface dose and build-up region measurements with wedge filters for 6 and 18 MV photon beams. <u>Jpn J Radiol</u> 28 (2010): 110-116.

[20] Yamaguchi, S., et al. Comparison of 4 MV photon surface dose among Varian, Siemens, and Elekta linear accelerators for tangential breast treatment: a phantom study. Radiat Med 25 (2007): 8-13.

[21] William, P., et al. <u>Gray's Anatomy</u>. London: Churchill Livingston, 1989.

[22] Turesson, I., et al. Repair capacity and kinetics of human skin during fractionated radiotherapy: erythema, desquamation, and telangiectasia after 3 and 5 year's follow-up. <u>Radiother Oncol</u> 15 (1989): 169-188.

[23] Stathakis, S., et al. Ultra-thin TLDs for skin dose determination in high energy photon beams. <u>Phys Med Biol</u> 51 (2006): 3549-3567.

[24] Attix, F.H. <u>Introduction to radiological physics and radiation dosimetry</u>. Weinheim: WILEY-VCH Verlag GmbH & Co. KGaA, 2004.

[25] Shea, E.O., et al. Review of surface dose detectors in radiotherapy. <u>J Radiother Pract</u> 3 (2003): 69-76.

[26] Nilsson, B.O., Montelius, A. Fluence perturbation in photon beams under nonequilibrium conditions. <u>Med Phys</u> 13 (1986): 191-195.

[27] David, E., et al. Determination of build-up region over-response corrections for a Markus chamber. <u>Med Phys</u> 17 (1990): 1041-4.

[28] Gerbi, B.J., et al. Measurement of dose in the buildup region using fixed-separation plane-parallel ionization chambers. Med Phys 17 (1990): 17-26.

[29] Velkley, D.E., et al. Build-up region of megavoltage photon radiation sources. Med Phys 2 (1975): 14-19.

[30] Chetty, I.J., et al. Report of the AAPM Task Group No.105: Issues associated with clinical implementation of Monte Carlo-based photon and electron external beam treatment planning. Med Phys 34 (2007): 4818-4853.

[31] Cherry, P., Duxbury, A. Practical radiotherapy physics and equipment. United Kingdom: WILEY-BLACKWELL publishing, 2009.

[32] Bjarngard, B.E., et al. Doses near the surface in high-energy x-ray beams. Med Phys 22 (1995): 465-468.

[33] Sixel, K.E., et al. Buildup region and depth of dose maximum of megavoltage x-ray beams. Med Phys 21 (1994): 411-416.

[34] Lamb, A., et al. Investigation and modeling of the surface dose from linear accelerator produced 6 and 10 MV photon beams. Phys Med Biol 43 (1998): 1133-1146.

[35] Carl, J., et al. Skin damage probabilities using fixation materials in high-energy photon beams. Radiother Oncol 55 (2000): 191-198.

[36] Ravikumar, M., et al. Dose measurements in the build-up region for the photon beams from Clinac-1800 dual energy medical linear accelerator. Strahlenther Onkol 176 (2000): 223-228.

[37] Parsai, E.I., et al. Surface and build-up region dose analysis for clinical radiotherapy photon beam. Appl Radiat Isot 66 (2008): 1438-1442.

[38] Dogan, N., et al. Surface and build-up region dosimetry for obliquely incident intensity modulated radiotherapy 6 MV x rays. Med Phys 30 (2003): 3091-3096.

[39] Butson, M.J., Cheung, T., et al. Variations in 6MV x-ray radiotherapy build-up dose with treatment distance. Australas Phys Eng Sci Med 26 (2003): 87-88.

[40] Yadav, G., et al. Skin dose estimation for various beam modifiers and source-to-surface distances for 6 MV photons. J Med Phys 34 (2009): 87-92.

[41] Chen, F.Q., et al. Intensity modulated radiation therapy (IMRT) surface dose measurements using a PTW advanced Markus chamber. Australas Phys Eng Sci Med 33 (2010): 23-34.

[42] Rawlinson, J.A., et al. Design of parallel plate ion chambers for build up measurements in megavoltage photon beams. Med Phys 19 (1992): 641-648.

[43] Butson, M.J., Cheung, T., Yu, P.K.N., et al. Measurement of skin dose variations produced by a silicon-based protective dressing in radiotherapy. Phys Med Biol 47 (2002): N145-151.

[44] Yokoyama, S., et al. Surface buildup dose dependence on photon field delivery technique for IMRT. J Appl Clin Med Phys 5 (2004): 71-81.

[45] Hsu, S.H., et al. Assessment of skin dose for breast chest wall radiotherapy as a function of bolus material. Phys Med Biol 53 (2008): 2593-2606.

[46] Rogers, D.W.O. Monte Carlo techniques in radiotherapy. Physics in Canada (2002): 63-70.

[47] Verhaegen, F., et al. Monte Carlo modeling of external radiotherapy photon beams. Phys Med Biol 48 (2003): R107-164.

[48] Zee, W., et al. Calculating photon beam characteristics with Monte Carlo techniques. Med Phys 26 (1999): 1883-1892.

[49] Libby, B., et al. Validation of Monte Carlo generated phase-space descriptions of medical linear accelerators. Med Phys 26 (1999): 1476-1483.

[50] Rogers, J.E. Monte Carlo simulations of dose deposition applied to clinical radiation therapy. Radiat Measurements 41 (2007): S36-44.

[51] Garnica-Garza, H.M. Monte Carlo-derived TLD cross-calibration factors for treatment verification and measurement of skin dose in accelerated partial breast irradiation. Phys Med Biol 54 (2009): 1621-1631.

[52] Berger, M.J. Methods in Computational Physics. New York: Academic, 1963.

[53] Rogers, D.W.O., Kawrakow. I., et al. NRC User Codes for EGSnrc: NRCC report PIRS-702. Ottawa: National Research Council of Canada, 2010.

[54] Karakow, I., Mainegra-Hing, E., et al. EGnrcMP: the multi-platform environment for EGSnrc: NRCC report PIRS-877. Ottawa: National Research Council of Canada, 2006.

[55] Treurniet, J.R., et al. BEAMnrc, DOSYZnrc and BEAMDP GUI User's Manual: NRCC report PIRS-0623. Ottawa: National Research Council of Canada, 2005.

[56] Rogers, D.W.O., Walters, B., et al. BEAMnrc User's Manual: NRCC report PIRS-0509(A). Ottawa: National Research Council of Canada, 2006.

[57] Walters, B., et al. DOSYZnrc User's Manual: NRCC report PIRS-794. Ottawa; National Research Council of Canada, 2006.

[58] Roger, D.W.O., Faddegon, B.A, et al. BEAM: A Monte Carlo code to simulate radiotherapy treatment units. Med Phys 22 (1995): 503-524.

[59] Walters, B.R.B., et al. History by history statistical estimators in the BEAM code system. Ottawa: National Research Council of Canada, 2002.

[60] Deng, J., et al. Photon beam characterization and modeling for Monte Carlo treatment planning. Phys Med Biol 45 (2000): 411-427.

[61] Kawrakow, I., Rogers, D.W.O., et al. Large efficiency improvements in BEAMnrc using directional bremsstrahlung splitting. Med Phys 31 (2004): 2883-2898.

[62] Fix, M.K., et al. Monte Carlo source model for photon beam radiotherapy: photon source characteristics. Med Phys 31 (2004): 3106-3121.

[63] Kawrakow, I., Walters, B.R.B. Efficient photon beam dose calculations using DOSYZnrc with BEAMnrc. Med Phys 33 (2006): 3046-3056.

[64] Sempau, J., et al. DPM, a fast, accurate Monte Carlo code optimized for photon and electron radiotherapy treatment planning dose calculations. Phys Med Biol 45 (2000): 2263-2291.

[65] Ding, G.X. Dose discrepancies between Monte Carlo calculations and measurements in the buildup region for a high-energy photon beam. Med Phys 29 (2002): 2459-2463.

[66] Abdel-rahman, W., et al. validation of Monte Carlo calculated surface doses for megavoltage photon beams. Med Phys 31 (2005): 286-298.

[67] Devic, S., et al. Accurate skin dose measurements using radiochromic film in clinical applications. <u>Med Phys</u> 33 (2006): 1116-1124.

[68] Kim, J.H., et al. An evaluation of calculation parameters in the EGSnrc/BEAMnrc Monte Carlo codes and their effect on surface dose calculation. <u>Med Phys</u> 57 (2012): N267-278.

[69] Day, M.J, et al. The equivalent field method for dose determination in rectangular fields. <u>Br J Radiol</u> 25 (1996): 138-147.

[70] Vanselaar, J.L.M., et al. Is there a need for a revised table of equivalent square fields for the determination of phantom scatter correction factors? <u>Phys Med Biol</u> 42 (1997): 2369-81.

[71] Bjarngard, B.E., Siddon, R.L. A note on equivalent circles, squares, and rectangles. <u>Med Phys</u> 9 (1982): 258-260.

[72] Sanz, D.E. A mathematical study of the area over perimeter rule using the sector-integration equation. <u>Med Phys</u> 27 (2000): 2376-2379.

[73] Vadash, P., et al. An equivalent-square formula for head-scatter factors. <u>Med Phys</u> 20 (1993): 733-734.

[74] Norvill, C.A.J, et al. An investigation of equivalent square formula. <u>Australas Phys Eng Sci Med</u> 31 (2008): 151-153.

[75] Kim, S., Zhu, T.C., et al. An equivalent square field formula for determining head scatter factors of rectangular fields. <u>Med Phys</u> 24 (1997): 1770-1774.

[76] Gosselin, M., et al. Equivalent square as a predictor of depth of dose maximum for megavoltage therapy beams. <u>Med Dosim</u> 21 (1996): 145-148.

[77] Dyk, J.V., Barnett, R.B., et al. Commissioning and quality assurance of treatment planning computers. <u>Int J Radiat Oncol Biol Phys</u> 26 (1993): 261-273.

[78] Fraass, B., et al. American Association of Physicists in Medicine Radiation Therapy Committee Task Group 53: Quality Assurance of Treatment Planning Computers. <u>Med Phys</u> 25 (1998): 1773-1836.

[79] Venselaar, J., et al. Tolerances for the accuracy of photon beam dose calculations of treatment planning systems. <u>Radiother Oncol</u> 60 (2001): 191-201.

[80] Dyk, J.V., et al. <u>Commissioning and quality assurance of computerized planning systems for radiation treatment of cancer: TRS no.430.</u> Vienna: International Atomic Energy Agency, 2004.

[81] Andreo, P., et al. <u>Absorbed dose determination in external beam radiotherapy: TRS no.398.</u> Vienna: International Atomic Energy Agency, 2000.

[82] Gerbi, B.J., Khan, F.M. The polarity effect for commercially available plane-parallel ionization chambers. <u>Med Phys</u> 14 (1987): 210-215.

[83] Paelinck, L., et al. Comparison of build-up dose between Elekta and Varian linear accelerators for high-energy photon beams using radiochromic film and clinical implications for IMRT head and neck treatments. Phys Med Biol 50 (2005): 413-428.

[84] Scarbora, S.B., et al. Variations in photon energy spectra of a 6 MV beam and their impact on TLD response. <u>Med Phys</u> 38 (2011): 2619-2628.

[85] Apipunyasopon, L., et al. An investigation of the depth dose in the build-up region, and surface dose for a 6-MV therapeutic photon beam: Monte Carlo simulation and measurements. <u>J Radiat Res</u> 54 (2013): 374-382.

APPENDICES

APPENDIX A

EGSnrc transport parameters

The EGSnrc code offers an option to facilitate the user in determining the appropriate the transport parameters for improving the accuracy of the simulation and reducing the computing time. There are a wide range of transport parameters that need to be defined. The example of the available option for the transport parameters are listed below.

- AP and AE

AP and AE is the low-energy threshold for secondary bremsstrahlung photons production and for knock-on electrons, respectively. The AE value affects the statistical fluctuations in the electron energy loss, the electron step sizes and the lower limit of ECUT. The interactions are continuous event and give rise to energy losses and direction changes until the photons with energy of at least AP and any electrons with energy of a least AE are discarded. Normally the AE value of 0.70 MeV with a fixed AP of 0.01 MeV is used in the beam modeling. However a higher value of AE is underestimate of the calculated surface dose up to approximately 6% at the depths less than 0.1 mm [64].

- PCUT and ECUT

PCUT and ECUT is the global electron and photon transport cut-off energy in MeV, respectively. The particles that have the energy below the PCUT and ECUT are terminated and their energies are deposited in the current region. Commonly, the PCUT and ECUT values are required to be greater than or equal to AP and AE, respectively. If the ECUT value increases, the fewer low energy electrons are modeled and stored, and the computed times are shorter.

- ECUTRR

ECUTRR is the threshold energy of electron range rejection. The range rejection is used to save computing time for electron transport simulations by calculate the residual range of a charge particle and terminate its history if it cannot escape from the current region. It is also used to avoid simulating those electrons that did not affect the phase space output significantly.

- ESAVE

ESAVE is the threshold energy to turn on the electron range rejection. In particular, the ESAVE value of 2 MeV is performed because it increases the computed speed to 2-3 times and ignores the photon that produced due to bremsstrahlung anywhere in the accelerator head reaching the phantom surface only 1%. Therefore any electron energy below 2.0 MeV is estimated to determine whether its range within the component modules is short enough to terminate its transport.

- BCA

BCA is used to transport electrons across the interfaces between different materials and/or scoring regions where the electrons are within the skin depth distance, defined as the distance from the region boundary in which the chosen BCA algorithm comes into effect. There are two possible algorithms for BCA: EXACT and PRESTA-I. EXACT algorithm utilizes a single elastic scattering mode to cross the boundaries given by the EGSnrc input. PRESTA-I uses multiple scattering mode with no lateral correction by the skin depth distance.

- ESA

ESA is used to calculate lateral and longitudinal corrections by measuring the distance along the initial direction of motion to account for multiple elastic scattering in an electron step. There are two algorithms available: PRESTA-II and PRESTA-I. ESTEPE is the maximum fractional energy loss per electron step. It used to determine how far an electron can potentially go in one step, and the length of time and the required accuracy for simulation.

APPENDIX B

Example of EGSnrc/BEAM input file for Varian Clinac 23EX linear accelerator machine simulation

```
6.1MeV1.2mm_1000M_Jaw10                                    #!GUI1.0
AIR521ICRU
0, 0, 0, 0, 1, 3, 0, IWATCH ETC.
1000000000, 33, 97, 999, 0, 0, 0, 4, NCASE ETC.
15, 15, NSPLIT
-1, 19, -0.12, 0, 0, 1, 0, 0.0, 0.0, 0.0, IQIN, ISOURCE + OPTIONS
0, MONOENERGETIC
6.1
0, 0, 0.521, 0.01, 0, 1, 0.521, 0, ECUT, PCUT, IREJCT, ESAVE
0, 1, 7, 1, 7, PHOTON FORCING
1, 9, SCORING INPUT
1, 1
5,
0, DOSE COMPONENTS
0.0, Z TO FRONT FACE

*********** start of CM SLABS with identifier TARGET ***********
0.5, RMAX
TARGET_6.1MeV
2, NSLABS
0, ZMIN
0.0889, 0.521, 0.01, 0, 0, 0
W521ICRU
0.15748, 0.521, 0.01, 0, 0, 0
CU521ICRU

*********** start of CM CONS3R with identifier PRI_COLL ***********
5, RMAX
PRI_COLL_6.1MeV
0.508, ZMIN
7.292, ZTHICK
4, NUM_NODE
0.508, 0.75,
1.6, 0.75,
1.6, 0.3989,
7.8, 1.9447,
0.521, 0.01, 0, 0, 0,
VACUUM
0.521, 0.01, 0, 0, 0,
```

W521ICRU

*********** start of CM SLABS with identifier VAC_WIND ***********
1.956, RMAX
VAC_WIND_6.1MeV
2, NSLABS
7.8, ZMIN
1.2, 0.521, 0.01, 0, 0, 0
VACUUM
0.0254, 0.521, 0.01, 0, 0, 0
BE521ICRU

*********** start of CM FLATFILT with identifier FLAT_FIL ***********
3.81, RMAX
FLAT_FIL_6.1MeV
10.4, ZMIN
19, NUMBER OF LAYERS
1, 0.033, # CONES, ZTHICK OF LAYER 1
0.064,
0.127,
1, 0.038, # CONES, ZTHICK OF LAYER 2
0.127,
0.191,
1, 0.046, # CONES, ZTHICK OF LAYER 3
0.191,
0.254,
1, 0.112, # CONES, ZTHICK OF LAYER 4
0.254,
0.381,
1, 0.122, # CONES, ZTHICK OF LAYER 5
0.381,
0.508,
1, 0.117, # CONES, ZTHICK OF LAYER 6
0.508,
0.635,
1, 0.117, # CONES, ZTHICK OF LAYER 7
0.635,
0.762,
1, 0.114, # CONES, ZTHICK OF LAYER 8
0.762,
0.889,
1, 0.112, # CONES, ZTHICK OF LAYER 9
0.889,
1.016,
1, 0.216, # CONES, ZTHICK OF LAYER 10
1.016,
1.27,

1, 0.201, # CONES, ZTHICK OF LAYER 11
1.27,
1.524,
1, 0.193, # CONES, ZTHICK OF LAYER 12
1.524,
1.778,
1, 0.17, # CONES, ZTHICK OF LAYER 13
1.778,
2.032,
1, 0.165, # CONES, ZTHICK OF LAYER 14
2.032,
2.286,
1, 0.142, # CONES, ZTHICK OF LAYER 15
2.286,
2.54,
1, 0.14, # CONES, ZTHICK OF LAYER 16
2.54,
2.794,
1, 0.147, # CONES, ZTHICK OF LAYER 17
2.794,
3.061,
1, 0.114, # CONES, ZTHICK OF LAYER 18
3.302,
3.366,
1, 0.0, # CONES, ZTHICK OF LAYER 19
3.366,
3.381,
0.521, 0.01, 0, 0,
CU521ICRU
0.521, 0.01, 0, 0,
AIR521ICRU
0.521, 0.01, 0, 0,
CU521ICRU
0.521, 0.01, 0, 0,
AIR521ICRU
0.521, 0.01, 0, 0,
CU521ICRU
0.521, 0.01, 0, 0,
AIR521ICRU
0.521, 0.01, 0, 0,
CU521ICRU
0.521, 0.01, 0, 0,
AIR521ICRU
0.521, 0.01, 0, 0,
CU521ICRU
0.521, 0.01, 0, 0,
AIR521ICRU

0.521, 0.01, 0, 0,
CU521ICRU
0.521, 0.01, 0, 0,
AIR521ICRU
0.521, 0.01, 0, 0,
CU521ICRU
0.521, 0.01, 0, 0,
AIR521ICRU
0.521, 0.01, 0, 0,
CU521ICRU
0.521, 0.01, 0, 0,
AIR521ICRU
0.521, 0.01, 0, 0,
CU521ICRU
0.521, 0.01, 0, 0,
AIR521ICRU
0.521, 0.01, 0, 0,
CU521ICRU
0.521, 0.01, 0, 0,
AIR521ICRU
0.521, 0.01, 0, 0,
CU521ICRU
0.521, 0.01, 0, 0,
AIR521ICRU
0.521, 0.01, 0, 0,
CU521ICRU
0.521, 0.01, 0, 0,
AIR521ICRU
0.521, 0.01, 0, 0,
CU521ICRU
0.521, 0.01, 0, 0,
AIR521ICRU
0.521, 0.01, 0, 0,
CU521ICRU
0.521, 0.01, 0, 0,

*********** start of CM CHAMBER with identifier CHAMBER ***********
6, RMAX
CHAMBER_6.1MV
14.2, ZMIN
1, 11, 1, N_TOP, N_CHM, N_BOT
0.0635, 5.8, 0, ZTHICK, RCYS, FLAG FOR LAYER 1 IN TOP
0.521, 0.01, 0, 0,
AIR521ICRU
0.521, 0.01, 0, 0,
AIR521ICRU
5.5, 5.7, 5.8, RADII FOR CENTRAL PART

0.0127, 0, ZTHICK, FLAG FOR LAYER 1 IN CENTRAL PART
0.521, 0.01, 0, 0,
KAPTON521ICRU
0.18, 0, ZTHICK, FLAG FOR LAYER 2 IN CENTRAL PART
0.521, 0.01, 0, 0,
AIR521ICRU
0.0127, 0, ZTHICK, FLAG FOR LAYER 3 IN CENTRAL PART
0.521, 0.01, 0, 0,
KAPTON521ICRU
0.18, 0, ZTHICK, FLAG FOR LAYER 4 IN CENTRAL PART
0.521, 0.01, 0, 0,
AIR521ICRU
0.0127, 0, ZTHICK, FLAG FOR LAYER 5 IN CENTRAL PART
0.521, 0.01, 0, 0,
KAPTON521ICRU
0.18, 0, ZTHICK, FLAG FOR LAYER 6 IN CENTRAL PART
0.521, 0.01, 0, 0,
AIR521ICRU
0.127, 0, ZTHICK, FLAG FOR LAYER 7 IN CENTRAL PART
0.521, 0.01, 0, 0,
KAPTON521ICRU
0.18, 0, ZTHICK, FLAG FOR LAYER 8 IN CENTRAL PART
0.521, 0.01, 0, 0,
AIR521ICRU
0.0127, 0, ZTHICK, FLAG FOR LAYER 9 IN CENTRAL PART
0.521, 0.01, 0, 0,
KAPTON521ICRU
0.18, 0, ZTHICK, FLAG FOR LAYER 10 IN CENTRAL PART
0.521, 0.01, 0, 0,
KAPTON521ICRU
0.0127, 0, ZTHICK, FLAG FOR LAYER 11 IN CENTRAL PART
0.521, 0.01, 0, 0,
KAPTON521ICRU
0.521, 0.01, 0, 0,   chamber wall
AIR521ICRU
0.521, 0.01, 0, 0,   gap
AIR521ICRU
0.521, 0.01, 0, 0,   container
AIR521ICRU
0.0635, 5.8, 0, ZTHICK, RCYS, FLAG FOR LAYER 1 IN BOTTOM PART
0.521, 0.01, 0, 0,
AIR521ICRU
0.521, 0.01, 0, 0,
AIR521ICRU
0, MRNGE

*********** start of CM MIRROR with identifier MIRROR ***********
8, RMAX
MIRROR_6.1MeV
17, 10, ZMIN, ZTHICK
7.13442, -7.14328, XFMIN, XBMIN
1, # LAYERS
0.00508, thickness of layer 1
0.521, 0.01, 0, 0,
MYLAR521ICRU
0.521, 0.01, 0, 0,
AIR521ICRU
0.521, 0.01, 0, 0,
AIR521ICRU

*********** start of CM JAWS with identifier SEC_COLL ***********
20.5, RMAX
SEC_COLL6.1MeV
2, # PAIRED BARS OR JAWS
Y
28, 35.8, 1.4, 1.79, -1.4, -1.79,
X
36.7, 44.5, 1.835, 2.225, -1.835, -2.225,
0.521, 0.01, 0, 0,
0.521, 0.01, 0, 0,
W521ICRU
0.521, 0.01, 0, 0,
W521ICRU

*********** start of CM DYNVMLC with identifier MLC ***********
20.1, RMAX
DYNVMLC6.1MeV
1, 3, ORIENT, NGROUP
48.25, ZMIN
6.7, ZTHICK
0.5327, 0.01, 0.04, 0.1354, 0.3673, 0.1396, 48.25, 48.533, 51.524, 51.732, 52.9618, 53.2968, 2, 54.556, 54.812,
0.2375, 0.04, 0.0246, 0.1054, 0.1371, 0.1371, 48.345, 48.6096, 49.5752, 49.7802, 2, 51.625, 51.625, 54.626, 54.745,
0.2338, 0.0246, 0.04, 0.0354, 0.1405, 0.1316, 48.412, 48.531, 51.631, 51.732, 53.3293, 53.6293, 2, 54.5474, 54.812,
10, 1
40, 2
10, 1
-10.0, START
0.006, LEAFGAP
0, ENDTYPE
8, ZFOCUS or RADIUS of leaf ends

0, ZFOCUS of leaf sides
-20, 20, 20
-20, 20, 20
-20, 20, 20
0.521, 0.01, 0, 0,
AIR521ICRU
0.521, 0.01, 0, 0, 0,
W521ICRU
0.521, 0.01, 0, 0,
AIR521ICRU

*********** start of CM SLABS with identifier PS_1 ***********
20.5, RMAX
PS2_6.1MeV
1, NSLABS
89.5, ZMIN
0.5, 0.521, 0.01, 0, 0, 0
AIR521ICRU

*********************end of all CMs***************************

:Start MC Transport Parameter:

 Global ECUT= 0.521
 Global PCUT= 0.01
 Global SMAX= 5
 ESTEPE= 0.25
 XIMAX= 0.5
 Boundary crossing algorithm= EXACT
 Skin depth for BCA= 0
 Electron-step algorithm= PRESTA-II
 Spin effects= On
 Brems angular sampling= Simple
 Brems cross sections= BH
 Bound Compton scattering= Off
 Pair angular sampling= Simple
 Photoelectron angular sampling= Off
 Rayleigh scattering= Off
 Atomic relaxations= Off
 Electron impact ionization= Off

 :Stop MC Transport Parameter:
 ##########################

APPENDIX C

<u>Example of EGSnrc/DOSXYZ output file for simulated phantom</u>

3 3 56 ·······▶ *number of voxels in x, y and z directions*
 -14.5 -0.5 0.5 14.5   *voxel boundaries (cm) in x direction*
 -14.5 -0.5 0.5 14.5   *voxel boundaries (cm) in y direction*

  0. 0.0140000 0.0280000 0.0420000 0.0560000 0.0700000
  0.0839999 0.0979999 0.111999 0.126000 0.140000
  0.153999 0.167999 0.181999 0.195999 0.209999 0.223999
  0.237999 0.252000 0.266000 0.280000 0.294 0.307999   *voxel*
  0.508000 0.708000 0.907999 1.10800 1.30800 1.50800   ·········▶   *boundaries*
  1.70800 1.90800 2.40800 2.90800 3.40800 3.90800   *(cm) in z*
  4.40799 4.90799 5.40799 5.90799 6.40799 6.90799   *direction*
  7.40799 7.90799 8.40799 8.90799 9.40799 9.90799
  10.408 10.908 11.408 11.908 12.408 12.908 13.408 13.908 14.408 14.908

  1.95678E-17 2.35821E-17 1.96950E-17 3.0223E-17 3.61956E-17
  3.01593E-17 1.95449E-17 2.32146E-17 1.97106E-17 2.282E-17
  2.75894E-17 2.29522E-17 3.62525E-17 4.32627E-17
  3.62603E-17 2.29340E-17 2.72262E-17 2.28215E-17
  2.52837E-17 3.09773E-17 2.53242E-17 4.11366E-17
  4.85329E-17 4.12654E-17 2.57315E-17 3.0728E-17 2.55613E-17
  2.76979E-17 3.38246E-17 2.76663E-17 4.55424E-17   *Dose values*
  5.46677E-17 4.49664E-17 2.76738E-17 3.36360E-17   ·········▶   *array (n_x n_y n_z*
  2.78195E-17 2.96157E-17 3.58982E-17 2.97207E-17   *values)*
  4.96831E-17 5.8617E-17 4.88296E-17 2.9730E-17 3.57818E-17
  3.0007E-17 3.12167E-17 3.80310E-17 3.12944E-17 5.27513E-17
  6.33108E-17 5.21787E-17 3.16546E-17 3.85102E-17
  3.16022E-17 3.30932E-17 4.06869E-17 3.29716E-17 5.6336E-17
  6.67689E-17 5.49579E-17 3.32289E-17 4.10584E-17
  3.32065E-17 3.44472E-17 4.18748E-17 3.44148E-17
  5.89702E-17 7.06798E-17 5.84870E-17 3.44714E-17
  4.22994E-17 3.451E-17 3.58323E-17 4.35767E-17 3.59512E-17

  0.00529607 0.00959040 0.00527111 0.00853894 0.0154372
  0.00858612 0.00527971 0.00947475 0.00532411 0.00511089
  0.00922649 0.00511365 0.00814935 0.0146892 0.00816233
  0.0050737 0.00920248 0.00510711 0.00493942 0.00888652
  0.0049420 0.0077850 0.0142171 0.00781486 0.00493514   ·········▶   *Error values*
  0.00892275 0.00495088 0.00480267 0.00862849 0.00480712   *array*
  0.00754311 0.0136523 0.00755102 0.0047810 0.00858042
  0.00479579 0.00468770 0.0083989 0.00469275 0.00729105
  0.0132781 0.00731394 0.00468056 0.00837871 0.00466501

APPENDIX D

Calibration factor for sensitivity of TLDs in column no. 1-8

TLD code		C_{ij} (nC/Gy)	TLD code		C_{ij} (nC/Gy)
Column 1	A	9.0360	Column 5	A	11.4288
	B	9.3329		B	11.5703
	C	9.4771		C	11.7852
	D	9.4834		D	11.8845
	E	9.5256		E	11.8900
	F	9.6747		F	11.8935
	G	9.7796		G	11.9895
	H	9.9777		H	12.0642
	I	10.0245		I	12.1320
	J	10.0360		J	12.1692
Column 2	A	10.1092	Column 6	A	12.1847
	B	10.2388		B	12.1850
	C	10.3012		C	12.1890
	D	10.3652		D	12.2268
	E	10.3780		E	12.3032
	F	10.3850		F	12.3362
	G	10.4202		G	12.4042
	H	10.4350		H	12.4282
	I	10.4580		I	12.4785
	J	10.4705		J	12.5295
Column 3	A	10.5127	Column 7	A	12.5700
	B	10.5185		B	12.5817
	C	10.5952		C	12.6857
	D	10.6200		D	12.8448
	E	10.7083		E	12.8578
	F	10.7172		F	12.8600
	G	10.8400		G	12.9975
	H	10.8417		H	13.0487
	I	10.8803		I	13.0780
	J	10.8808		J	13.1185

(continued)

TLD code		C_{ij} (nC/Gy)	TLD code		C_{ij} (nC/Gy)
Column 4	A	10.9552	Column 8	A	13.1765
	B	10.9972		B	13.2137
	C	11.0393		C	13.3047
	D	11.1842		D	13.3130
	E	11.1910		E	13.5723
	F	11.2215		F	13.7738
	G	11.2305		G	13.8082
	H	11.2663		H	14.0048
	I	11.2885			
	J	11.3375			

APPENDIX E

The percentage depth dose of the square open field sizes derived from the MC simulation at the depth of 0.007 to 5.158 cm for the 6 MV photon beam.

Depth (cm)	Field sizes (cm^2)						
	3×3	5×5	10×10	12×12	15×15	20×20	25×25
0.007	11.79	13.60	18.47	21.76	23.61	30.12	32.70
0.021	16.44	19.81	24.11	27.29	30.18	34.56	38.34
0.035	21.13	24.30	29.26	31.49	34.20	39.31	42.11
0.049	27.06	28.25	33.48	35.78	37.35	43.28	45.10
0.063	28.61	31.99	37.38	39.80	41.64	46.06	47.98
0.077	32.07	34.98	40.49	43.18	45.63	47.38	51.87
0.091	36.12	38.51	43.31	46.21	48.60	50.06	52.67
0.105	37.61	42.31	46.79	48.66	50.49	53.64	55.75
0.119	41.05	43.87	48.72	51.38	53.59	57.30	58.67
0.133	43.87	46.17	51.89	52.86	56.05	61.22	62.48
0.147	47.69	49.44	53.94	54.56	57.65	60.66	63.58
0.161	50.14	50.35	56.29	58.14	61.20	63.84	66.73
0.175	53.05	53.76	57.42	60.27	62.10	65.67	67.93
0.189	53.13	55.52	58.80	61.99	63.38	66.15	68.26
0.203	56.09	57.24	61.45	62.78	66.43	69.71	68.20
0.217	58.73	58.88	62.81	66.78	68.43	70.62	71.74
0.231	59.52	61.89	65.41	67.70	68.86	72.18	71.60
0.245	60.70	63.19	67.20	67.12	71.43	73.36	72.44
0.259	63.73	66.08	67.29	69.88	72.74	74.26	73.53
0.273	65.44	65.87	69.26	71.88	74.20	75.68	76.08
0.287	67.37	65.96	70.84	72.90	75.04	78.43	77.13
0.301	68.96	68.84	71.81	72.85	75.67	78.83	78.06
0.408	76.77	77.45	80.06	81.46	83.28	85.49	84.85
0.608	86.81	87.93	89.84	91.60	91.92	93.51	91.76
0.808	93.02	94.25	95.69	97.42	96.82	98.22	95.55
1.008	96.55	96.90	98.65	100.03	98.75	99.97	97.66
1.208	98.18	98.79	99.99	100.58	100.48	100.70	98.27
1.408	100.35	100.27	100.17	100.24	100.57	100.09	100.04
1.508	100.00	100.00	100.00	100.00	100.00	100.00	100.00
1.608	99.65	99.73	99.83	99.76	99.43	99.91	99.96
1.808	98.81	99.25	99.10	100.16	98.69	99.87	97.70
2.158	98.17	98.28	97.85	98.40	97.48	98.82	95.91
2.658	95.90	95.29	97.00	97.16	95.82	96.40	95.35
3.158	92.80	92.79	93.72	94.19	94.40	94.88	92.95
3.658	88.87	90.74	91.76	92.63	92.39	92.83	90.86
4.158	86.53	88.41	89.86	90.28	89.94	91.62	89.50
4.658	83.64	85.43	87.68	88.71	87.82	88.74	87.19
5.158	82.76	83.22	84.89	86.37	86.69	87.33	84.70

APPENDIX F

The percentage depth dose of the rectangular open field sizes derived from the MC simulation at the depth of 0.007 to 5.158 cm for the 6 MV photon beam.

Depth (cm)	Field sizes (cm^2)								
	5×15	15×5	5×20	20×5	7×18	18×7	8×20	20×8	10×20
0.007	16.64	16.57	17.20	17.81	19.05	19.70	20.49	20.86	22.41
0.021	22.03	22.41	23.29	23.14	24.59	25.07	27.14	25.94	28.12
0.035	26.37	26.52	27.61	27.99	30.12	29.59	30.97	30.32	32.66
0.049	30.53	31.40	31.74	32.14	35.01	33.52	34.84	35.04	37.14
0.063	34.06	36.03	35.53	35.24	38.04	36.82	38.95	37.94	40.49
0.077	38.63	38.58	38.20	39.54	39.87	40.02	42.04	41.66	43.90
0.091	41.37	41.43	42.68	43.38	44.27	43.05	45.55	44.09	46.51
0.105	44.58	44.88	45.54	45.30	46.81	45.67	47.94	46.57	49.06
0.119	47.03	47.85	47.75	48.62	49.54	49.64	50.02	49.01	52.88
0.133	50.09	50.49	49.77	49.84	51.80	51.60	53.15	51.10	54.96
0.147	51.58	52.60	52.20	52.83	54.15	52.77	55.28	53.95	56.44
0.161	52.37	54.49	54.02	55.75	56.38	55.67	58.12	55.76	59.18
0.175	55.88	55.33	57.27	56.40	58.62	57.21	59.62	56.82	60.34
0.189	57.10	56.91	59.47	58.05	60.52	58.65	61.07	59.20	61.90
0.203	58.57	59.33	61.98	60.76	62.34	61.53	62.61	62.39	64.61
0.217	61.51	62.21	62.52	62.88	64.28	63.66	63.61	65.02	66.60
0.231	64.28	65.15	64.96	64.36	65.33	65.44	66.03	65.47	68.05
0.245	64.62	65.50	66.91	65.64	65.99	66.60	67.15	66.68	69.48
0.259	66.03	67.35	68.09	67.49	68.87	67.73	68.57	68.91	69.70
0.273	67.97	68.79	69.88	69.98	70.60	70.07	68.92	70.23	73.60
0.287	67.84	70.61	70.90	69.76	71.05	71.18	71.17	71.23	72.45
0.301	70.56	70.63	72.91	72.07	71.03	72.20	73.07	71.24	74.53
0.408	78.34	78.74	80.20	80.45	80.44	80.08	80.35	80.17	83.16
0.608	88.93	88.55	90.18	91.51	90.38	89.61	89.03	91.08	92.04
0.808	94.78	94.54	95.84	95.70	96.45	95.19	96.15	95.72	97.52
1.008	97.83	98.62	98.41	98.31	99.41	97.34	98.31	98.01	98.28
1.208	100.15	100.36	100.21	99.43	100.43	99.93	98.66	99.53	99.49
1.408	100.04	100.41	100.43	100.27	100.06	100.02	98.99	100.38	99.66
1.508	100.00	100.00	100.00	100.00	100.00	100.00	100.00	100.00	100.00
1.608	99.96	99.59	99.57	99.73	99.94	99.98	100.00	99.62	100.00
1.808	100.08	99.57	98.89	99.38	100.07	100.16	99.66	99.87	100.06
2.158	98.36	99.13	98.40	98.61	98.75	97.86	97.58	98.04	98.73
2.658	95.97	95.74	96.14	96.57	97.41	96.04	95.69	96.18	97.10
3.158	93.73	94.29	93.95	94.44	95.12	93.90	92.95	93.61	94.90
3.658	91.44	91.29	91.88	91.35	91.94	91.86	91.45	91.46	92.75
4.158	88.64	89.67	89.03	89.20	89.96	89.44	89.08	90.06	90.83
4.658	86.69	87.46	87.24	86.96	88.51	87.48	86.88	88.22	88.61
5.158	84.51	85.56	84.88	84.84	86.08	86.14	85.08	85.90	85.51

(Continued)

Depth	Field sizes (cm^2)								
(cm)	20×10	12×17	17×12	12×20	20×12	15×20	20×15	18×20	20×18
0.007	22.09	24.14	22.91	24.16	24.40	25.87	25.72	28.37	27.51
0.021	27.82	29.63	29.27	29.57	29.12	31.54	31.59	32.92	32.52
0.035	32.39	33.36	33.00	33.60	33.22	36.83	36.12	38.34	37.50
0.049	36.74	37.55	38.26	37.87	37.53	41.05	39.33	41.60	41.47
0.063	41.08	41.34	42.20	40.21	40.71	43.58	44.06	44.16	44.56
0.077	43.55	44.25	44.45	44.77	43.87	47.02	47.03	48.24	49.40
0.091	46.46	47.12	46.33	47.62	48.06	51.00	49.34	51.12	51.47
0.105	50.51	49.33	50.05	49.65	50.48	53.11	52.51	54.45	52.98
0.119	52.59	51.89	51.86	52.55	52.53	54.46	54.40	57.42	56.52
0.133	53.93	54.32	54.49	53.45	53.34	56.65	57.38	59.19	58.78
0.147	56.79	56.11	56.20	57.14	57.20	59.49	58.87	62.41	59.67
0.161	58.20	58.70	59.15	58.16	58.34	61.23	60.46	62.11	62.64
0.175	61.82	60.40	60.63	58.46	60.32	63.90	62.37	64.27	64.62
0.189	61.87	62.80	62.08	61.72	62.33	65.73	64.56	66.08	66.02
0.203	65.25	65.84	64.53	65.57	63.89	67.79	66.39	68.06	66.47
0.217	65.98	65.61	65.85	66.41	66.24	68.56	67.09	68.89	69.90
0.231	67.91	65.99	67.31	67.83	66.97	69.84	69.16	70.99	71.18
0.245	69.27	68.52	68.65	69.33	69.69	71.66	70.29	72.22	72.47
0.259	70.82	69.24	71.17	70.96	72.20	72.45	71.35	73.81	73.29
0.273	73.17	71.26	71.57	72.31	71.33	74.60	73.25	75.78	73.41
0.287	73.62	73.79	71.85	73.67	73.43	76.04	75.32	79.48	75.91
0.301	75.30	73.85	74.92	75.00	74.47	75.51	76.65	78.75	77.53
0.408	82.62	81.80	81.93	82.21	81.99	83.23	83.83	85.17	83.80
0.608	91.59	91.07	90.39	91.97	90.40	91.60	93.02	94.19	91.34
0.808	95.99	96.20	96.75	96.99	95.77	97.10	97.60	98.56	96.02
1.008	98.30	98.34	97.70	99.42	98.19	99.11	100.31	100.81	99.11
1.208	98.29	99.35	99.93	99.34	99.93	99.72	100.47	101.06	100.07
1.408	99.52	100.04	99.72	99.28	99.38	100.39	99.67	101.57	100.48
1.508	100.00	100.00	100.00	100.00	100.00	100.00	100.00	100.00	100.00
1.608	100.48	99.96	100.28	100.00	100.00	99.61	100.33	100.00	100.00
1.808	100.99	99.30	99.51	99.55	98.40	99.41	99.31	101.26	99.72
2.158	99.10	97.83	98.53	97.96	96.58	98.93	98.27	98.87	98.05
2.658	97.23	95.18	96.17	96.13	95.28	96.54	95.42	97.59	95.95
3.158	94.52	93.88	93.87	94.47	93.15	94.41	94.67	95.63	93.72
3.658	92.29	91.42	91.78	92.27	91.24	92.96	92.43	92.93	91.86
4.158	89.91	89.40	90.31	89.60	89.63	90.69	90.34	91.60	89.84
4.658	88.73	87.39	87.96	87.72	87.43	88.74	88.07	89.33	87.51
5.158	86.64	85.52	85.40	85.56	85.22	86.31	86.09	87.10	86.31

APPENDIX G

The percentage depth dose of the square open field sizes derived from the measurement using CC13 dosimeter at the depth of 0.010 to 3.000 cm in Blue water phantom for the 6 MV photon beam.

Depth (cm)	Field sizes (cm^2)			
	5×5	10×10	15×15	20×20
0.010	50.70	56.16	60.68	64.65
0.020	51.70	56.91	61.67	65.35
0.040	52.69	57.65	62.79	66.58
0.060	53.86	59.55	63.90	67.80
0.080	55.98	61.53	65.76	69.52
0.100	58.02	63.43	67.54	71.17
0.120	59.99	65.27	69.26	72.74
0.140	61.89	67.03	70.90	74.25
0.160	63.73	68.72	72.48	75.70
0.180	65.49	70.34	73.99	77.08
0.200	67.19	71.91	75.43	78.40
0.220	68.83	73.40	76.82	79.67
0.240	70.40	74.84	78.14	80.88
0.260	71.92	76.22	79.41	82.03
0.280	73.38	77.54	80.62	83.13
0.300	74.78	78.80	81.78	84.18
0.320	76.12	80.01	82.88	85.17
0.340	77.41	81.17	83.94	86.12
0.360	78.65	82.28	84.94	87.03
0.380	79.84	83.34	85.90	87.89
0.400	80.98	84.35	86.81	88.70
0.420	82.07	85.31	87.67	89.48
0.440	83.12	86.23	88.50	90.21
0.460	84.12	87.11	89.28	90.91
0.480	85.07	87.94	90.02	91.57
0.500	85.99	88.74	90.72	92.19
0.520	86.86	89.49	91.39	92.78
0.540	87.69	90.21	92.02	93.33
0.560	88.49	90.90	92.61	93.86
0.580	89.24	91.54	93.18	94.35
0.600	89.96	92.16	93.71	94.81
0.620	90.65	92.74	94.21	95.25
0.640	91.30	93.29	94.68	95.65
0.660	91.92	93.81	95.12	96.04
0.680	92.51	94.30	95.53	96.39
0.700	93.07	94.76	95.92	96.73

(Continued)

Depth (cm)	Field sizes (cm^2)			
	5×5	10×10	15×15	20×20
0.720	93.60	95.20	96.28	97.04
0.740	94.10	95.61	96.62	97.32
0.760	94.57	95.99	96.94	97.59
0.780	95.01	96.35	97.23	97.84
0.800	95.43	96.69	97.51	98.07
0.820	95.83	97.01	97.76	98.28
0.840	96.20	97.31	97.99	98.47
0.860	96.55	97.58	98.21	98.65
0.880	96.87	97.84	98.41	98.81
0.900	97.18	98.08	98.59	98.96
0.920	97.46	98.30	98.75	99.09
0.940	97.73	98.50	98.91	99.21
0.960	97.97	98.69	99.04	99.32
0.980	98.20	98.86	99.16	99.41
1.000	98.41	99.02	99.27	99.49
1.120	99.36	99.69	99.70	99.79
1.140	99.47	99.76	99.74	99.81
1.160	99.57	99.83	99.77	99.82
1.180	99.65	99.88	99.79	99.83
1.200	99.73	99.93	99.80	99.83
1.220	99.79	99.96	99.81	99.83
1.240	99.85	99.99	99.81	99.82
1.260	99.89	100.02	99.81	99.80
1.280	99.93	100.03	99.80	99.78
1.300	99.96	100.04	99.79	99.76
1.320	99.98	100.04	99.77	99.73
1.340	99.99	100.04	99.75	99.70
1.360	100.00	100.03	99.72	99.66
1.380	100.00	100.02	99.69	99.63
1.400	99.99	100.00	99.65	99.59
1.420	99.97	99.98	99.62	99.54
1.440	99.96	99.95	99.58	99.50
1.460	99.93	99.93	99.53	99.45
1.480	99.90	99.89	99.49	99.40
1.500	99.87	99.86	99.44	99.35
1.520	99.83	99.82	99.40	99.30
1.540	99.79	99.77	99.35	99.25
1.560	99.74	99.73	99.29	99.19
1.580	99.69	99.68	99.24	99.14
1.600	99.64	99.63	99.19	99.08
1.62	99.59	99.58	99.13	99.02
1.64	99.53	99.53	99.08	98.96

(Continued)

Depth (cm)	Field sizes (cm^2)			
	5×5	10×10	15×15	20×20
1.66	99.47	99.47	99.02	98.90
1.68	99.40	99.41	98.96	98.84
1.70	99.34	99.36	98.91	98.78
1.72	99.27	99.30	98.85	98.72
1.74	99.20	99.24	98.79	98.66
1.76	99.13	99.18	98.73	98.60
1.78	99.06	99.11	98.67	98.54
1.80	98.99	99.05	98.61	98.47
1.82	98.91	98.98	98.55	98.41
1.84	98.84	98.92	98.49	98.35
1.86	98.76	98.85	98.43	98.29
1.88	98.68	98.79	98.37	98.22
1.90	98.61	98.72	98.32	98.16
1.92	98.53	98.65	98.26	98.09
1.94	98.45	98.58	98.20	98.03
1.96	98.37	98.51	98.14	97.96
1.98	98.29	98.44	98.08	97.90
2.00	98.21	98.37	98.02	97.83
2.12	97.71	97.94	97.65	97.43
2.14	97.63	97.87	97.59	97.36
2.16	97.55	97.79	97.53	97.29
2.18	97.47	97.72	97.46	97.23
2.20	97.38	97.64	97.40	97.15
2.22	97.30	97.57	97.34	97.08
2.24	97.21	97.49	97.27	97.01
2.26	97.13	97.41	97.21	96.94
2.28	97.04	97.34	97.14	96.87
2.30	96.96	97.26	97.08	96.79
2.32	96.87	97.18	97.01	96.72
2.34	96.79	97.10	96.94	96.64
2.36	96.70	97.02	96.87	96.57
2.38	96.61	96.94	96.80	96.49
2.40	96.53	96.85	96.73	96.42
2.42	96.44	96.77	96.66	96.34
2.44	96.35	96.69	96.59	96.26
2.46	96.26	96.60	96.52	96.18
2.48	96.17	96.52	96.44	96.10
2.50	96.08	96.43	96.37	96.02
2.52	95.98	96.34	96.29	95.94
2.54	95.89	96.26	96.21	95.86
2.56	95.80	96.17	96.13	95.78
2.58	95.70	96.08	96.05	95.70

(Continued)

Depth (cm)	Field sizes (cm^2)			
	5×5	10×10	15×15	20×20
2.60	95.61	95.99	95.97	95.61
2.62	95.51	95.90	95.89	95.53
2.64	95.41	95.80	95.80	95.45
2.66	95.31	95.71	95.72	95.37
2.68	95.21	95.62	95.63	95.29
2.70	95.11	95.53	95.55	95.21
2.72	95.00	95.43	95.46	95.13
2.74	94.90	95.34	95.37	95.05
2.76	94.79	95.24	95.28	94.97
2.78	94.68	95.15	95.19	94.89
2.80	94.57	95.05	95.10	94.82
2.82	94.46	94.96	95.01	94.74
2.84	94.35	94.86	94.92	94.67
2.86	94.23	94.77	94.83	94.60
2.88	94.11	94.67	94.73	94.53
2.90	94.00	94.58	94.64	94.47
2.92	93.88	94.49	94.55	94.40
2.94	93.75	94.39	94.46	94.35
2.96	93.63	94.30	94.37	94.29
2.98	93.50	94.21	94.28	94.24
3.00	93.37	94.12	94.19	94.19

APPENDIX H

The percentage depth dose of the square open field sizes derived from the measurement using PFD^{3G} dosimeter at the depth of 0.006 to 3.020 cm in Blue water phantom for the 6 MV photon beam.

Depth (cm)	Field sizes (cm^2)			
	5×5	10×10	15×15	20×20
0.006	40.30	43.60	47.90	52.00
0.020	42.20	45.40	49.40	53.10
0.060	46.10	48.80	52.30	55.40
0.100	50.80	53.10	56.20	58.60
0.140	56.00	57.90	60.70	62.50
0.180	61.40	63.00	65.60	66.80
0.220	66.50	68.00	70.40	71.30
0.260	70.80	72.40	74.80	75.60
0.300	74.30	76.00	78.40	79.30
0.340	77.20	79.00	81.20	82.30
0.380	79.70	81.50	83.40	84.60
0.420	82.00	83.60	85.30	86.50
0.460	84.10	85.70	87.10	88.40
0.500	86.00	87.70	88.80	90.00
0.540	87.80	89.40	90.40	91.60
0.580	89.30	90.80	91.80	93.00
0.620	90.70	92.00	93.00	94.10
0.660	92.00	93.10	94.10	95.00
0.700	93.10	94.10	95.00	95.70
0.740	94.00	94.90	95.80	96.40
0.780	94.90	95.70	96.50	97.00
0.820	95.80	96.40	97.00	97.60
0.860	96.50	96.90	97.50	98.00
0.900	97.20	97.50	97.90	98.40
0.940	97.70	98.00	98.30	98.80
0.980	98.10	98.30	98.70	99.20
1.020	98.40	98.60	98.90	99.40
1.060	98.60	98.80	99.00	99.60
1.100	98.90	99.10	99.20	99.80
1.140	99.10	99.30	99.40	99.80
1.180	99.30	99.50	99.50	99.80
1.220	99.50	99.70	99.60	99.90
1.260	99.70	99.80	99.80	99.90
1.300	99.80	99.90	99.90	100.00
1.340	99.90	99.90	100.00	100.00
1.380	100.00	100.00	100.00	100.00

(Continued)

Depth (cm)	Field sizes (cm^2)			
	5×5	10×10	15×15	20×20
1.420	100.00	100.00	100.00	100.00
1.460	99.90	99.90	99.90	99.80
1.500	100.00	99.90	99.80	99.70
1.540	100.00	99.80	99.80	99.70
1.580	99.90	99.80	99.90	99.60
1.620	99.80	99.80	99.80	99.50
1.660	99.70	99.70	99.60	99.40
1.700	99.60	99.60	99.50	99.30
1.740	99.50	99.50	99.30	99.20
1.780	99.30	99.30	99.10	99.10
1.820	99.10	99.10	98.90	98.90
1.860	98.80	99.00	98.70	98.60
1.900	98.70	98.80	98.60	98.50
1.940	98.60	98.60	98.60	98.30
1.980	98.50	98.60	98.60	98.30
2.020	98.30	98.60	98.60	98.20
2.060	98.10	98.60	98.50	98.20
2.100	97.90	98.50	98.30	98.10
2.140	97.80	98.30	98.10	97.90
2.180	97.60	98.10	97.80	97.70
2.220	97.40	97.90	97.60	97.60
2.260	97.20	97.50	97.50	97.50
2.300	96.90	97.30	97.30	97.30
2.340	96.70	97.00	97.10	97.00
2.380	96.60	96.90	97.10	96.80
2.420	96.40	96.80	97.10	96.70
2.460	96.10	96.70	96.90	96.50
2.500	95.80	96.70	96.80	96.50
2.540	95.50	96.60	96.60	96.40
2.580	95.30	96.40	96.30	96.30
2.620	95.10	96.20	96.10	96.10
2.660	94.90	96.00	95.90	96.00
2.700	94.70	95.80	95.70	95.90
2.740	94.50	95.70	95.40	95.70
2.780	94.40	95.60	95.20	95.60
2.820	94.40	95.40	95.10	95.40
2.860	94.30	95.40	95.00	95.20
2.900	94.20	95.20	94.90	95.10
2.940	94.00	95.10	94.80	94.90
2.980	93.70	94.80	94.70	94.80
3.020	93.50	94.50	94.50	94.80

APPENDIX I

The percentage depth dose of the square open field sizes derived from the measurement using Markus chamber at the depth of 0.003 to 3.000 cm in solid water phantom for the 6 MV photon beam.

Depth (cm)	Field sizes (cm^2)						
	3×3	5×5	10×10	12×12	15×15	20×20	25×25
0.003	18.62	20.99	27.01	29.38	32.88	38.38	43.28
0.200	61.84	63.24	67.05	68.58	70.88	74.36	77.25
0.300	72.59	72.62	75.78	76.38	78.98	81.80	84.90
0.500	85.58	85.92	88.00	89.10	90.19	92.02	93.43
1.000	98.52	98.37	98.89	99.17	99.45	99.94	100.10
1.200	99.68	99.82	99.84	100.01	100.19	100.44	100.52
1.500	100.00	100.00	100.00	100.00	100.00	100.00	100.00
2.000	98.56	98.67	98.70	98.57	98.63	98.64	98.60
3.000	93.32	93.72	94.37	94.49	94.60	94.83	94.84

The percentage depth dose of the rectangular open field sizes derived from the measurement using Markus chamber at the depth of 0.003 to 3.000 cm in solid water phantom for the 6 MV photon beam.

Depth (cm)	Field sizes (cm^2)					
	5×15	15×5	7×18	18×7	12×17	17×12
0.003	24.29	24.34	27.39	27.33	31.60	31.56
0.200	65.96	65.79	67.97	67.70	70.61	70.43
0.300	75.21	75.08	76.95	76.65	79.13	78.92
0.500	87.05	87.03	88.32	88.07	89.64	89.67
1.000	98.51	98.40	98.76	98.67	99.12	99.12
1.200	99.67	99.70	99.90	99.81	100.06	100.06
1.500	100.00	100.00	100.00	100.00	100.00	100.00
2.000	98.44	98.46	98.51	98.50	98.49	98.52
3.000	94.12	94.05	94.45	94.44	94.61	94.59

APPENDIX J

The percentage depth dose of the square open field sizes derived from the measurement using TLD chips at the depth of 0.025 to 3.000 cm in solid water phantom for the 6 MV photon beam.

Depth (cm)	Field sizes (cm^2)			
	5×5	10×10	15×15	20×20
0.025	22.76	28.21	33.04	39.34
0.200	62.66	66.80	71.08	75.06
0.300	71.43	76.16	79.93	83.69
0.500	85.17	89.04	92.04	95.05
1.000	97.46	99.75	100.33	100.45
1.200	99.99	100.11	100.35	100.66
1.500	100.00	100.00	100.00	100.00
2.000	98.40	99.99	100.35	100.67
3.000	92.41	94.44	97.22	100.00

BIOGRAPHY

NAME	Ms. Lukkana Apipunyasopon
SEX	Female
NATIONALITY	Thai
DATE OF BIRTH	11 June 1980
PLACE OF BIRTH	Bangkok, Thailand
INSTITUTIONS ATTENDED	Mahidol University, 1997-2001:

Mahidol University, 1997-2001:

Bachelor of Science

(Radiological Technology)

Mahidol University, 2001-2004:

Master of Science

(Radiological Science)

Chulalongkorn University, 2008-2012:

Doctoral of Engineering

(Nuclear Engineering)

HOME ADDRESS 161/1012 Jaransanitwong Rd, Bangkunsri, Bangkoknoi, Bangkok Thailand 10700

Tel. 02-4121091, 089-7962144

Email: laa393@yahoo.com

PUBLICATION An investigation of the depth dose in the build-up region, and surface dose for a 6-MV therapeutic photon beam: Monte Carlo simulation and measurements. J Radiat Res 54 (2013): 374-382.